

A SIMPLE PARAMETERIZATION TO PREDICT
POPULATION CHARACTERISTICS OF BOUNDARY-LAYER CUMULUS CLOUDS

by

LARRY KEITH BERG

B.Sc., The Pennsylvania State University, 1993

A THESIS SUBMITTED IN PARTIAL FULFILLMENT
OF THE REQUIREMENTS FOR THE DEGREE OF
MASTER OF SCIENCE

in

THE FACULTY OF GRADUATE STUDIES

Department of Geography

Atmospheric Science Programme

We accept this thesis as conforming
to the required standard

/The University of British Columbia

November 1996

© Larry Keith Berg, 1996

In presenting this thesis in partial fulfilment of the requirements for an advanced degree at the University of British Columbia, I agree that the Library shall make it freely available for reference and study. I further agree that permission for extensive copying of this thesis for scholarly purposes may be granted by the head of my department or by his or her representatives. It is understood that copying or publication of this thesis for financial gain shall not be allowed without my written permission.

Department of Geography
The University of British Columbia
Vancouver, Canada

Date 12 December 4, 1996

ABSTRACT

Estimates of fair-weather cumulus size distributions are made from the joint frequency distribution (JFD) of virtual potential temperature (θ_v) vs height of the lifting condensation level (z_{LCL}) collected from a single surface weather station. Conceptually, the JFD represents the likelihood that a parcel will rise and the likelihood that condensation will occur. The θ_v and the z_{LCL} for each point of the JFD can be compared to the mean θ_v of the mixed layer. If the parcel has a θ_v less than that of the mixed layer the parcel will not rise. If the parcel has a larger θ_v the parcel will rise dry adiabatically. A subset of the these rising parcels will reach their z_{LCL} and form clouds. These parcels will continue to rise, moist adiabatically, until they reach the stable layer above the convective mixed layer. Other rising parcels will not condense but will continue to rise, dry adiabatically, as clear air parcels until they reach the stable layer.

The cloud model was designed to use a JFD measured near the top of the surface layer using fast-response instruments mounted on a research aircraft flying over a large area. It is very expensive to obtain surface-layer data using an aircraft. It would be desirable if a JFD based on inexpensive surface measurements could be used. These experiments will not only investigate the CuP model results, but will also determine if a less expensive JFD computed from a single surface weather station can be used instead.

Using a JFD of θ_v vs z_{LCL} calculated from a single surface station, cloud ensemble estimates are compared to cloud measurements made at the Atmospheric Radiation Experiment (ARM) site in central Oklahoma during the spring and summer 1994 and 1995 intensive operations periods. There was some skill predicting the cloud-base height — in

most cases the model estimates were bracketed by observations. No observations of cloud-thickness are made at the ARM site. However, model estimates of cloud-thickness are nearly log-normally distributed, consistent with observations by Lopez (1977) and Stull (1988). Using a JFD constructed from a single-surface station there is little skill predicting cloud cover.

TABLE OF CONTENTS

Abstract		ii
Table of Contents		iv
List of Tables		vi
List of Figures		viii
Chapter One	Introduction, Motivation and Literature Review	1
Chapter Two	Theory	5
	The Joint Frequency Distribution	5
	Cloud Cover and Cloud-Field Prediction	6
	Daily Evolution of Cloud Cover	9
	Computation of the Joint Frequency Distribution	11
Chapter Three	Site Description	14
	Instrument Description	17
Chapter Four	CuP Model Meteorological Input	21
	Determination of the Mixed Layer Depth	21
	Calculation of the Joint Frequency Distribution from Single Stations	21
	Calculation of the Mixed Layer θ_v and z_{LCL}	24
	Error Analysis	25
Chapter Five	Case Study Days	27
	Date: 1 May 1994	27
	Date: 27 July 1994	27
	Date: 28 July 1994	28
	Date: 31 July 1994	28
	Date: 27 June 1995	29
	Date: 6 July 1995	29
	Date: 9 July 1995	30
	Date: 11 July 1995	30
	Date: 13 July 1995	31

Chapter Six	CuP Model Sensitivity	32
	Changes in the Mean of the JFD	32
	Slope of Bowen-ratio Axis	34
	Slope of Solar-Forcing Axis	37
	Bowen ratio and Solar-Forcing Standard Deviations	39
	JFD and θ_v Interactions	41
Chapter Seven	Results	46
	Mixing Line Analysis	47
	Model Accuracy and Measurement Errors	49
	Detailed Results	51
	Daily Results	68
Chapter Eight	Conclusions and Future Work	106
	Shortcomings and Improvements	107
	Other Future Work	109
References		111
Appendix A	Instrument Uncertainty	116
Appendix B	Comparison of Empirical and Parcel Determination of z_{LCL}	118
Appendix C	Sample Error Calculation	121
Appendix D	Cloud and Weather Observations	127
Appendix E	JFD Parameters	155

LIST OF TABLES

3.1	Instruments at each of the ARM facilities	15
4.1	Errors for the SMOS	25
4.2	Propagation of errors	26
6.1	Times of sensitivity plots	32
7.1	Calculated and critical statistics for a log-normal fit	62
7.2	Mean and variance of cloud base height observed at the CF	65
7.3	Statistical tests comparing CuP and observed means	66
7.4	Statistical tests comparing CuP and observed variances	67
7.5	Values of z_i , $\overline{\theta_{v,ML}}$, and $z_{LCL,ML}$	68
A.1	Accuracy of SMOS pressure, humidity and precipitation measurements	116
A.2	Wind accuracy for a given wind speed for SMOS 13	116
A.3	Temperature accuracy for a given wind speed for SMOS 13	117
A.4	Accuracy of EBBR measurements	117
A.5	Accuracy of sonde measurements	117
B.1	Values z_{LCL} calculated from analytical and iterative methods	118
D.1	Cloud descriptions used by human observers at the ARM CART site	127
D.2	Hourly observations from 1 May, 1994 at the Central Facility	133
D.3	Hourly cloud coverage by sky quadrant at the Central Facility 1 May, 1994	134
D.4	Hourly overhead cloud amounts from 1 May, 1994	135
D.5	Hourly observations from 27 July, 1994 at the Central Facility	136
D.6	Hourly cloud coverage by sky quadrant at the Central Facility 27 July, 1994	137
D.7	Hourly overhead cloud amounts from 27 July, 1994	138
D.8	Hourly observations from 28 July, 1994 at the Central Facility	139
D.9	Hourly cloud coverage by sky quadrant at the Central Facility 28 July, 1994	140
D.10	Hourly overhead cloud amounts from 28 July, 1994	141
D.11	Hourly observations from 31 July, 1994 at the Central Facility	141
D.12	Hourly cloud coverage by sky quadrant at the Central Facility 31 July, 1994	142
D.13	Hourly overhead cloud amounts from 31 July, 1994	143
D.14	Hourly observations from 27 June, 1995 at the Central Facility	144
D.15	Hourly cloud coverage by sky quadrant at the Central Facility 27 June, 1995	145
D.16	Hourly overhead cloud amounts from 27 July, 1995	146
D.17	Hourly observations from 6 July, 1995 at the Central Facility	147

D.18	Hourly cloud coverage by sky quadrant at the Central Facility 6 July, 1995	148
D.19	Hourly overhead cloud amounts from 6 July 1995	149
D.20	Hourly observations from 9 July, 1995 at the Central Facility	149
D.21	Hourly cloud coverage by sky quadrant at the Central Facility 9 July, 1995	150
D.22	Hourly overhead cloud amounts from 9 July, 1995	150
D.23	Hourly observations from 11 July, 1995 at the Central Facility	151
D.24	Hourly cloud coverage by sky quadrant at the Central Facility 11 July, 1995	151
D.25	Hourly overhead cloud amounts from 11 July, 1995	152
D.26	Hourly observations from 13 July, 1995 at the Central Facility	152
D.27	Hourly cloud coverage by sky quadrant at the Central Facility 13 July, 1995	153
D.28	Hourly overhead cloud amounts from 13 July, 1995	154
E.1	JFD parameters used as input to the CuP model	155

LIST OF FIGURES

1.1	Surface and mixed-layer thermals	1
2.1	Properties of surface-layer parcels	6
2.2	Properties of surface-layer parcels with θ_v profile	7
2.3	Properties of surface-layer parcels with adiabats	8
2.4	Daily evolution of cloud cover	10
2.5	Slopes of Bowen-ratio and solar-forcing axes	12
3.1	Map of North America with case study area marked	14
3.2	Monthly average maximum and minimum temperatures at Ponca City and Enid Oklahoma	16
3.3	Monthly average precipitation at Ponca City and Enid Oklahoma	17
3.4	Sample Belfort Ceilometer and Micropulse Lidar cloud base observations	20
6.1	CuP model sensitivity to changes in z_{LCL}	33
6.2	CuP model sensitivity to changes in θ_v	34
6.3	CuP model sensitivity to changes in the slope of the Bowen-ratio axis	36
6.4	JFD with different Bowen-ratio axis slopes	37
6.5	CuP model sensitivity to changes in the slope of the solar-forcing axis	38
6.6	JFD with different solar-forcing axis slopes	39
6.7	CuP model sensitivity to changes in standard deviation along the Bowen-ratio axis	40
6.8	CuP model sensitivity to changes in standard deviation along the solar-forcing axis	41
6.9	Sample JFD and θ_v profiles	42
6.10	Sample clear and cloudy updrafts	44
6.11	Sample CuP predicted cloud thickness	45
7.1	Observed and modeled cloud amounts	47
7.2	Mixing lines between surface and mixed layer values of θ_v and z_{LCL}	48
7.3	CuP predicted frequency of a given cloud thickness for 28 July 1994	52
7.4	CuP predicted frequency of a given cloud thickness for 6 July 1995	53
7.5	Profiles of θ_v taken at the CF on 6 July 1995	55
7.6	Profiles of z_{LCL} taken at the CF on 6 July 1996	56
7.7	Plot of CuP cloud thickness vs. height for 1430 LST on 27 July 1994	57
7.8a	Cloud thickness as predicted by the CuP model	59
7.8b	Cloud thickness as predicted by the CuP model	60
7.9	Cloud thickness as predicted by the CuP model	61
7.10	CuP modeled up drafts for 28 July 1994, 1430 LST	63
7.11	CuP modeled up drafts for 6 July 1995, 1430 LST	64

7.12	Profiles of θ_v taken from CF sondes on 1 May 1994	71
7.13	Profiles of r taken from CF sondes on 1 May 1994	72
7.14	Profiles z_{LCL} taken from CF sondes on 1 May 1994	73
7.15	Observed and CuP modeled cloud cover on 1 May 1994	74
7.16	Observed and CuP model predicted cloud-base heights for 1 May	75
7.17	Profiles of θ_v taken from CF sondes on 27 July 1994	77
7.18	Observed and CuP model predicted cloud cover on 27 July 1994	78
7.19	Observed and CuP model predicted cloud-base height for 27 July 1994	79
7.20	Profiles of θ_v taken from CF sondes on 28 July 1994	80
7.21	Profiles of z_{LCL} taken from CF sondes on 28 July 1994	81
7.22	Observed and CuP model predicted cloud cover on 28 July 1994	82
7.23	Observed and CuP model predicted cloud-base height for 28 July 1994	83
7.24	Profiles of θ_v taken from CF sondes on 31 July 1994	84
7.25	Profiles of z_{LCL} taken from CF sondes on 31 July 1994	85
7.26	Observed and CuP model predicted cloud cover on 31 July 1994	86
7.27	Observed and CuP model predicted cloud-base height for 31 July 1994	87
7.28	Profiles of θ_v taken from CF sondes on 27 June 1995	88
7.29	Profiles of z_{LCL} taken from CF sondes on 27 June 1995	89
7.30	Observed and modeled cloud cover for 27 June 1995	90
7.31	Observed and CuP modeled cloud-base heights for 27 June 1995	92
7.32	Profiles θ_v taken from CF sondes on 6 July 1995	93
7.33	Profiles of r taken from the CF sondes on 6 July 1995	94
7.34	Profiles z_{LCL} taken from CF sondes on 6 July 1995	95
7.35	Observed and modeled cloud cover for 6 July 1995	96
7.36	Observed and CuP predicted cloud-base heights for 6 July 1995	97
7.37	Profiles θ_v taken from CF sondes on 9 July 1995	98
7.38	Observed and modeled cloud cover for 9 July 1995	99
7.39	Profiles of θ_v taken from CF sondes on 11 July 1995	100
7.40	Observed and CuP modeled cloud cover for 11 July 1995	101
7.41	Profiles θ_v taken from CF sondes on 13 July 1995	102
7.42	Profiles of z_{LCL} taken from CF sondes on 13 July 1995	103
7.43	Observed and modeled cloud cover for 13 July 1995	104
7.44	Observed and CuP modeled cloud-base height 13 July 1995	105
B.2	Differences between z_{LCL} calculated from empirical equation and parcel method	119
B.3	The z_{LCL} calculated from empirical equation vs. parcel method	120

1.0 Introduction, Motivation, and Literature Review

During periods of free convection, boundary-layer cumulus clouds are created by convective thermals. The core of each thermal contains relatively undiluted surface-layer air as shown in figure 1.1 (Crum and Stull 1987). The two most important parameters in the formation of these clouds are temperature and humidity of the surface layer, which is controlled by surface properties and solar radiation (Rabin et al. 1990).

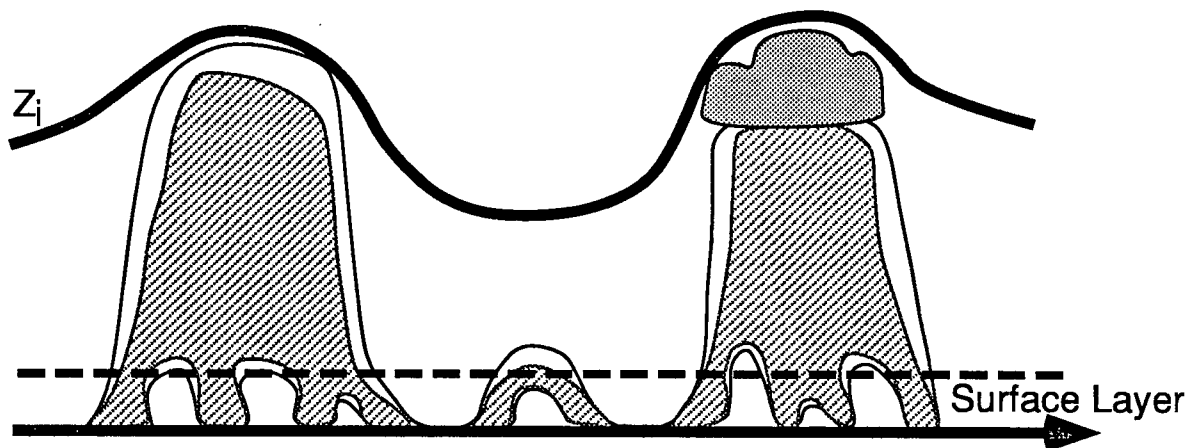


Figure 1.1. Sketch of surface and mixed-layer thermals. The mixed-layer depth is shown by the heavy solid line. The top of the surface layer is marked with the broken line. Thin lines mark the outlines of individual mixed-layer and surface-layer thermals. The core of surface-layer air in each thermal is represented by the heavy dark shapes. The right-most thermal has a cumulus-humilis cloud at its top.

Heterogeneous land surfaces cause small differences in air temperature and humidity in the horizontal. These landscape-induced variances can enhance those differences already present in the turbulent boundary layer. A Cumulus Potential (CuP) model has been developed to account for these effects on the observed cloud field.

The CuP model, described in section 2, will be tested against cloud distributions observed on several days from 1994 and 1995 at the Atmospheric Radiation Measurement

(ARM) site centered in north-central Oklahoma. The CuP model was developed to use aircraft data collected over a large area in the mid to upper surface layer. These experiments will not only investigate the accuracy of the CuP model but will also determine if a JFD computed from a single surface weather station can be used to form the JFD. The instrumentation at the ARM site will be described in section 3. Calculations and methods will be discussed in section 4. Weather for the study days will be described in section 5. Model sensitivity to input parameters will be reported in section 6. Model results will be compared to both human observations and instruments in section 7. Conclusions and future research efforts will be presented in section 8.

Boundary-layer cumulus clouds play an important role in the earth's radiation budget and large-scale dynamics. Stull (1992) observed scattered boundary-layer clouds on 261 days of the year over the upper-midwest US, 33% of the low clouds were boundary-layer cumulus, and 48% were stratocumulus. Raga and Jonas (1993) found that boundary-layer cumulus near the British Isles change the earth's albedo on a horizontal scale smaller than a typical Atmospheric Global Climate Model (AGCM) grid cell. Boundary-layer cumulus are important in model simulations of the Indian Monsoon because they transport moisture from the boundary layer to the free atmosphere (Slingo et al. 1988).

In many AGCM's the cumulus parameterization is for only deep precipitating cumulus (e.g. Donner 1993). Forecasts of the nonprecipitating cloud amount are generally made using: grid box relative humidity, precipitation rate, cloud mass flux, or layer-average mass flux (Sud et al. 1991, Tiedtke 1989, and Slingo 1987). Xu and Krueger

(1991), using a cloud-resolving model, showed that these methods, with the exception of the cloud mass-flux scheme, are unsatisfactory for representing convective clouds. Cloud amounts predicted also have a strong dependence on model vertical resolution (Tiedtke 1993, Xu and Krueger 1991).

Computer modeling efforts have shown that the formation of boundary-layer cumulus is sensitive to both the state of the atmosphere and the underlying surface. Many authors (Liu and Avissar 1996, Chen and Avissar 1994, Hong et al. 1995, and Rabin et al. 1990) have found that land and atmospheric characteristics can enhance the formation of cumulus clouds and precipitation.

Researchers are working to improve the cloud parameterizations. Wilde et al. (1985) developed a cumulus-cloud model that used the distributions of surface moisture and entrainment-zone height. Smith (1990) developed a cloud scheme that assumes a distribution of thermodynamic and water variables about the grid box mean. Tiedtke (1993) developed a prognostic cloud scheme which treats boundary-layer cumulus in the cumulus convection scheme. Wetzel (1990) compared several different cloud models by predicting cloud cover during the Wangara experiment. He used Wilde's scheme, a simple parcel method, a nine parcel method and the relative humidity at the top of the boundary-layer. Wetzel (1990) found that the nine parcel and single parcel methods gave the best results. The CuP model is similar to the nine parcel model proposed by Wetzel, both use a distribution of surface temperature and humidity. Wetzel and Boone (1995) have included an air parcel cloud model in their surface-atmosphere model. In their model a mixing distribution of surface and mixed-layer air is prescribed.

Research has also explored the size distributions and spatial relationships of cumulus clouds. Wielicki and Welch (1986) studied cumulus-cloud fields over both land and water. Hozumi et al. (1982) and Plank (1969) used aerial photographs to study fair-weather cumulus clouds over the ocean. Lopez (1977) found that both cumulus-cloud heights and diameters have a log-normal distribution over many geographic areas. Joseph and Cahalan (1990), Sengupta et al. (1990) Weger et al. (1992) and Zhu et al. (1992) investigated clustering and randomness in cumulus-cloud fields. Cahalan (1991) found a break in the power-law relationship between cloud size and number distribution near a cloud diameter of 2 km for clouds over ocean surfaces. The CuP also model predicts the size distribution of the clouds based on buoyancy information contained in the JFD.

2.0 Theory

2.1 The Joint Frequency Distribution

Boundary-layer cumulus clouds form near the top of mixed-layer thermals. The roots of these thermals are near the top of the surface layer (Williams and Hacker 1992). These thermals rise, largely undiluted through the convective mixed layer. Some thermals may rise past their level of condensation and form clouds. During times of free convection and negligible shear-generated turbulence, surface heating is the driving force behind the thermals.

Heterogeneity in the surface can help enhance the turbulence in the convective boundary layer. Different parcels of surface-layer air will have different values of temperature and humidity caused by heterogeneous heat and moisture-flux coupling with the ground. Figure 2.1 shows a sketch of surface-layer parcels and their temperature and humidity characteristics. The parcel shading represents temperature; those that are darker are warmer. The humidity of the parcel is represented by the height of the lifting condensation level (z_{LCL}). Warmer parcels can be associated with dry fields, stronger solar insolation, or a small albedo. Parcels that are more moist can be associated with irrigated fields, or areas that received recent rainfall.

The temperature and humidity of each parcel can be used to compute the virtual potential temperature (θ_v) a measure of buoyancy, and z_{LCL} , the height that a parcel needs to rise to form a cloud (Schrieber et al. 1996). The number of parcels having various combinations of z_{LCL} and θ_v can be counted to form a joint frequency distribution (JFD). The JFD for a range of land-use types can be quite complicated with many modes. But

Schrieber et al. (1996) show how this complex JFD can be modeled as the sum of simpler distributions. The measured or modeled JFD can then be compared with a mean mixed-layer θ_v profile to predict the cloud coverage.

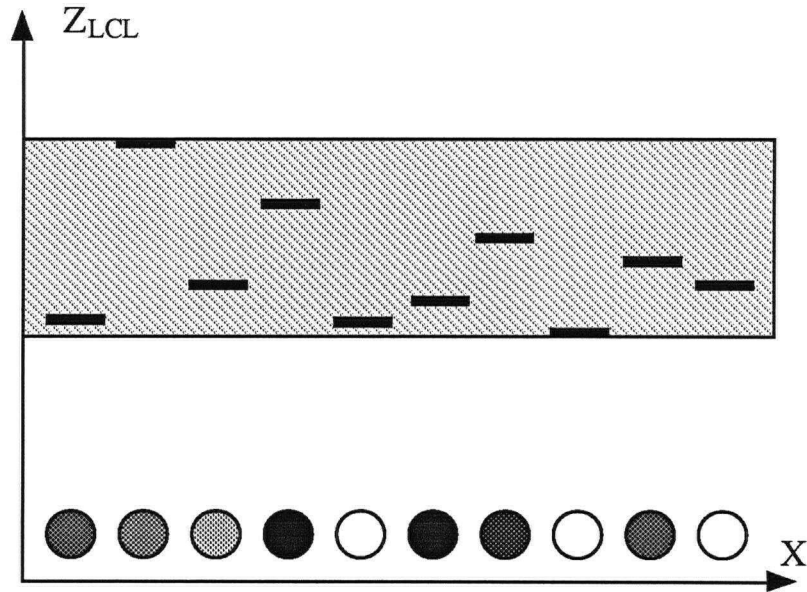


Figure 2.1. Sketch of temperature and moisture of surface air parcels. Darker parcels are warmer. Dashes correspond to the z_{LCL} of the parcel. The shaded region is the range of z_{LCL} values.

2.2 Cloud-Cover and Cloud-Field Prediction

2.2.1 Cloud Cover and Cloud-Base Altitude

Figure 2.2 shows a sketch similar to figure 2.1, along with a sample JFD and mean environmental θ_v profile. The shaded region marks the entrainment zone, the range of heights to which buoyant parcels are expected to rise. Some parcels are cooler than the environment, they are more dense than their surroundings and will not rise. Parcel one is an example of such a parcel, and its location in the JFD is marked. All similar parcels to the left of the dashed line are cooler than the environment and will also not rise. The rest of the parcels are warmer than the environment, so they are buoyant and will rise. Of the

parcels that rise, some, like parcel two, will reach the entrainment zone and stop rising before reaching its z_{LCL} . These parcels will form clear air updrafts. The rest of the rising parcels, such as parcel three, will rise and reach their z_{LCL} . These parcels will condense and continue to rise as a clouds.

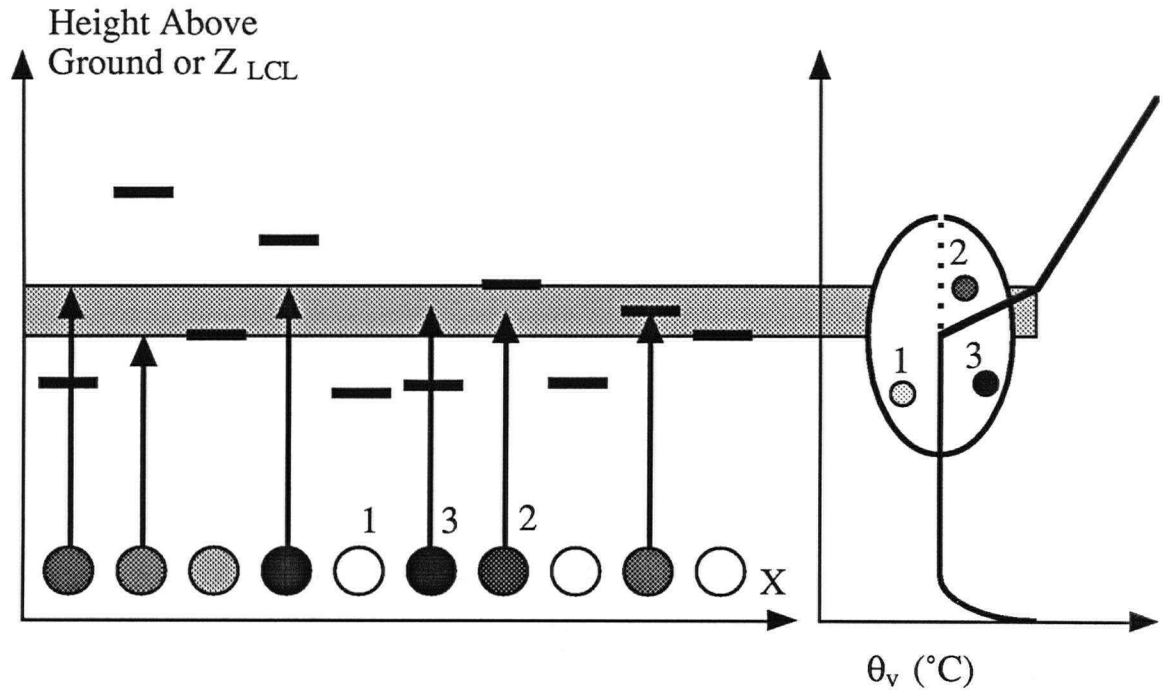


Figure 2.2. Similar figure 2.1 but with the mean θ_v profile and a JFD of z_{LCL} and θ_v (oval) shown on the right. The location of surface parcels 1, 2 and 3 on the JFD are shown. The shaded area is the entrainment zone and is the height to which most parcels will rise.

Cloud coverage can be computed by comparing the number of rising cloudy parcels to the number of total parcels. This is equivalent to the portion of the JFD that is below and to the right of the θ_v profile. Since different parcels in the JFD have different z_{LCL} values, a range of cloud-base heights is expected, consistent with the findings of Plank (1969).

2.2.2 Cloud Height and Cloud Thickness

After condensation occurs in a parcel, it will continue to rise moist adiabatically.

Tops of both clear and cloudy thermals are determined by the location at which the parcel reaches the environmental θ_v . The clear thermal top formed by parcel 2 and the cloudy thermal top formed by parcel 3 are marked in figure 2.3 by the arrows. Because the cloudy parcels follow the moist adiabat for part of their ascent, they can rise to greater depths than if they had remained cloudless.

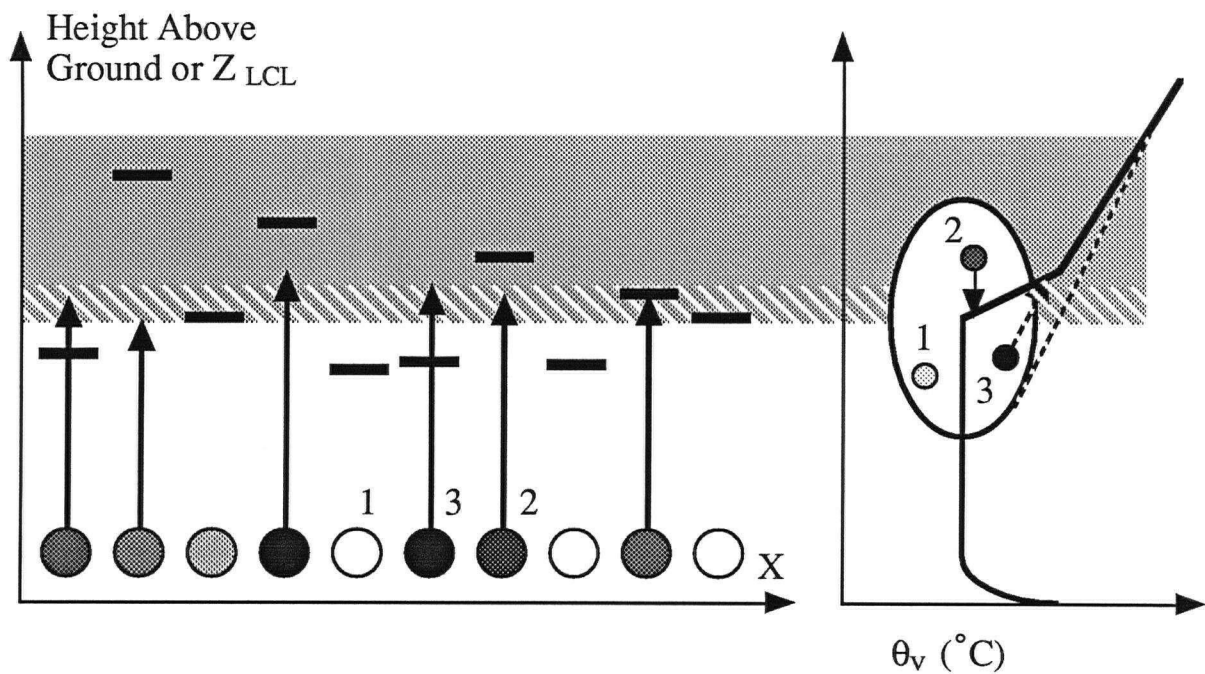


Figure 2.3. Similar to figure 2.2 but with moist adiabats included on the JFD (broken arrows). The height to which parcels 2 and 3 would rise are marked on the JFD with arrows. The shaded area marks the height range of cloudy thermal tops. The hashed area marks the height range of clear thermal tops. In this example the area with white hashes lies within the shaded area.

Cloud thickness is the difference between cloud top and z_{LCL} . The thermals will create a cloud field having a range of heights. The CuP model predicts a range of both clear and cloudy thermal tops because the parcels producing the clear and cloudy thermals have different z_{LCL} and θ_v values.

2.2.3 Implications

The CuP model defines three different layers in the cloud-topped boundary layer. The bottom layer is the typical cloud-free boundary layer, and the top layer is a region of completely cloudy updrafts. In between is a unique layer that includes both clear and cloudy updrafts. This layer is not quite the same as the clear-air transition layer described by Malkus (1958) for tropical cumulus. It also is not like the entrainment zone found in the tank experiments described by Deardorff et al. (1980). It is not quite like the LCL zone described by Wilde et al. (1985) which assumes that buoyancy and moisture content of thermals are independent.

2.3 Daily Evolution of Cloud Cover

Early in the day the mixed layer depth (z_i) is small, the JFD is typically located well above the turbulent mixed layer (figure 2.4), which implies no clouds. As the day progresses the layer will continue to warm, moving the θ_v profile to the right. The JFD would warm as well, moving to the right at approximately the same rate as the mixed layer. Since both the θ_v profile and JFD are moving in unison, there is little effect on the amount of cloud cover predicted. However, surface heating does increase the probability of cloud

formation by causing z_i to grow. If the surface layer becomes more moist due to evaporation from the surface, the JFD would be expected to move down relative to the θ_v profile, which could increase cloud formation. If the layer dries with time, the JFD would then rise relative to the profile reducing the probability of cloud formation.

In figure 2.4 the mixed layer becomes more moist between A and B, and z_i has grown. Clouds would begin to form when the JFD and the profile first intersect. Cloud cover would then increase as the mixed layer continues to grow. The surface layer has dried between B and C but the amount of cloud cover will still increase in this hypothetical scenario because of the growth of z_i .

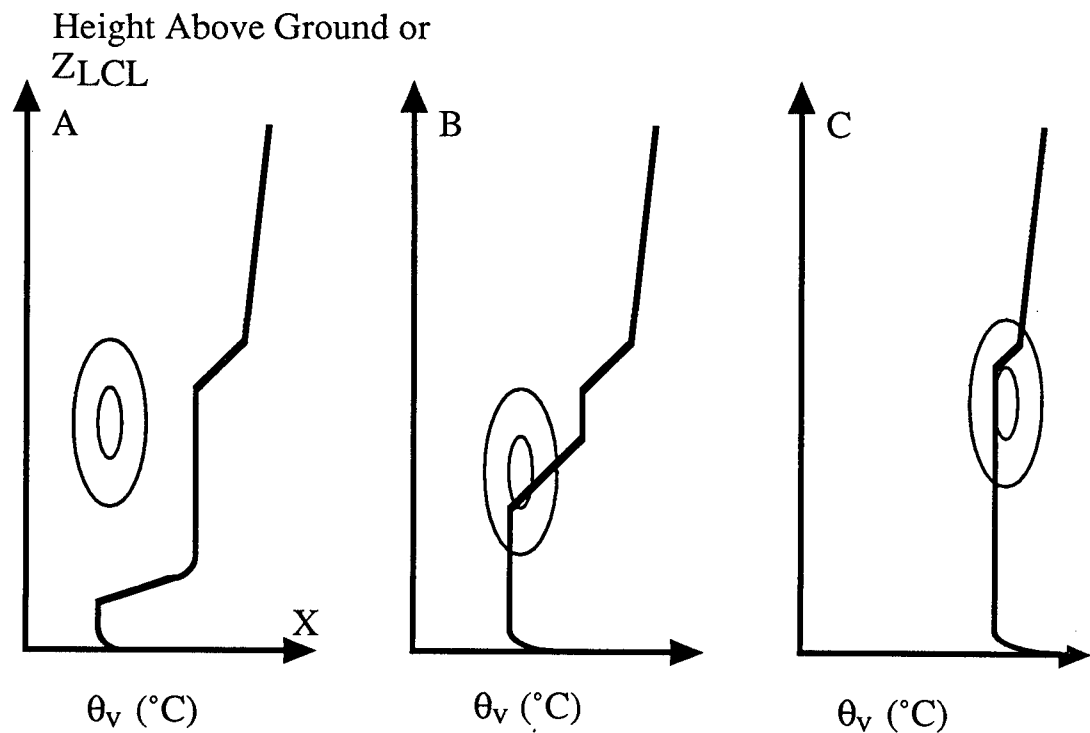


Figure 2.4. A sample evolution of θ_v profile and JFD. Figure A corresponds to an early morning situation, while B and C would be typical later in the morning. The mixed layer is very thin in A, but grows through the residual layer throughout the morning.

2.5 Computation of the Joint Frequency Distribution.

Measurements of z_{LCL} and θ_v can be used to form a distribution of data points. This distribution can be approximated with a simple function to create a JFD for use in the CuP model. Unfortunately z_{LCL} and θ_v are not independent because both are linked by the surface energy budget, warmer areas tend to be drier, so the major and minor axes of the JFD would not be parallel to the z_{LCL} and θ_v axes. A set of variables that are independent would be more convenient for fitting the distribution. Schrieber et al. (1996) chose to use a coordinate system based on the surface fluxes.

Schrieber et al. (1996) found that the Bowen ratio and the total flux (the sum of the sensible and latent heat flux) can be used to define the JFD. They expressed the total flux by the solar forcing, which is proportional to the temperature difference between the mixed layer and ground skin that would be needed to drive the total flux (Stull 1988). Equations for z_{LCL} and θ_v can be derived based on both the Bowen ratio and solar forcing (Schrieber et al. 1996). Figure 2.5 shows a lines of constant Bowen ratio and solar forcing plotted in z_{LCL} and θ_v space. Although these lines do not appear to be geometrically orthogonal in the z_{LCL} and θ_v plot, they are physically orthogonal. The lines of constant Bowen ratio converge at the mixed-layer value of Bowen ratio. The slope of each line can change relative to the z_{LCL} and θ_v axes, and each line is linear in z_{LCL} and θ_v space.

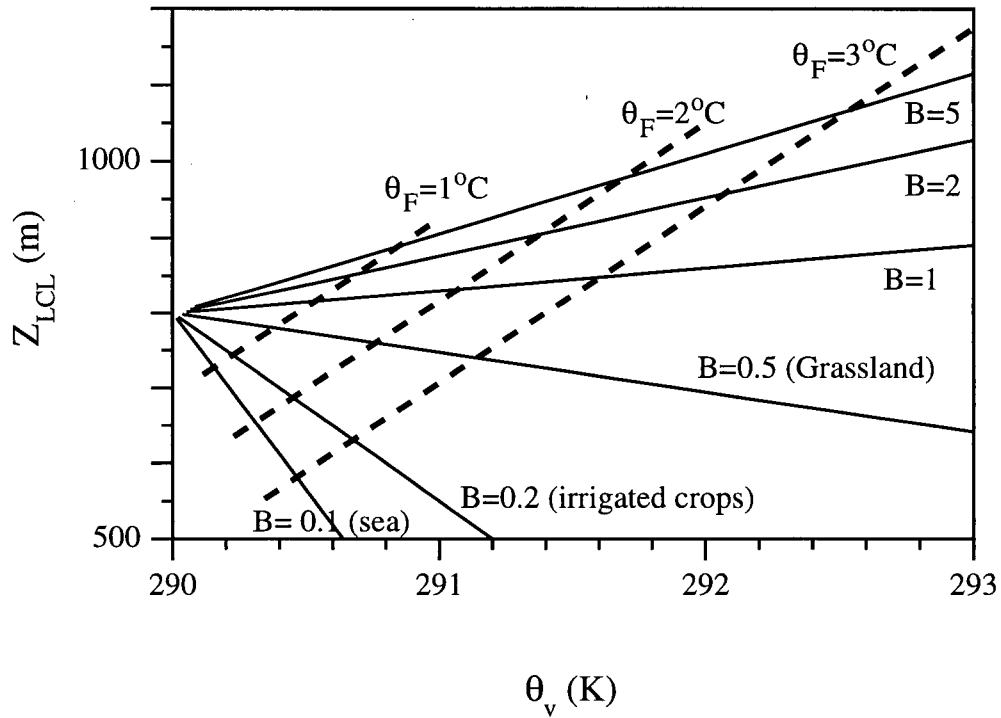


Figure 2.5. Example of θ_v and z_{LCL} as a function of the Bowen ratio B (solid lines) and the solar forcing temperature θ_F (dashed lines). Larger Bowen ratios occur over drier ground. Larger solar forcing can be caused by higher sun angles, smaller albedo, and/or less cloud shading (after Schrieber et al. 1996).

The Bowen ratio and solar forcing are related to boundary-layer physics. Changes in solar forcing can be attributed to variations in albedo, partial shading by clouds, or changes in sun angle. These variations would cause the JFD to spread along lines of constant Bowen ratio. Variations in Bowen ratio can be caused by differences in soil moisture or crop type. Bowen-ratio variations would cause the JFD to spread along lines of constant solar forcing. In nature the JFD is controlled by a combination of both types of forcing.

Schrieber et al. (1996) fit a Gaussian distribution in Bowen ratio and solar forcing space using maximum-likelihood procedures. The shape parameters used to define the JFD

were the slope of the Bowen ratio and solar forcing axes in z_{LCL} and θ_v space and the standard deviation along each of the axes. The Gaussian distribution takes on the form:

$$G(m, c) = \frac{1}{2\pi \cdot m_{bd} \cdot c_{ds}} \exp \left\{ -\frac{1}{2} \left[\left(\frac{m}{m_{bd}} \right)^2 + \left(\frac{c}{c_{ds}} \right)^2 \right] \right\} \quad (2.1)$$

where m is a surrogate measure of location on the Bowen ratio axis projected onto the z_{LCL} axis, c is a surrogate measure of location on the solar forcing axes projected onto the θ_v axis, m_{bd} (m) is the corresponding surrogate standard deviation along the Bowen ratio axis, and c_{ds} (K) is the corresponding surrogate standard deviation along the solar-forcing axis.

While the Bowen ratio and solar forcing axes are more convenient for fitting a JFD to observations, z_{LCL} and θ_v are directly related to cloud formation. Therefore the computed Gaussian distribution is converted back to z_{LCL} and θ_v coordinates using geometric arguments, for use in the CuP model.

3.0 Site Description

Data used for verification of the CuP model was collected at the United States Department of Energy Atmospheric Radiation Measurement (ARM) site (36.6° N, 97.9° W). The site encompasses an area of over $1.2 \times 10^5 \text{ km}^2$ and includes parts of Oklahoma and Kansas (figure 3.1). Land use in the region varies from agricultural to urban. Instruments are distributed among the Central Facility (CF), three boundary facilities and 27 extended facilities, as listed in table 3.1

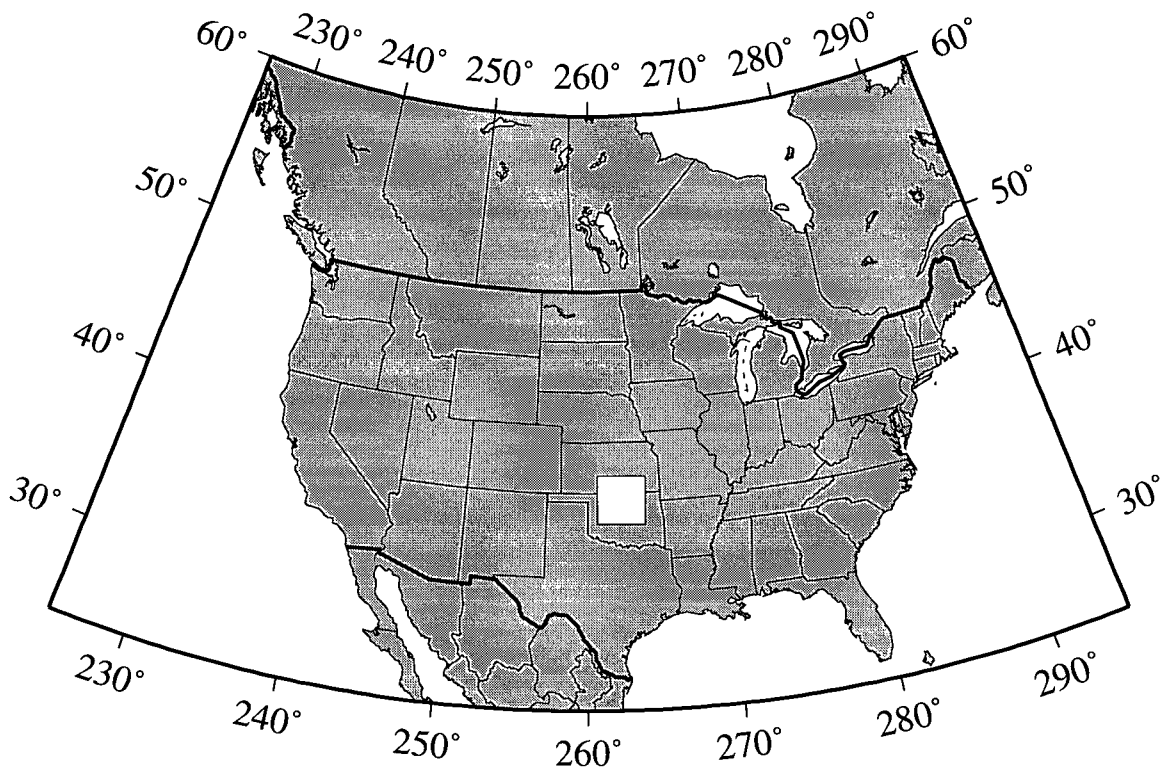


Figure 3.1. Map of North America with the ARM site marked with the large white box. The box represents the approximate size of the ARM domain.

Table 3.1. Instruments at each of the ARM facilities (Splitt et al. 1995). Items in italics are variables measured.

Central Facility	Extended Facilities	Boundary Facilities
Sondes:	Energy Balance Bowen Ratio:	Sondes:
<i>Temperature Profile</i>	<i>Sensible Heat Flux</i>	<i>Temperature Profile</i>
<i>Humidity Profile</i>	<i>Latent Heat Flux</i>	<i>Humidity Profile</i>
<i>Wind Profile</i>	Solar and Infrared	<i>Wind Profile</i>
Microwave Radiometer:	Observations Station:	Microwave Radiometer:
<i>Liquid Water Path</i>	<i>Solar Direct Beam</i>	<i>Liquid Water Path</i>
Micropulse Lidar:	<i>Irradiance</i>	
<i>Cloud Base Height</i>	<i>Solar Diffuse</i>	
Belfort Ceilometer:	<i>Irradiance</i>	
<i>Cloud Base Height</i>	<i>Total Solar Irradiance</i>	
Whole Sky Imager:	<i>IR Irradiance</i>	
<i>Cloud Cover</i>	Surface Meteorological	
Human Observations:	Station:	
<i>Cloud Cover</i>	<i>Temperature</i>	
<i>Cloud Type</i>	<i>Humidity</i>	
<i>Weather</i>	<i>Pressure</i>	
Atmospherically Emitted	<i>Winds</i>	
Radiance Interferometer:		
<i>Temperature Profile</i>		
<i>Humidity Profile</i>		

The central facility (CF) and two extended facilities are located in southeastern Grant county, Oklahoma. The area near the CF is mostly cultivated — only a small amount remains as range land or other uses. All of the towns near the CF are small (less than 6 km²). Crops near the CF are primarily (60-80%) non-irrigated wheat, but some hay, sorghum, and alfalfa are also grown. There are some trees, generally less than 10 m tall,

along fence rows and in drainage areas. The predominate soil type in Grant county is silt loam, but the CF is located in an area of silty clay loam.

The region's climate is continental, with frequent inflow of hot humid air from the Gulf of Mexico during the summer. Winds are generally southerly throughout most of the year, but switch to a northerly direction in the winter. Rainfall in north-central Oklahoma is heaviest during May, June, and July. Monthly average maximum and minimum temperatures are plotted in figure 3.2 for Ponca City (40 km east of the CF) and Enid (40 km southeast of the CF), and monthly average precipitation is plotted in figure 3.3.

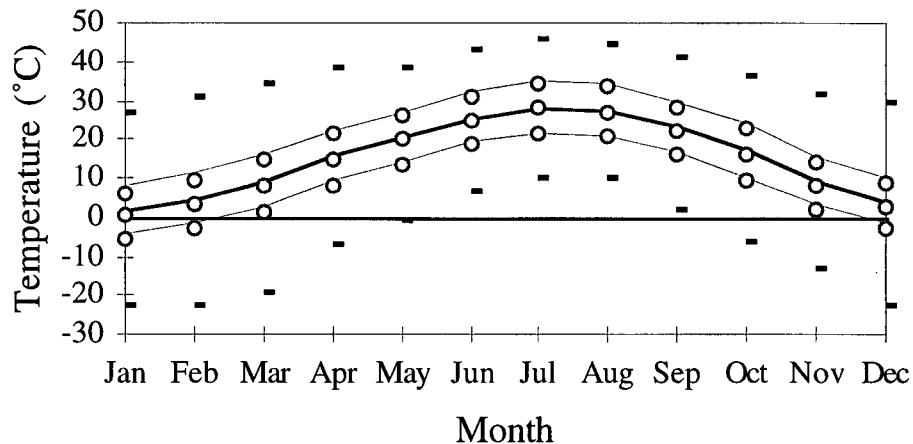


Fig 3.2. Monthly average maximum, minimum, and average temperature at Ponca City (lines) and Enid (circles), Oklahoma. Tick marks show the record maximum or record minimum at either of the locations (Ruffner 1985).

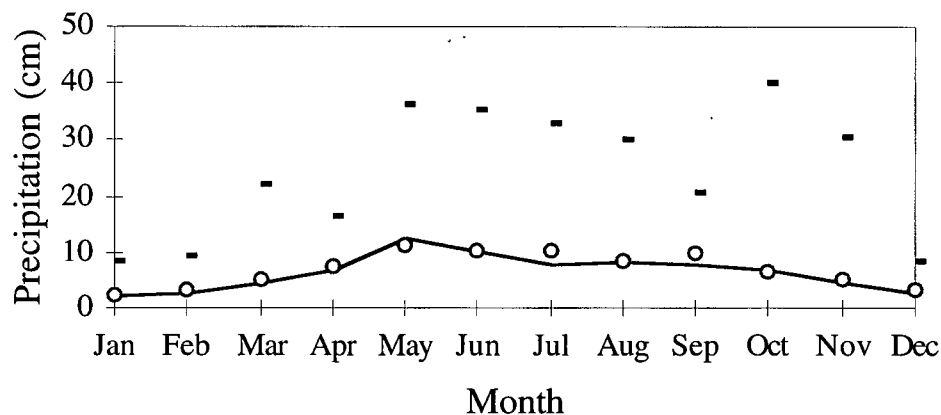


Fig 3.3. Monthly average precipitation at Ponca City (lines) and Enid (circles), Oklahoma. Tick marks show the maximum monthly precipitation at either of the locations (Ruffner 1985)

Intensive Operations Periods (IOPs) occur several times a year at the ARM site. During IOPs more sondes are launched and routine maintenance on instruments is avoided. Regular IOPs occur during each season. Other IOPs, of more limited scope, occur as required by scientists. Data from the Regular Spring 1994, Summer 1994, Summer 1995, and the Surface Energy Exchange IOP (summer 1995) were used to verify the CuP model.

3.1 Instrument Description

3.1.1 Energy Balance Bowen Ratio (EBBR) Instruments

Latent and sensible heat fluxes at most of the extended facilities are measured using energy balance (Bowen ratio) methods. The EBBR is a set of instruments to measure the net radiation near the surface, soil energy storage, soil heat flow, and near-surface gradients of air temperature and moisture. Soil temperature and moisture are measured at five locations around the EBBR at a depth of 0.0 to 0.05 m below ground level (BGL).

Soil heat flux is measured using five soil heat flux plates, 0.05 m BGL. Air temperature and humidity are measured at 0.8 and 1.8 m above ground level (AGL), using an Omega Engineering Inc. Chromel-constant thermocouple and Vaisala Inc. probe. The net radiation is measured at 2.3 m AGL. Atmospheric pressure is measured using a Met One barometer. Uncertainties are presented in appendix A. These instruments sample every 30 seconds. The samples are reduced into five-minute averages (Cook personal communication 1996).

3.1.2 Surface Meteorology Stations (SMOS)

The SMOS measures wind speed and direction at 10 m, air temperature and relative humidity at 2 m, atmospheric pressure at 1 m, rainfall, snowfall, and snow cover. One-second samples of each variable, except for pressure, are taken and then averaged to provide half-hour averages. One-minute samples of atmospheric pressure are taken and averaged to give half-hour averages. The half-hour standard deviation is also reported. Accuracies of the SMOS sensors are reported in Appendix A (Wesely personal communication 1996).

3.1.3 Balloon Borne Sounding System (BBSS)

The BBSS measures profiles of temperature, humidity, wind speed, and wind direction. Launches occur every three hours on the half-hour during regular IOPs starting at 0230 UTC. Thermodynamic variables are sampled every 2 seconds and wind variables are sampled every 10 seconds. The humidity sensor is slow to report high relative

humidities upon entering clouds, and slow to return to lower values when leaving the cloud (Wesely personal communication 1996). Other accuracies are listed in Appendix A.

3.1.4 Belfort Laser Ceilometer (BLC)

The Belfort Laser Ceilometer Model 7013C uses a 976.6 Hz laser and a 30 second time step to measure cloud-base altitude. The ceilometer sampling interval is 5.12 seconds. The instrument's vertical resolution is 7.6 m, with a range of 15 to 7625 m. The BLC has difficulties measuring cloud height in rain, fog, snow and cases with very high thin clouds during periods of strong sunlight (Wesely personal communication 1996).

3.1.5 Micropulse Lidar (MPL) Ceilometer

The Scientific Engineering Services micropulse lidar uses a 2.5 kHz laser. Resolution of the MPL is 300 m with a range of 270 m to 15 km. Sampling time for the MPL is one minute (Wesely personal communication 1996). Turner (1996) found that the BLC reports a slightly higher cloud base than the MPL. Figure 3.4 shows a comparison of cloud-base heights from the MPL and BLC taken at the ARM site. Results from both instruments will be compared to CuP model estimates.

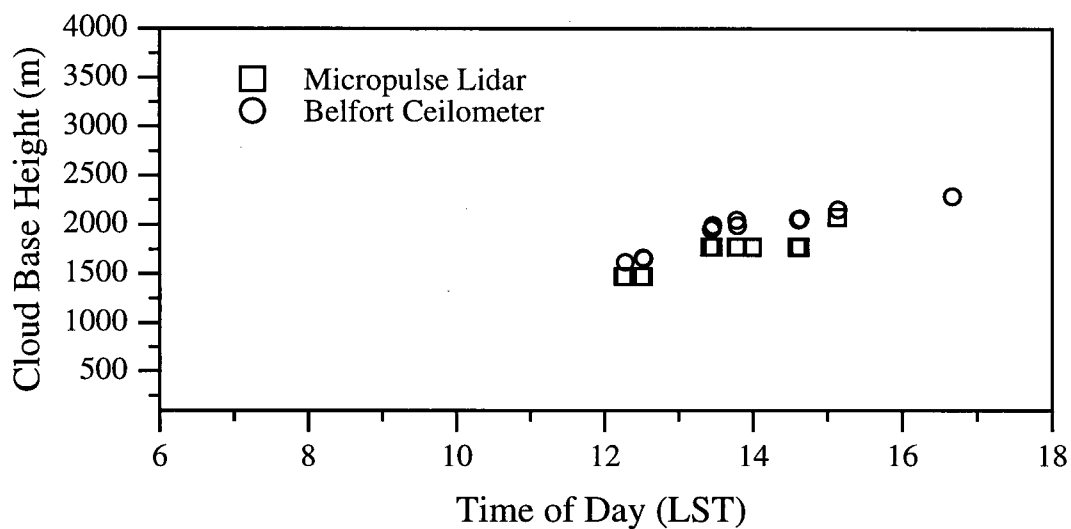


Fig. 3.4. Belfort Ceilometer and Micropulse Lidar cloud base observations for 28 July 1994.

3.1.6 Human Observations

Human observers make hourly observations of cloud coverage, cloud height, and weather observations. Cloud base is reported to within 100 m and coverage is reported in tenths for three levels in each sky quadrant. Stull and Eloranta (1985) showed that human estimates of cloud base height can be inaccurate and they will not be used in this study.

4.0 CuP Model Meteorological Input

4.1 Determination of the Mixed Layer Depth

The CuP model requires the mixed layer depth (z_i) as input. The value of z_i was found using an equal area method from the θ_v profiles (Driedonks 1982). If z_i could not be determined from the profile of θ_v , then the profile of mixing ratio (r), wind direction, wind speed and/or z_{LCL} were used to determine z_i . Conserved variables for both moist and dry adiabatic motions, such as z_{LCL} should be nearly constant through the mixed layer (Betts 1985).

Heights above ground level were found using the hypsometric equation and the temperature and humidity profile from the CF sonde. The CF sonde has a vertical resolution of approximately 10 m for both temperature and moisture.

4.2 Calculation of the Joint Frequency Distribution From Single Stations

Joint Frequency Distributions (JFD) of θ_v and z_{LCL} were made from measurements at the ARM site. Schrieber et al. (1996) found several features that their JFD's shared: strong central tendency about a dominant mode, sharply pointed peak, spread of the distribution along the Bowen ratio and solar forcing axes, asymmetric tails, maximum ranges, and an irregular perimeter.

Values of θ_v and z_{LCL} were calculated from the relative humidity, atmospheric pressure, atmospheric temperature measured at the SMOSs. The saturation vapor pressure was found from the temperature using Tetens's formula (Stull 1988). The vapor pressure

was found using the definition of relative humidity. Teten's formula was inverted to find the dewpoint (T_D):

$$T_D = \frac{35.86 \ln(e/e_{so}) - 4717.31}{\ln(e/e_{so}) - 17.2694} \quad (4.1)$$

The value of z_{LCL} is found using (Barnes 1968, Wilde et al. 1985):

$$z_{LCL} \approx a(T - T_D) \quad (4.2)$$

where a is 125 m K^{-1} . The value of θ_v is found using standard methods (Stull 1988).

The slope of the Bowen-ratio axis and the slope of the solar-forcing axis were calculated using both mixed layer and surface layer variables. Schrieber et al. (1996) showed that the slope of the Bowen-ratio axis (b) can be expressed by:

$$b = a \frac{(1 - B_{ML}/B)}{(1 + \theta_{ML}\beta/B)} \quad (4.3)$$

where B is the surface Bowen ratio, B_{ML} is a mixed layer moisture parameter, θ_{ML} is the mixed layer θ , a is as defined in equation 4.2, and β is a constant equal to $2.44 \times 10^{-4} \text{ K}^{-1}$. Half-hour mean values of Bowen ratio from the CF that bracket the sonde launch time were averaged together for use in the calculations. The slope of the solar-forcing axis (s) can be expressed by (Schrieber et al. 1996):

$$s = a \frac{(1 + B_{ML})}{(1 - \theta_{ML}\beta)} \quad (4.4)$$

Standard deviations along Bowen ratio and solar forcing axes were calculated from the SMOS measured standard deviations of θ_v and z_{LCL} . The standard deviations measured at the CF which bracket the sonde launch timer were combined using the expression for the variance (σ^2):

$$\sigma^2 = \frac{1}{N} \left[\sum_{i=1}^n m_i \sigma_i^2 + \sum_{i=1}^n \left\{ m_i (\bar{c}_i - \bar{c})^2 \right\} \right] \quad (4.5)$$

where N is the total number of observations, n is the number instruments, m_i is the

number of observations made with instrument i , σ_i^2 is the variance reported by instrument i , \bar{c}_i is the mean value reported by instrument i , and \bar{c} is the population mean. The standard deviations were converted into the Bowen ratio, solar forcing coordinate system using simple geometric arguments (Schrieber et al. 1996). Cutoffs along the Bowen ratio and solar forcing axes were set to twice the measured standard deviation.

Schrieber et al. (1996) computed JFDs from fast-response instruments on an aircraft. No area-average fast-response measurements were made at the ARM site during 1994-95, so slow-response (approximately 1 Hz) instruments near the CF were used. The hypothesis to be tested is whether the half-hour mean and standard deviations computed by the slow-response sensors at a single point would be an adequate substitute for those found by the more costly fast-response instruments on an aircraft sampling a broader area.

Using all of the stations at the ARM site is not justified due to the mesoscale variations that typically occur in the atmosphere. Temperatures and humidities measured far from the CF are not representative of the conditions close to the CF. Stull and Eloranta (1985) found that observed z_{LCL} were not correlated with distant cloud-base height, but were almost perfectly correlated with local cloud-base height.

Therefore, only one SMOS, located at the Central Facility was used to calculate the single station JFDs. The station was located at 36.07° N, 97.49° W. A disadvantage of using only one SMOS is that it is not representative of the region. It is located over pasture, so crop land and other land uses will not be represented in the JFD.

4.3 Calculation of Mixed Layer θ_v and z_{LCL}

Values of θ_v were calculated at each level of the profile using the methods described in section 4.2. Mean mixed layer values of θ_v ($\overline{\theta_{v,ML}}$) were calculated by simply averaging over the points in the interior of the mixed layer. The starting point was taken to be 500 m, the height at which the sondes become reliable in a convective-boundary layer (Wesley personal communication). The stopping points for the average, which were near the top of the well-mixed layer, but below the base of the capping inversion, were found by eye. When the mixed-layer depth was less than 500 m the average was taken over the layer of nearly constant θ_v .

Values of z_{LCL} through the mixed layer were calculated from the sondes using a parcel method, rather than equation 4.2 which was used to determine z_{LCL} from surface sensors. A parcel from each level of the temperature profile was lifted by small increments while recalculating temperature until the parcel cooled to saturation; this height was assumed to be z_{LCL} . Comparisons in appendix B between the parcel method and equation 4.2 show that both methods yield nearly identical results in the boundary layer.

Mixed-layer averages of z_{LCL} ($\overline{z_{LCL,ML}}$) were computed by taking the average over the interior of the mixed layer using the same endpoint altitudes used for $\overline{\theta_{v,ML}}$. The average over the entire layer was used even in the cases where z_{LCL} increased slightly with height.

4.4 Error Analysis

Uncertainties in measured quantities are propagated through the calculations to determine errors in z_{LCL} and θ_v . Uncertainties in measured relative humidity, atmospheric pressure and atmospheric temperature from the SMOS are given in appendix A. Details of the error propagation calculations are given in appendix C. Table 4.1 shows typical uncertainties for z_{LCL} and θ_v found from the SMOS.

Table 4.1. Average, standard deviation, maximum and minimum errors for the SMOS. Data was taken from all of the case-study days

	SMOS	
	z_{LCL} Error (m)	θ_v Error (K)
Average	167.97	0.71
Standard Deviation	53.87	0.31
Max Error	437.73	2.28
Min Error	103.30	0.46

The uncertainty in the surface Bowen ratio is thought to be $\pm 5\%$ (Cook personal communication). However near sunrise and sunset the measurement errors using the Bowen ratio method can be quite large (Stull 1988).

The sonde instrument uncertainties should not have a large effect on predicted cloud cover because they are reduced when the mixed-layer average is computed. But the instrument uncertainties from the SMOSs could have an important effect.

There are sampling uncertainties in the representation of the environment by both the sondes and surface instruments. Uncertainties arise because the sonde and surface instruments provide only a point measurement in a continuously varying field. In addition,

sondes only provide a point measurement in time, they may rise through an active thermal or an area of weak subsidence between thermals. The uncertainty was estimated to be on the order of ± 0.5 K for θ_v and 150 m for z_{LCL} , as observed from data collected during the Boundary-Layer Experiment 1996 (Stull et al. 1996). Uncertainties in z_i measured from a sonde profile can be as large as $\pm 0.5 z_i$.

Uncertainties in the JFD parameters, the slopes of the axes and the standard deviations, were estimated from the known instrument uncertainty and the environmental sampling uncertainty. The same error propagation methods were used to trace this error through the calculations of the JFD parameters. Results using typical values of the variables are listed in table 4.2. The affect of the instrument and environmental errors on the CuP predictions will be discussed in section 7.1.

Table 4.2. Propagation of errors through calculations of mixed layer variables and JFD parameters. Errors in the calculated JFD means from the SMOSs are listed in table 4.1.

Variable	Instrument Uncertainty	Environ Sampling Uncertainty	Total Uncertainty
$\overline{\theta_{v,ML}}$ (K)	± 0.02	± 0.5	± 0.52
$\overline{T_{D,ML}}$ (K)	± 0.06	± 1.0	± 1.06
$\overline{z_{LCL,ML}}$ (m)	± 8	± 140	± 148
Bowen Ratio Slope ($K m^{-1}$)	± 0.003	± 0.005	± 0.008
Solar Forcing Slope ($K m^{-1}$)	± 0.00001	± 0.0004	± 0.0004
Bowen Ratio Standard Deviation (m)	± 3	± 7	± 10
Solar Forcing Standard Deviation (K)	± 0.2	± 0.3	± 0.5

5.0 Case Study Days

The CuP model was tested against nine case-study days from the Spring 1994, Summer 1994, and Summer 1995 IOPs. Criteria for test days were: weak pressure gradients with light winds, the formation of boundary-layer cumulus or clear conditions, and free convection. Cloud type and amounts were taken from human surface observations made at the CF. Free-convective conditions were determined from the wind profile in the mixed layer. Such free-convective cases should have light winds or little wind shear with height. Details of the cloud and hourly observations are in Appendix D.

5.1 Date: 1 May 1994

A weak upper-level ridge over the Texas panhandle moved to the east and weakened, while the 50 kPa flow over the CF was nearly zonal. A surface high, located near Kansas City drifted to the southeast. The CF was under a region of weak surface pressure gradient. Overnight skies changed from overcast to clear. Some fog formed in the low-lying areas around the CF. Cumulus-humilis clouds were reported through the late morning and afternoon. Winds shifted from northerly to southeasterly near noon. Wind speeds ranged from 1 to 6 m s⁻¹. Temperatures at the CF ranged from 6.9 to 15.4 °C.

5.2 Date: 27 July 1994

A trough located over Lake Michigan, and a ridge centered over Nevada dominated the weather. Winds at 50 kPa over the CF were from the northwest. The CF was under a large region of high surface pressure with little pressure gradient. Wind speeds ranged

from 3 to 8 m s⁻¹. Wind direction shifted from northwesterly to northly near 1200 LST. Some dew, haze, altocumulus and cirrocumulus were reported in the morning. In the afternoon cumulus humilis and a small amount of cirrocumulus were reported. Temperatures at the CF ranged from 14.4 to 27.3 °C

5.3 Date: 28 July 1994

The trough over the eastern US deepened and continued to move toward the east. The ridge to the west weakened and moved over Utah. The CF was under a region of high surface pressure with weak pressure gradients. Winds throughout the day were northwesterly with speeds ranging from 0 to 5 m s⁻¹. Morning fog, dew, and haze were reported at the CF. Altocumulus clouds were reported in the morning. Throughout the afternoon cumulus humilis, along with some periods of cirrocumulus and cirrus, were reported. Temperatures at the CF ranged from 16 to 28 °C.

5.4 Date: 31 July 1994

An upper level trough reaching from Lake Michigan to Arkansas moved to the east and weakened, while a ridge over the southwestern US shifted east. The CF was under an area of weak cyclonic curvature at 50 kPa. At the surface the CF was under a ridge of high pressure with a moderate gradient. Surface winds were southerly with speeds ranging from 5 to 9 m s⁻¹. The temperature at the CF ranged from a low of 18 to a high of 30 °C. Cirrocumulus were observed overnight and into the morning. Altocumulus, dew, and fog were observed in the morning. Cumulus humilis and some periods of altocumulus, cirrus,

and cirrostratus were observed in the afternoon. A tornado was spotted 72 km northwest of the CF at 1600 LST.

5.5 Date: 27 June 1995

A 50 kPa trough was located over the Mississippi valley and a weak 50 kPa ridge over Utah and Colorado remained stationary throughout the day. The 50 kPa winds over the site weakened throughout the day. An area of surface high pressure moved from southwestern Nebraska into Kansas and weakened. Pressure gradients over the the CF were weak, and the pressure over the CF dropped slightly during the afternoon. Surface winds were light, ranging from 0 to 4 m s⁻¹, and changed from northwesterly in the morning to southerly in the afternoon. The temperature at the CF ranged from 17 to 34 °C.

5.6 Date: 6 July 1995

An upper-level ridge over the southwestern US began to strengthen, while the upper-level trough over the central US continued to move eastward. The CF was under the transition region between the 50 kPa ridge and trough. Winds at 50 kPa were northwesterly. A low-level trough began to develop over western Kansas causing surface winds in the region to change from northwesterly to southerly. Winds overnight from 5 to 6 July were light and southwesterly. The CF was under a region of high pressure, the pressure gradient was weak in the morning, but strengthened in the afternoon. Winds throughout the day were variable with speeds ranging from 0 to 5 m s⁻¹. Low-level moisture flow into the region increased with the southerly winds. Temperatures at the

central facility ranged from 18 to 40 °C. Altocumulus were reported overnight and into the morning. Cumulus humilis were reported throughout the day. Smoke was observed at the CF.

5.7 Date: 9 July 1995

An upper-level ridge over Colorado moved to the east during the day, while a weak surface trough moved over the southern portions of the site. The CF remained between the 50 kPa ridge and a trough to the east. Winds at 50 kPa changed from northwesterly to northeasterly during the day. Several isolated thunderstorms developed along the trough and moved east. A weak surface high moved in the northern areas of the ARM site and dissipated. Surface pressure gradients over the CF were weak. No low-level clouds were reported. Some mid-level clouds were reported between 0500 and 0800 LST. Temperatures at the CF ranged from 22 to 38 °C.

5.8 Date: 11 July 1995

An upper-level ridge moved over the site while a weak 50 kPa trough began to form over the western US. Near sunrise a surface trough was located over the site. Winds were southerly and light in the morning. Surface pressure gradients over the CF strengthened some during the day. Peak wind speeds near 6 m s⁻¹ were observed between 1400 and 1500 LST. Haze and smoke were observed at the CF throughout the day. Altocumulus was reported in the mid-morning. Temperatures ranged from 22 to 45 °C. No low-level clouds were reported on this day. Smoke from many wheat-field fires was reported during the day.

5.9 Date: 13 July 1995

The ridge aloft continued to drift slowly past the CF. An area of low pressure from the northern plains began to move southward. Surface pressure gradients at the CF remained weak. During the day showers and thundershowers developed over the northwestern areas of the site. Surface winds at the CF were southerly with speeds ranging from 0.4 to 4.9 m s⁻¹. Temperatures ranged from 24 to 41 °C. Light haze and smoke were reported throughout the day. Altocumulus and cirrocumulus were observed in the mid-morning. Cumulus humilis were reported in the mid-morning and in the afternoon.

6.0 CuP Model Sensitivity

Each of the JFD parameters: the slope of the Bowen-ratio and the solar-forcing axes, the standard deviations along the Bowen-ratio and solar-forcing axes, the mean value of z_{LCL} , and the mean value of θ_v were changed independently to test the sensitivity of the CuP model. Ranges of input parameters were chosen to cover at least the measurement error, or at least the range of values observed over all days and times studied. Only a subset of the model runs were duplicated for sensitivity tests. Dates and times used are listed in table 6.1. The mean value of θ_v and z_{LCL} of the JFDs were set to the mean mixed-layer values for the sensitivity tests.

Table 6.1. Times (LST) shown in sensitivity plots for each cloudy day

27 June 95	6 July 95	13 July 95
1128	1130	1131
1430	1431	1420

6.1 Changes in the Mean of the JFD

The value of z_{LCL} was allowed to range ± 2000 m from the measured mean value of z_{LCL} used in the original calculations. Figure 6.1 shows how cloud cover changes relative to the difference between the measured z_{LCL} and a test value of z_{LCL} . Although the curves are different they share the same general features. As the JFD is allowed to get more moist the amount of cloud cover increases nearly 50%. Fifty percent cloud cover is not reached because of the discrete bin sizes used to represent the JFD in the CuP model. As the JFD is

allowed to dry, the amount of cloud cover decreases to zero. Between is an area of rapid change near the measured value of z_{LCL} .

In the sensitivity studies the 50% limit on cloud cover occurs because the mean θ_v of the JFD has been set to the mixed layer mean value. Half of the parcels would be too cool to rise and form clouds regardless of the humidity. In the real atmosphere the JFD might be at a temperature warmer than the mean mixed layer value so that cloud cover greater than 50% could occur. Research is ongoing to help determine the relationship between the JFD and the θ_v profile.

The strange step appearance in the cloud cover curves near 40% cloud cover are the result of a warm layer below z_i that exists in the observed profiles. In the CuP model these warm layers can stop a rising parcel before it reaches the capping inversion. Once z_{LCL} drops below the warm level, the cloud cover increases.

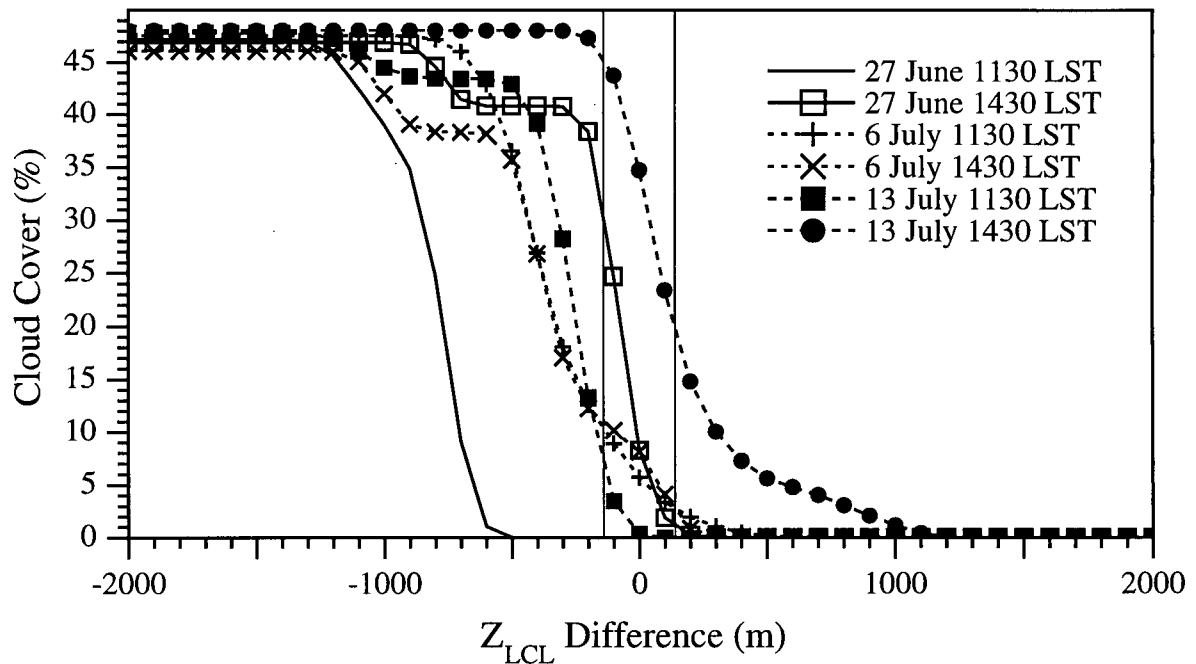


Figure 6.1. CuP model sensitivity to changes in z_{LCL} for selected times on each day. The z_{LCL} difference is the difference between the measured mean z_{LCL} value and the value used in the sensitivity test. Vertical lines indicate typical uncertainty.

The mean value of θ_v was allowed to vary $\pm 8^\circ\text{C}$ from the measured value. Cloud cover values ranged from 0 to 100% over this temperature range (figure 6.2). The curves are similar to those found for the sensitivity to z_{LCL} . In most of the cases the mean θ_v is in a region where the CuP model is very sensitive. Only near predicted cloud cover of 0 and 100% is the CuP model not sensitive to the mean θ_v value. The slope of the sensitivity curves is about the same for all the times tested.

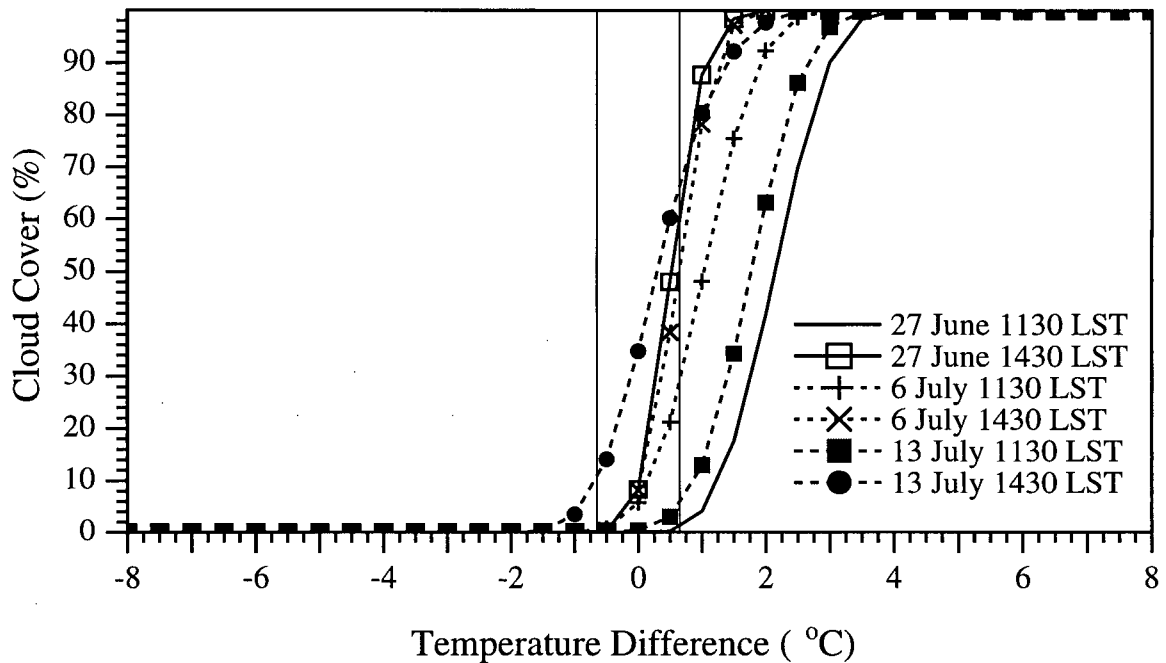


Figure 6.2. CuP model sensitivity to changes in θ_v for selected times on each day. The θ_v difference is the difference between the measured mean θ_v value and the value used in the sensitivity test. Vertical lines indicate typical uncertainty.

6.2 Slope of Bowen-ratio Axis

The slope of the Bowen-ratio axis was allowed to range over $\pm 0.15 \text{ K m}^{-1}$ from the calculated values. Typical slopes are close to $-1 \times 10^{-2} \text{ K m}^{-1}$; the range includes all reasonable values of the slope. Note that the slopes presented are the inverse of the usual definition of slope.

Figure 6.3 shows a plot of cloud cover as a function of the difference between the Bowen-ratio slopes for the times listed in table 6.1. The CuP model is moderately sensitive to the Bowen-ratio slope for most times. Each of the curves has a minimum as the slope of the Bowen-ratio axis approaches the slope of the solar-forcing axis. The JFD is undefined when the slopes are equal.

The slopes of the axes approach each other as the mixed-layer Bowen ratio approaches the negative of the mixed layer θ_v times a constant as defined in equation 4.4. But a negative mixed-layer Bowen ratio was not observed on any of the case study days, and would be unlikely to occur in a convective mixed layer.

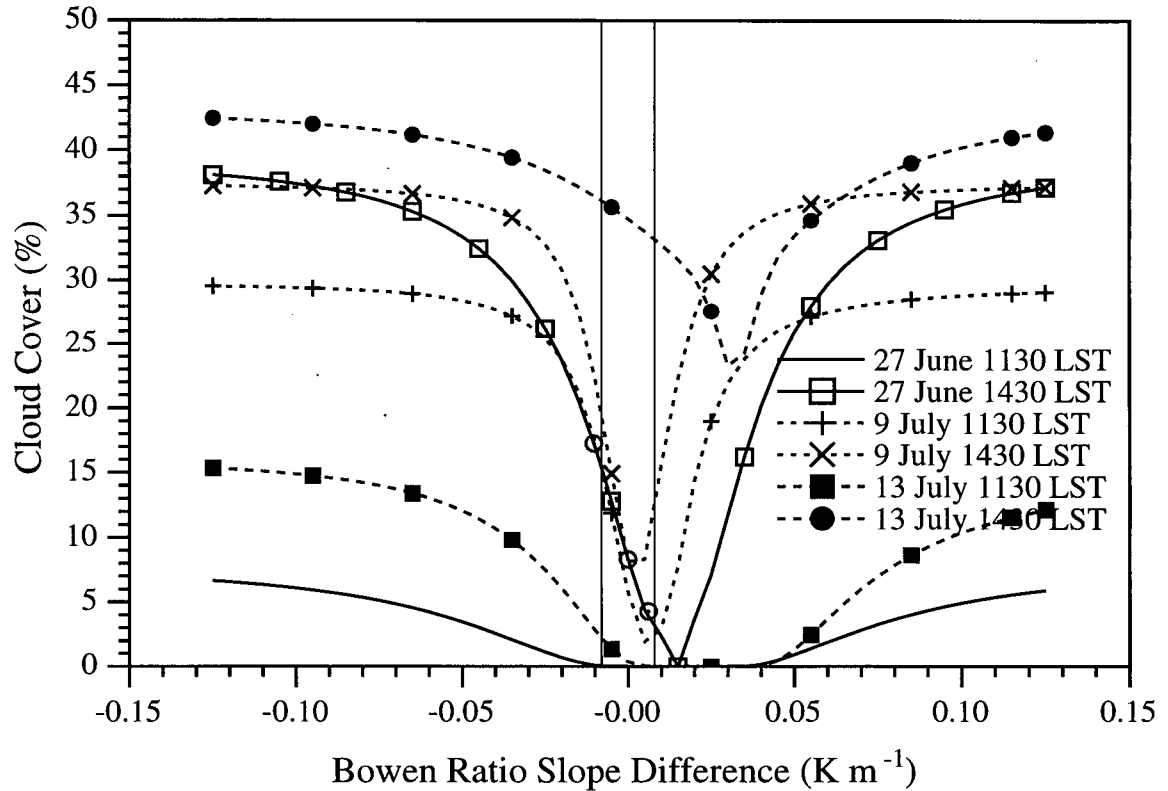


Figure 6.3. CuP model sensitivity to changes in the slope of the Bowen-ratio axis for selected times on each day. The Bowen-ratio slope difference is the difference between the measured mean slope of the Bowen-ratio axis value and the value used in the sensitivity test. Vertical lines show typical error. Closed circles correspond to the slopes used in figure 6.4.

The compression occurs because of the way the standard deviations of the distribution are specified. They are calculated in terms of θ_v and z_{LCL} and then projected into the Bowen-ratio and solar-forcing coordinate system. Sample standard deviations have been added in figure 6.4, these lines are not the ones used in the calculations, but serve as an example. As the slope gets tilted toward vertical the distance along the solar-forcing axis represented by the standard deviation decreases. This causes the JFD to be compressed along that one axis.

A negative change in the slope of the Bowen-ratio axes corresponds to a moistening of the surface layer or the drying of the mixed layer. As shown in figure 6.4, as the slope gets smaller the central frequency of the JFD increases and the spread along the minor axis decreases. This compression of the JFD along the minor axis, with little increase in the length of the major axis causes the central frequency to increase.

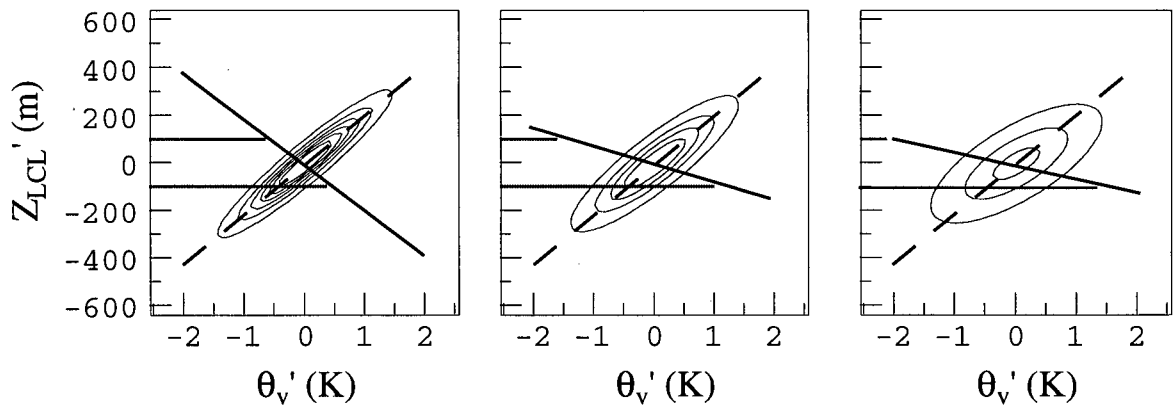


Figure 6.4. Plot of JFD with different Bowen-ratio axis slopes. The plots are made using data from 27 June 1995 at 1430 LST. Deviations of the θ_v and z_{LCL} are the axis labels. From left to right the slopes are: -5.17×10^{-3} , -1.03×10^{-2} , -2.06×10^{-2} ($K m^{-1}$). The first contour is at 0.001, with an interval of 0.002. Broken lines mark the solar-forcing axis, solid lines the Bowen-ratio axis. Horizontal lines at 100 and -100 m represent a hypothetical standard deviation.

6.3 Slope of the Solar-Forcing Axis

To test the sensitivity of the CuP model to changes in the slope of the solar-forcing axis, slope values were allowed to vary from $\pm 0.01 K m^{-1}$. This allowed the slope of the solar-forcing axis to change by a factor of three. Only positive values of the slope of the solar-forcing axis have physical meaning so negative values are not allowed. Figure 6.5

shows how the predicted cloud cover changed as a function of the difference between the tested solar-forcing slope and the measured values.

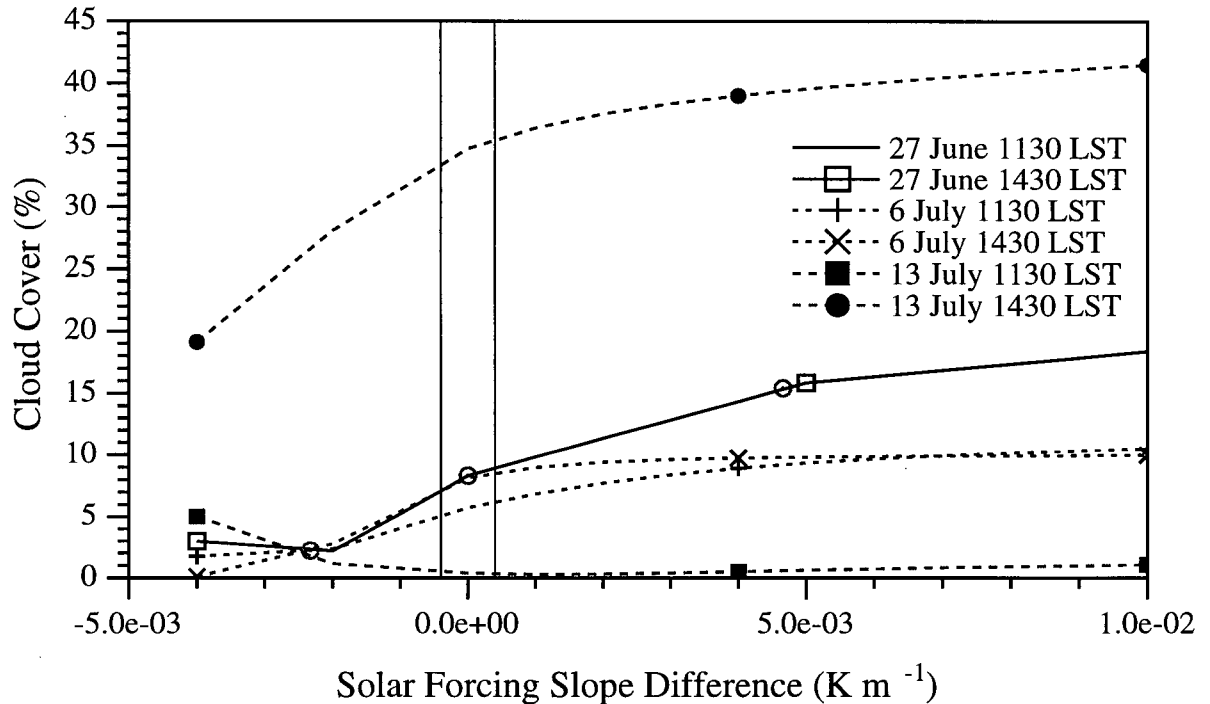


Figure 6.5. CuP model sensitivity to changes in the slope of the solar-forcing axis for selected times on each day. The solar-forcing slope difference is the difference between the measured mean slope of the solar-forcing axis value and the value used in the sensitivity test. Closed circles correspond to the slope difference used for figure 6.6.

As the slope of the solar-forcing axis approaches horizontal the JFD gets compressed along its major axis, the central frequency becomes larger, and the JFD gets tilted to the right (figure 6.5). The physical explanation for this behavior is the same as was presented in section 6.2, although the standard deviations are specified in terms of θ_v . Although the central frequency is larger the JFD spans a larger θ_v range than at smaller values of slope. For the days with observed cloud cover, the tilting of the JFD to the right, and the stretching would cause the cloud cover to increase. The value of slope used

in figure 6.6 is marked on figure 6.5. An increase in slope of the solar-forcing axis can be caused by an increase in the mixed-layer Bowen ratio, or an increase in the mixed layer θ_v .

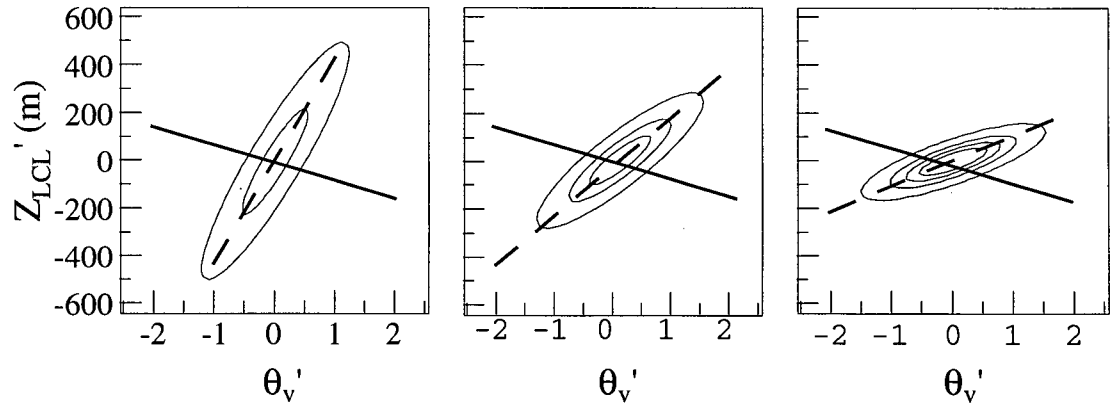


Figure 6.6. Plot of JFD with different solar-forcing axis slopes. The plots are made using data from 27 June 1995 at 1430 LST. Deviations of the θ_v and z_{LCL} are the axis labels. From left to right the slopes are: 2.33×10^{-3} , 4.66×10^{-3} , 9.32×10^{-3} ($K m^{-1}$). The first contour is at 0.001, with an interval of 0.003. Broken lines mark the solar-forcing axis, solid lines the Bowen-ratio axis.

6.4 Bowen-ratio and Solar-Forcing Standard Deviations

The sensitivity of the CuP model to both the Bowen-ratio and solar-forcing standard deviations was also tested. The standard deviation along the Bowen-ratio axis was allowed to vary from ± 100 m, while the standard deviation along the solar-forcing axis was allowed to vary by ± 2.0 K.

The model is more sensitive to the standard deviation along the Bowen-ratio axis (figure 6.7). On 27 June 1995 at 1430 LST the model seemed to be more sensitive than on the other days. Doubling the standard deviation caused the estimated cloud cover to increase from near 8 to 17%. Reducing the standard deviation by half caused the amount of cloud cover to drop to near 6%. On 13 July 1995 at 1430 LST doubling the standard

deviation caused the cloud cover to increase from 35 to 40%. Reducing the standard deviation by half caused the cloud cover to drop to 31%.

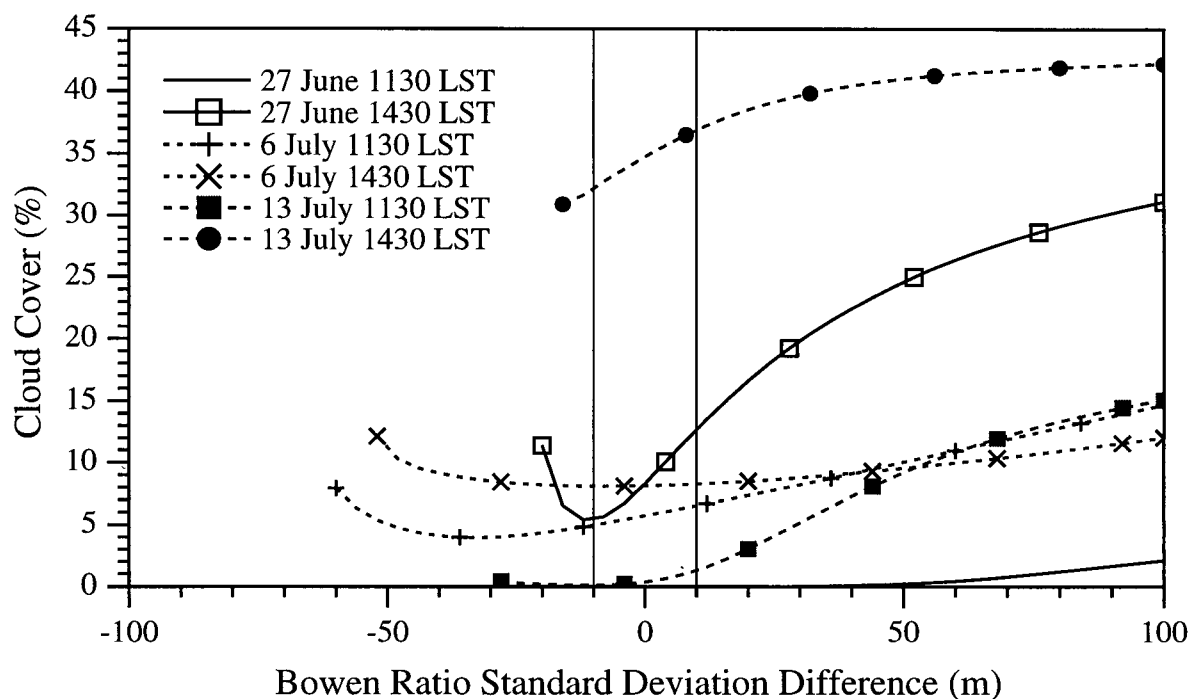


Figure 6.7. CuP model sensitivity to changes in standard deviation along the Bowen-ratio axis for selected times on each day. The Bowen-ratio standard deviation difference is the difference between the measured standard deviation and the value used in the sensitivity test.

The CuP Model shows some weak dependence on the solar-forcing standard deviation (figure 6.8). The most sensitive day was 6 July 1995 at 1430 LST. Doubling of the standard deviation caused the cloud cover to increase from 8 to 18%. Reducing the standard deviation by half caused the cloud cover to decrease from 8 to 4%.

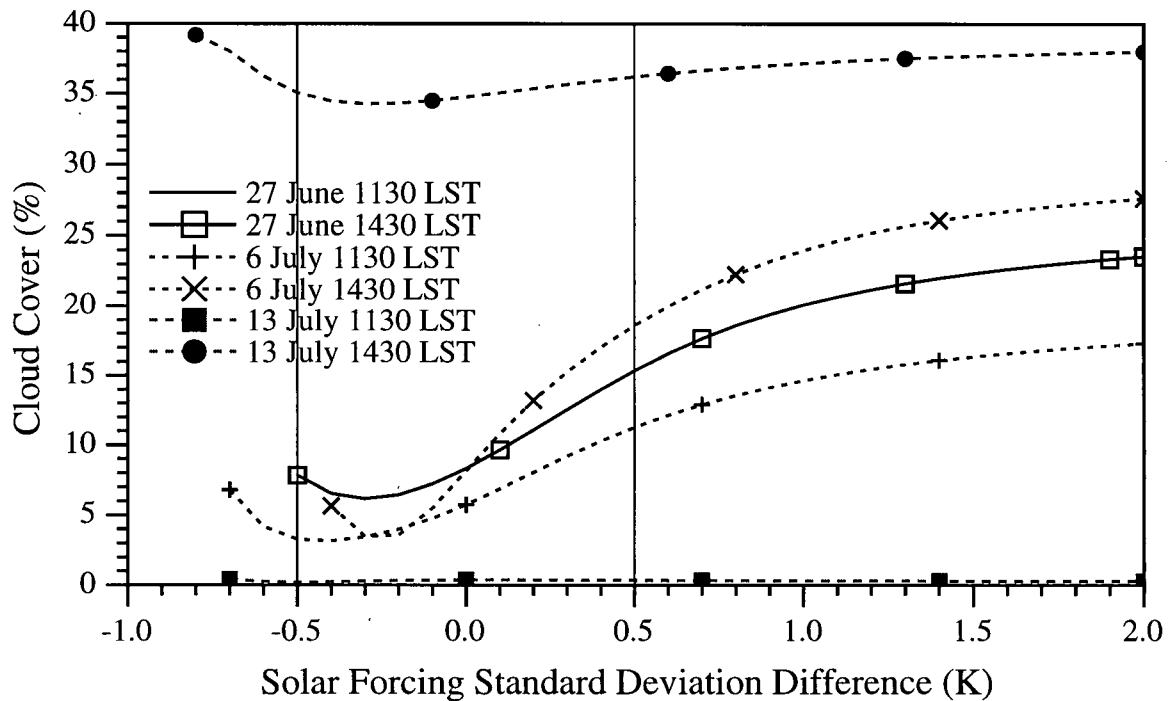


Figure 6.8. CuP model sensitivity to changes in standard deviation along the solar-forcing axis for selected times on each day. The solar-forcing standard deviation difference is the difference between the measured standard deviation and the value used in the sensitivity test.

The relatively weak sensitivity to standard deviation is reassuring. Incorrectly determining the standard deviation should not greatly affect the model results. The model dependence on slopes was less than the dependence on mean θ_v and z_{LCL} . These results are consistent with those of Wetzell and Boone (1995).

6.5 JFD and θ_v Interaction

While not an exhaustive test, the CuP model was run with the same JFD and three contrived θ_v profiles. These tests examine the affect of the θ_v profiles on the model predicted clouds and thermals. Three different θ_v profiles were used. In each case $\overline{\theta_{v,ML}}$

was set to 30 °C, $\overline{z_{LCL,ML}}$ to 1000 m, and z_i to 1000 m. The inversion strength at the top of the mixed layer and the lapse rate above z_i were allowed to change in each case. Figure 6.9 shows the JFD taken from 31 July 1994 at 1430 LST, and the three θ_v profiles.

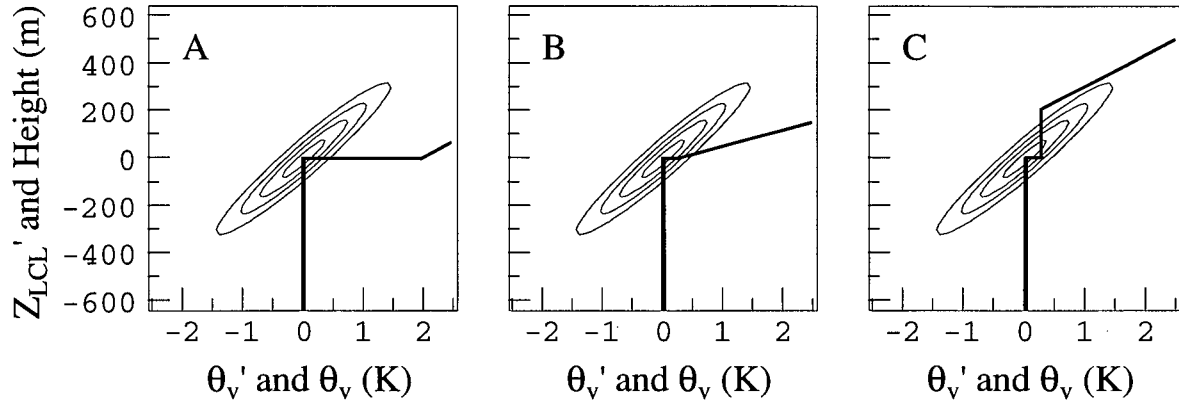
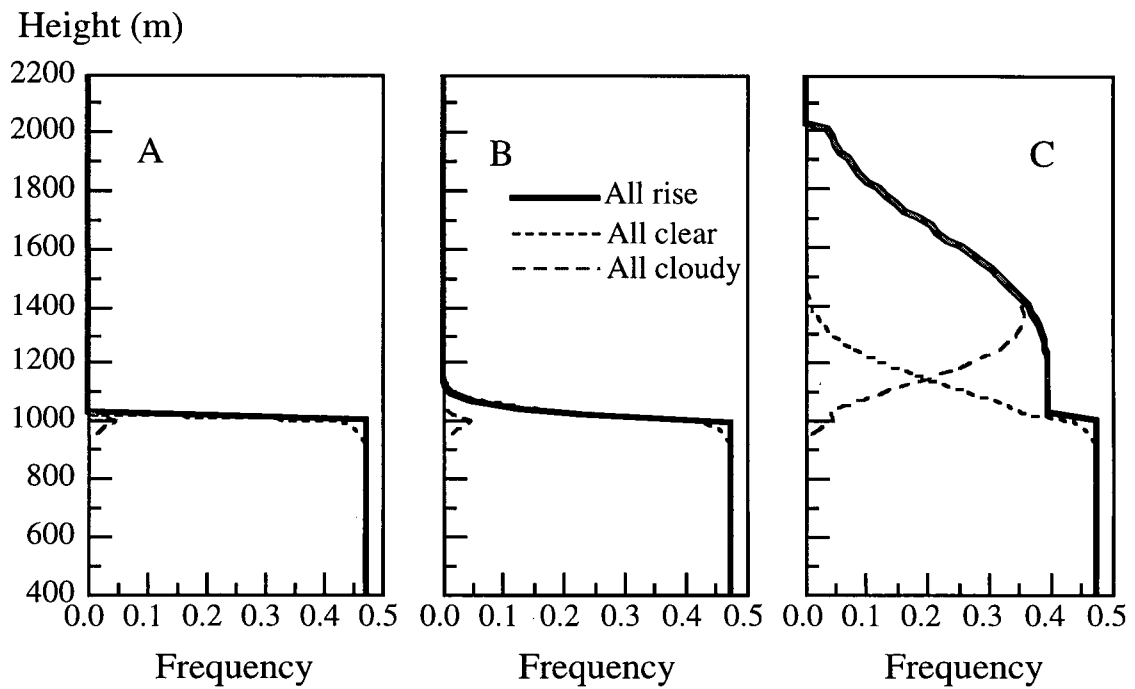


Figure 6.9. JFD and θ_v profiles used to examine affects of changing the θ_v profile. Vertical axis shows the perturbation to $\overline{z_{LCL,ML}}$ or the difference between the height and z_i . The horizontal axis is the $\overline{\theta_{v,ML}}$ perturbation or the θ_v excess or deficit relative to $\overline{\theta_v}$. The same JFD is used in each plot and was take from 31 July 1994, 1430 LST.

Case A has a 2 °C inversion with a stable layer above. Only the small region to the right and below the profile will produce clouds. Figure 6.10 shows the model-predicted thermals. Both clear and cloudy thermals are forced to stop at z_i due to the strong inversion. A small number of cloudy thermals do form, but they are shorter than the clear thermals because the right “end” of the JFD is above the θ_v profile. The range of clear and cloudy thermals is due to the discrete nature of the JFD and the CuP model.

Case B is very similar to case A, but with only a 0.25 °C inversion. In this case there is a larger range of both clear and cloudy thermal tops because of the slope of the θ_v profile (figure 6.10). There are still clear thermals higher than the tallest cloudy thermals because the end of the JFD is still above and to the left of the θ_v profile.

Case C is different. There is a 0.25 °C inversion at 1000 m, then θ_v is constant to 1200 m. Above 1200 m θ_v rapidly increases. The cloud field is much different in this case (figure 6.10). At lower levels all thermals are clear. At a height of 1000 m the thermals begin to reach the lower inversion creating the lowest step appearance. All of the thermals that do not reach their z_{LCL} stop at 1000 m, only clear thermals that will form clouds at higher heights are clear above 1000 m. The number of thermals remains constant up to 1200 m, where the thermals begin to reach the θ_v profile again. Although the total number of thermals is constant, the ratio of clear and cloudy thermals changes above 1000 m, because the clear thermals are reaching their z_{LCL} and the water vapor in the thermal is condensing. Near 1500 m the last remaining clear thermals have become cloudy. Because the slope of the θ_v profile is less than that of the moist adiabat each thermal will reach its level of neutral buoyancy and stop. All three diagrams show patterns similar to those observed on the case-study days, presented in section 7.



6.10. Clear and cloudy updrafts for cases A, B, and C. “All rise” is the sum of clear and cloudy updrafts.

Cloud thickness can also be plotted (figure 6.11). Case C has the most and also the deepest cloud cover, case A has the least and thinnest cloud cover. The unevenness in the curves is due to the discrete nature of the JFD. Smaller bin sizes for θ_v and z_{LCL} make a smoother curve of cloud thickness, but have little affect on the predicted cloud cover.

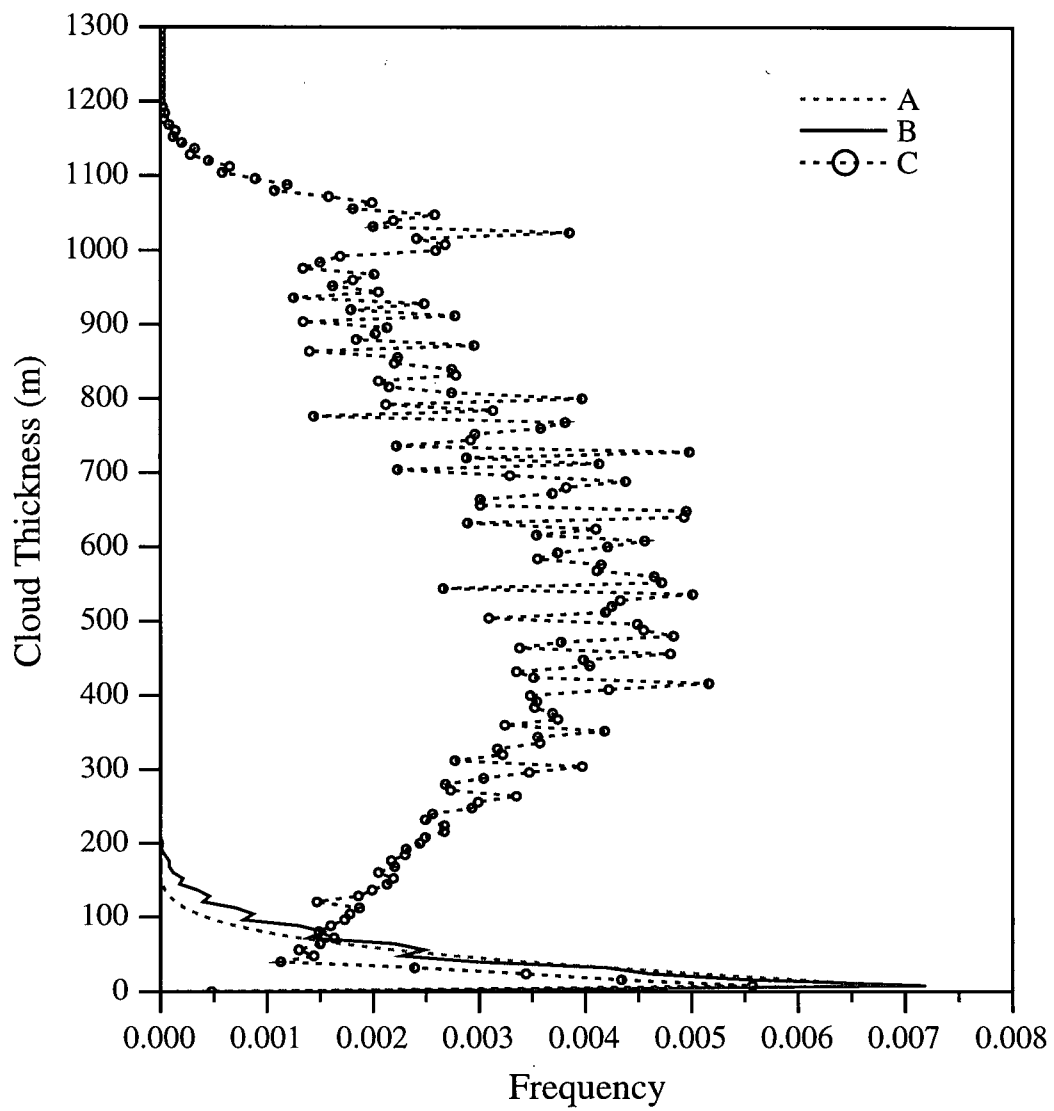


Figure 6.11. CuP predicted cloud thickness for test cases A, B, and C.

7.0 Results

The CuP model was used to predict boundary-layer cumulus clouds on nine days in 1994 and 1995. An overview and discussion of the shortcomings of using a JFD calculated from data collected at a single point will be presented. General results, including typical predictions of cloud thickness will be discussed. Results of the CuP model for the test days will be shown in section 7.4. Plots of observed cloud amount and forecast cloud amounts will be displayed for each day. The CuP model forecasts of cloud base will be compared to BLC and MPL observations.

The CuP model was run for the case study days using the JFD computed as described in section 4 and centered at the surface $\theta_v (\theta_{v,sfc})$ and $z_{LCL} (z_{LCL,sfc})$. To summarize the results, the CuP model predicted cloud cover 45-100% in excess of observed cloud cover in most cases (figure 7.1). Additional experiments were done using the mean mixed layer values of $\theta_v (\theta_{v,ML})$ and $z_{LCL} (z_{LCL,ML})$ as the JFD mean, keeping all other JFD parameters the same. This led to an estimate of cloud cover 0-20% smaller than observed. These latter experiments were conceived because of the nature of mixing in the surface layer as the parcels rise. This mixing hypothesis implies that the driving force behind mixed-layer thermals is not the JFD at a height of several meters, but rather the JFD near the top of the surface layer, where larger mixed-layer thermals are formed.

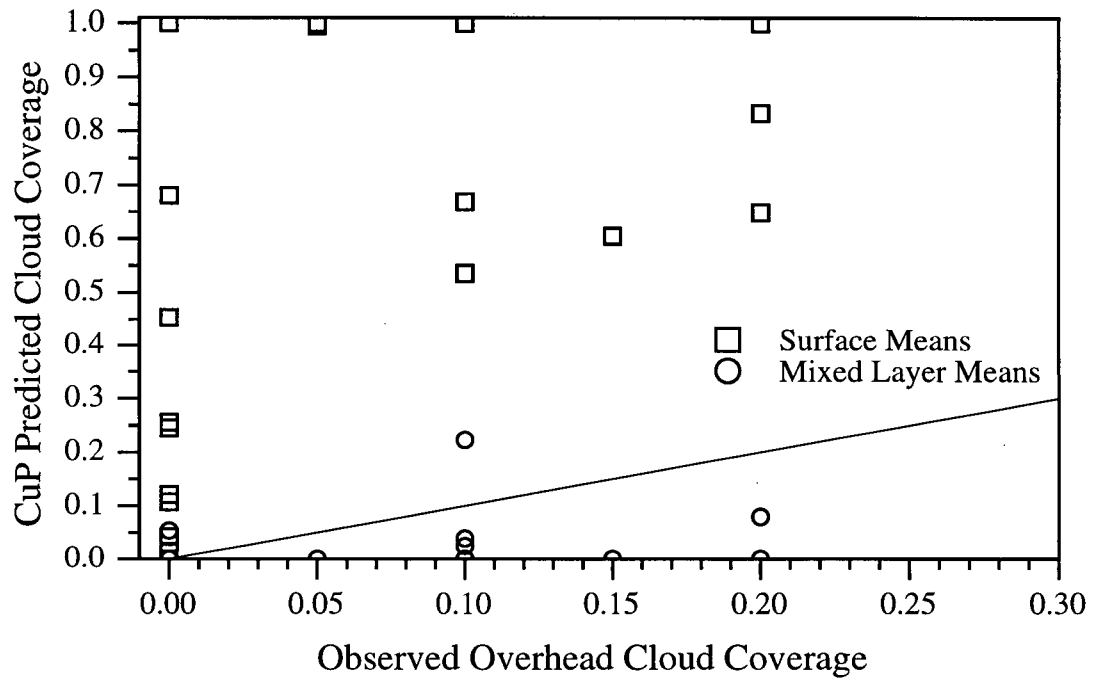


Figure 7.1. Observed and CuP modeled cloud cover. Surface means correspond to cloud forecasts using the calculated JFD set to $\theta_{v,sfc}$ and $z_{LCL,sfc}$. Mixed layer means correspond to cloud forecasts using the calculated JFD set to $\theta_{v,ML}$ and $z_{LCL,ML}$. The solid line has a slope of 1.

7.1 Mixing Line Analysis

A mixing line can be constructed between $\theta_{v,ML}$ and $z_{LCL,ML}$ and $\theta_{v,sfc}$ and $z_{LCL,sfc}$ (figure 7.2). The mixing line traces the range of θ_v and z_{LCL} values of any parcel that consists of a mixture of air from the mixed and surface layers (Betts 1982a, Betts 1982b, and Betts 1985).

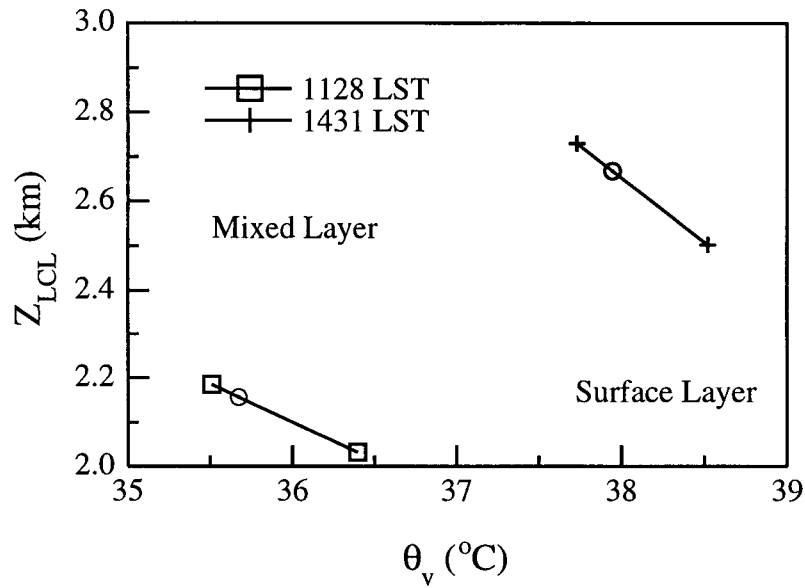


Figure 7.2. Plot of mixing lines connecting and mixed layer and surface θ_v and z_{LCL} for 6 July 1995. Mixed-layer values are at the left end of the line, surface values are at the right end. The circle marks the mixture of θ_v and z_{LCL} where the CuP forecast matches the observed cloud cover on 6 July 1995.

The center of the JFD was allowed to vary along this line to represent the mixing a convective thermal would undergo. A point along each line was found where the CuP model agrees with observations at the CF; this best fit ratio is marked by the circles in figure 7.2. For example, at 1128 LST on 6 July 1995 the CuP model predicted cloud cover matched the observed cloud cover when the JFD was centered at 35.6 $^{\circ}\text{C}$ and 2.15 km. These “best fit” JFD locations will be referred to as $\theta_{v,Best}$ and $z_{LCL,Best}$. The ratios for each day and time were compared to many different combinations of typical mixed-layer mean quantity and flux scales, such as the friction velocity, Deardorff convective velocity scale, surface and mixed-layer temperature scales, z_i , the temperature difference between the surface and mixed layers, and the Obukhov length. No significant correlations were

found. Wetzel and Boone (1995) had a similar difficulty defining the distribution for their cloud forecast model.

7.2 Model Accuracy and Measurement Errors

A test was done assuming that the human cloud-coverage observations at the CF were in error by $\pm 10\%$. The mixture of surface layer and mixed-layer air that gave the best CuP estimate of the observed cloud cover $\pm 10\%$ were found. The range in these values was as large as the scatter of the best-fit ratio for all days. This suggested that cloud coverage is very sensitive to air-parcel mixing, and the similar sensitivity of the CuP model makes forecasts of coverage extremely difficult given typical measurement errors.

These errors could include: 1) the sondes were not representative of the mean mixed layer, and/or 2) the surface-based instruments were not representative of the surface layer over the area. In addition the theory of the CuP model could be incorrect.

The accuracy of the sondes at representing the mean mixed-layer state was addressed in section 4.4 dealing with error analysis. Uncertainties ranged from ± 0.5 K for θ_v and 150 m for z_{LCL} . Doran and Zhong (1995) found that z_i can vary by over 1 km in an area 40 km². Given the sensitivity of the CuP model to the relationship between the JFD and the θ_v profile these differences were substantial.

The accuracy of using only one surface station to form the JFD can also be examined. As discussed in section 4.2, the ARM station used gave a biased sample, it was over pasture. The incorrect estimation of cloud cover could be attributed to sampling error; namely cultivated areas and other land uses were missed in the observations. Most of the

cultivated land in the area was non-irrigated wheat. During July and August these areas would be bare with no evapotranspiration and would have a larger sensible heat flux, θ_v , and z_{LCL} than other areas. Rabin et al. (1990) found that heat flux was the most important parameter for cloud formation. Several smaller JFDs could be used, one for bare ground, another for pasture/range, one for woodlands, etc. These could be added together to form a composite JFD that is more likely to be more representative than one large mono-model JFD (Schrieber et al. 1996).

Given the biased sample, one might have expected the modeled JFD to be too cool, and that too few clouds would be forecast. But this was not the case, even the relatively cool JFD greatly overestimated the cloud cover. This would support the mixing hypothesis presented at the beginning of section 7.1.

There may also be problems in the assumptions made to fit the JFDs to the data. Schrieber et al. (1996) fit JFDs to data collected with fast response sensors mounted on the NCAR King Air that flew over a wide range of heterogeneous landscapes. Rather than use fast response aircraft data, we used observations from slower response surface-based instruments at the single point. It is hoped that the mean and standard deviations reported by these slow-response instruments would give similar results to the aircraft data. The standard deviations of the point measurements were similar to those measured by Schrieber et al. (1996) in France over a broader area.

Another explanation for the performance of the CuP model is that the theory is not valid. Wetzal and Boone (1995) found that a multiple parcel model can give good cloud estimates. However they let parcels mix through the entire mixed layer. This modeling assumption differs from the observations of Crum et al. (1987), who found that some

parcels near the entrainment zone had mixing ratios identical to those measured near the surface, indicating that mixing is not important near the thermal core. Williams and Hacker (1993) found that once a thermal rises above $0.3 z_i$, there is little mixing between the thermal and the environment.

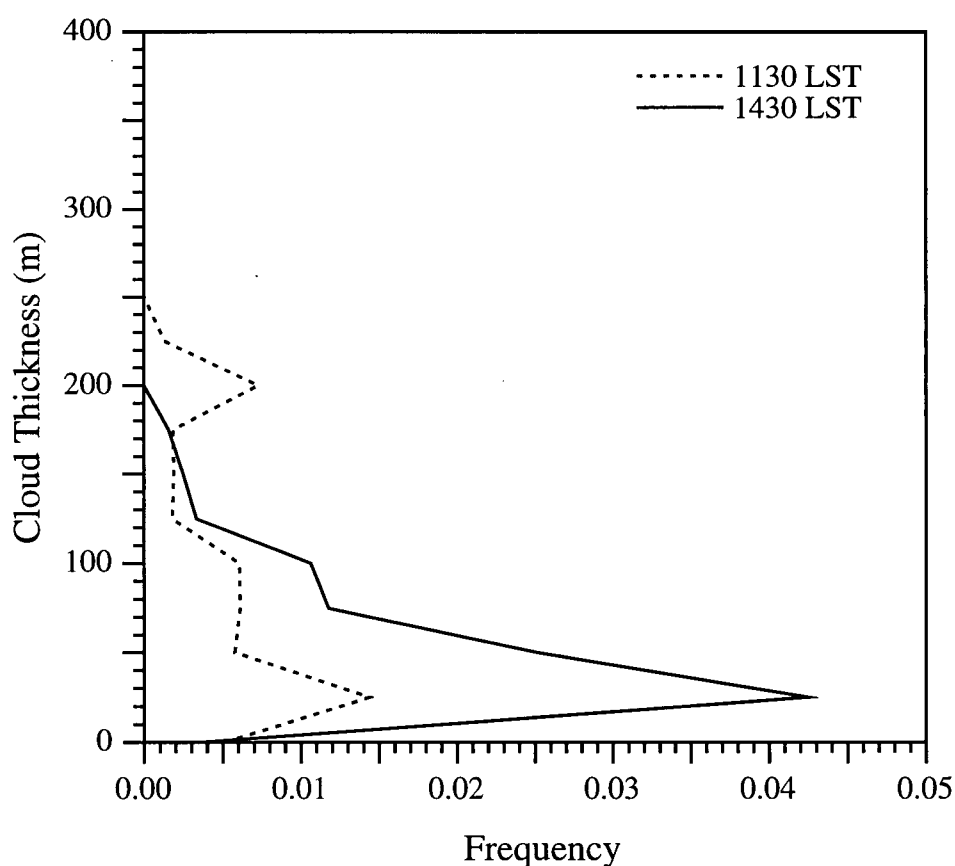
It is impossible, from the data gathered at the ARM site to determine which of the scenarios is correct. The CuP model cloud forecasts will be examined in detail below.

7.3 Detailed Results

7.3.1 Cloud Thickness

Distributions of predicted cloud thicknesses were computed for all of the case study days using a JFD centered at $\theta_{v,sfc}$ and $z_{LCL,sfc}$, $\overline{\theta_{v,ML}}$ and $\overline{z_{LCL,ML}}$, and $\theta_{v,Best}$ and $z_{LCL,Best}$. No measurements were made of cloud thickness at the ARM site so it is impossible to verify this aspect of the CuP model results. Some distributions were bi-modal with a maximum at very thin cloud thicknesses and another maximum at greater thicknesses. The maximum at very small thicknesses can be explained by parcels in which the water vapor condenses just before reaching the top of the mixed layer. The parcel would rise only a short distance before reaching its level of neutral buoyancy in the capping inversion. Other cloudy parcels, in which the water vapor condensed at lower heights, were able to rise, moist adiabatically to much higher heights. These parcels rise beyond the capping inversion because the slope of the moist adiabat was less than that of the θ_v profile. In some cases there were multiple maxima at larger thicknesses. In almost all of the cases the distribution of cloud thicknesses did not trace a smooth curve. This behavior can be

explained by slope changes in the θ_v profile and the discrete nature of the JFD. Cloud tops may form where the slope of the profile was less than the slope of the moist adiabat. Cloud tops cannot occur where the slope of the θ_v profile was greater than the slope of the moist adiabat. The cloud thicknesses were also a function of the mean used to define the JFD. The cloud thicknesses from 28 July 1994 with the JFD centered at $\theta_{v,Best}$ and $z_{LCL,Best}$ are shown as an example (figure 7.3). This plot is typical of the case study days in 1994.



7.3. CuP predicted frequency of a given cloud thickness for 28 July 1994 with the JFD centered at $\theta_{v,Best}$ and $z_{LCL,Best}$. No clouds were predicted at 830 LST.

Much deeper clouds were predicted on the case study days in 1995. Figure 7.4 shows an example of the CuP predicted cloud thickness from 6 July 1995 using a JFD set to $\theta_{v,Best}$ and $z_{LCL,Best}$. While cloud thicknesses are not recorded, the human observer at the

CF reported only cumulus-humilis clouds at the lower levels. Even on days with cumulus-humilis clouds, some deep clouds might be expected, but for the days in question most of the clouds were quite high.

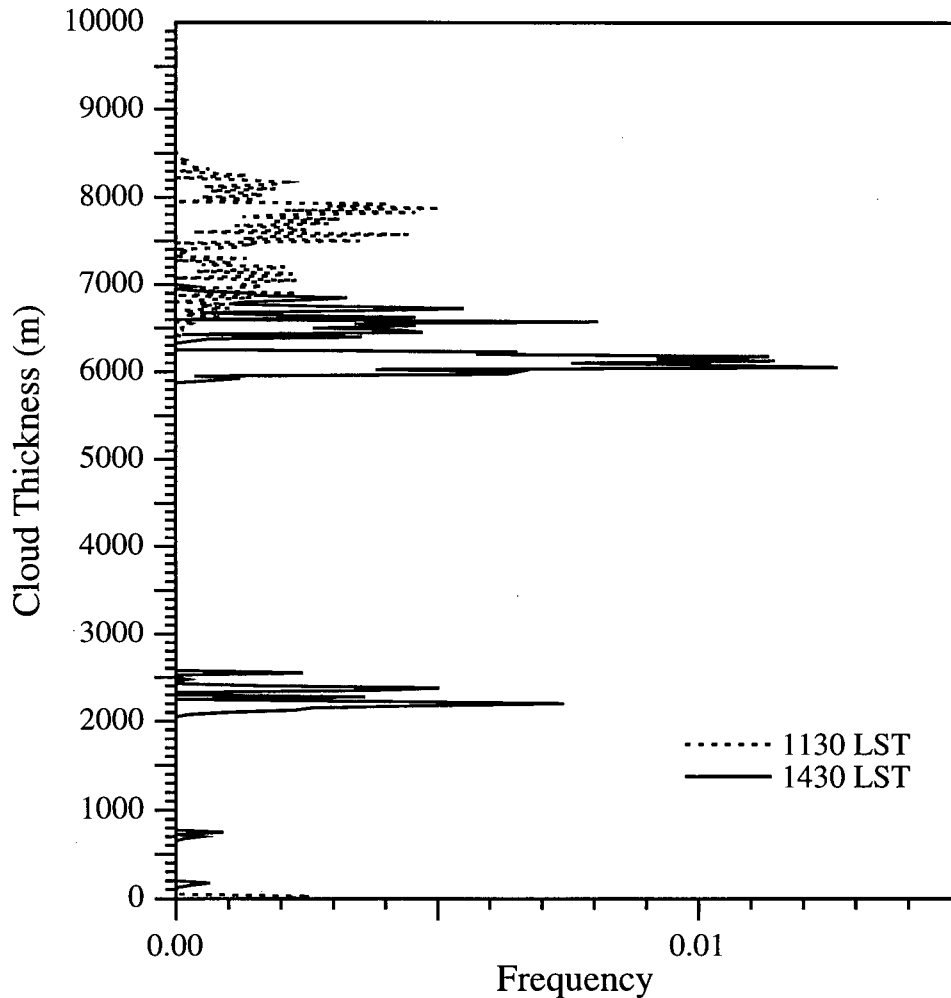


Figure 7.4. CuP predicted frequency of a given cloud thickness for 6 July 1995 using $\theta_{v,Best}$ and $z_{LCL,Best}$ to center of the JFD. No clouds were predicted at 830 LST.

The cause of these tall clouds can be determined from the θ_v profile. Profiles from each of the different days in 1995 were similar in several important ways. Each had a thick nearly moist adiabatic layer, representing the cloud layer. Each plot also had a weak stable

layer above the cloud layer. In the CuP model this allows parcels that reach their z_{LCL} to continue rising well past the observed cloud layer. Figure 7.5 is a plot of the θ_v profile for 6 July 1995. Included in the plot are moist adiabats. In this case there was a moist adiabatic layer from approximately 3.5 to 6 km. The plot shows how a parcel could easily rise to great heights.

The location or size of the JFD could be important in the formation of these deep clouds. But, these results are largely independent of the JFD used. The CuP model did a good job predicting the cloud base altitude (section 7.3.4) indicating that the altitude of the center location of the JFD is not a problem. The size and shape of the JFD was not the cause of the problem either because all of the cloudy parcels are rising to large heights, not just a small fraction. Some other aspect of the cloud-atmosphere system was keeping the clouds from rising to their level of neutral buoyancy.

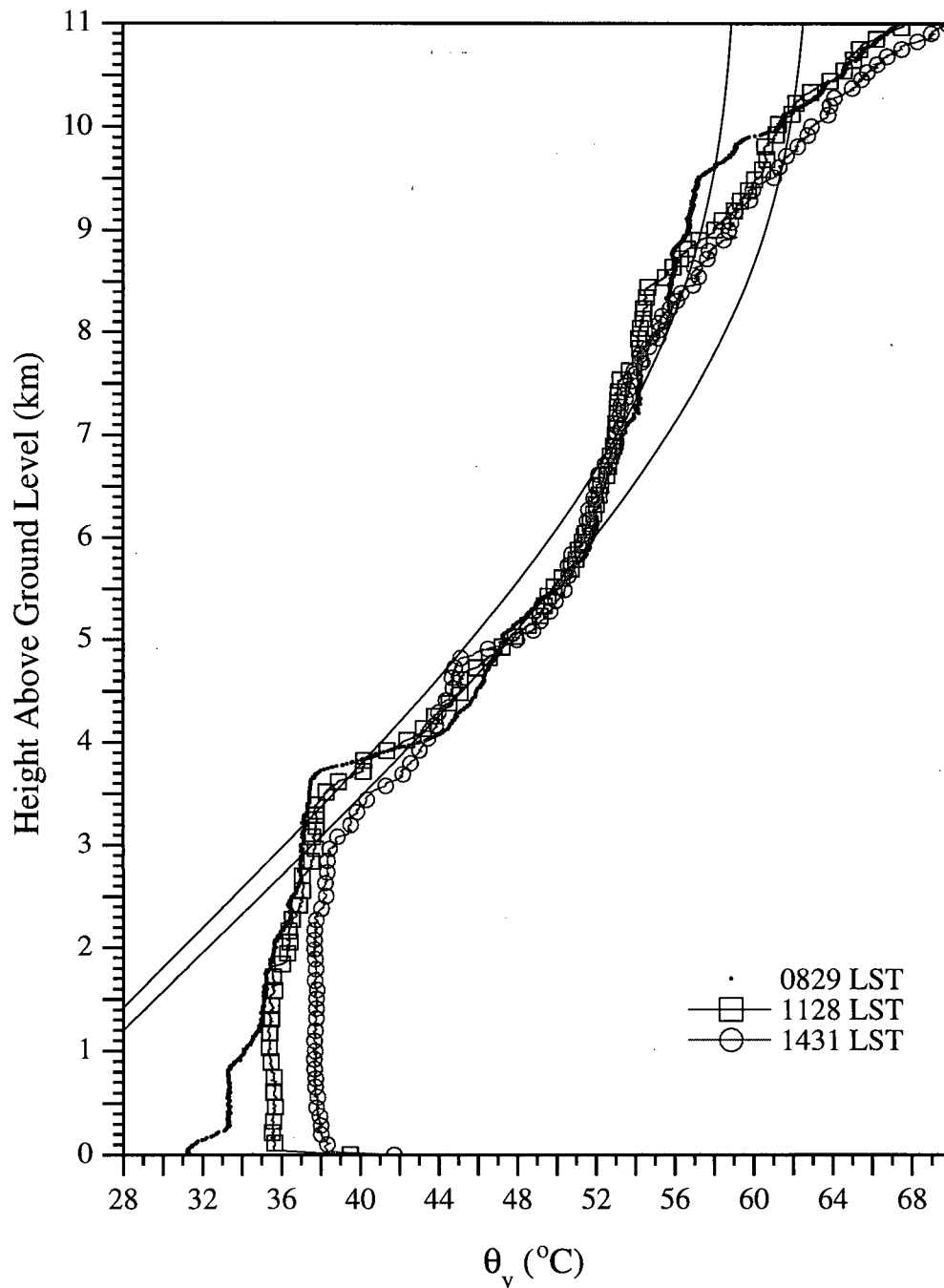


Figure 7.5. Profiles of θ_v taken at the CF on 6 July 1995. Solid lines are moist adiabats.

One possible explanation is cloud mixing. Figure 7.6 is the z_{LCL} profile taken from 6 July 1995. This plot showed a dry layer near 3.7 km. As clouds enter this dry layer they

would be expected to mix with the environment. This mixing with dry air would tend to cool the clouds through evaporation so they would no longer rise moist adiabatically. Each of the days in 1995 had some sort of dry layer above the mixed layer that could provide the needed cooling.

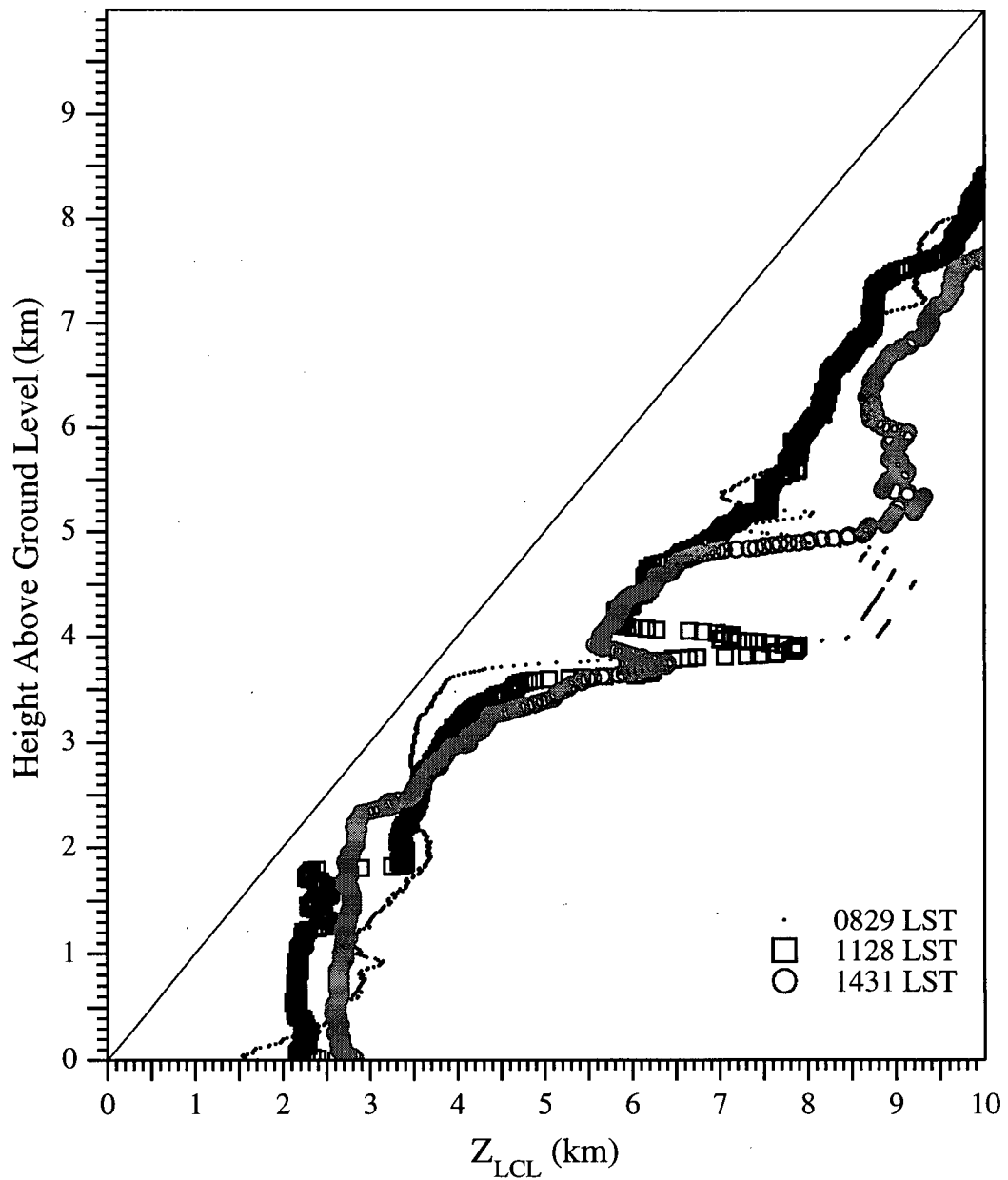


Figure 7.6. Profiles of z_{LCL} taken at the CF on 6 July 1996. Solid line separates clear and cloudy air.

Lopez (1977) found that populations of cumulus clouds form nearly log-normal thickness distributions in both maritime and continental regimes. It is useful to see if the range of cloud thicknesses predicted by the CuP model are also log-normal. A sample from 27 July 1994 is shown in figure 7.7 along with the best fit log-normal curve. On this day the CuP predictions appeared to be log-normal.

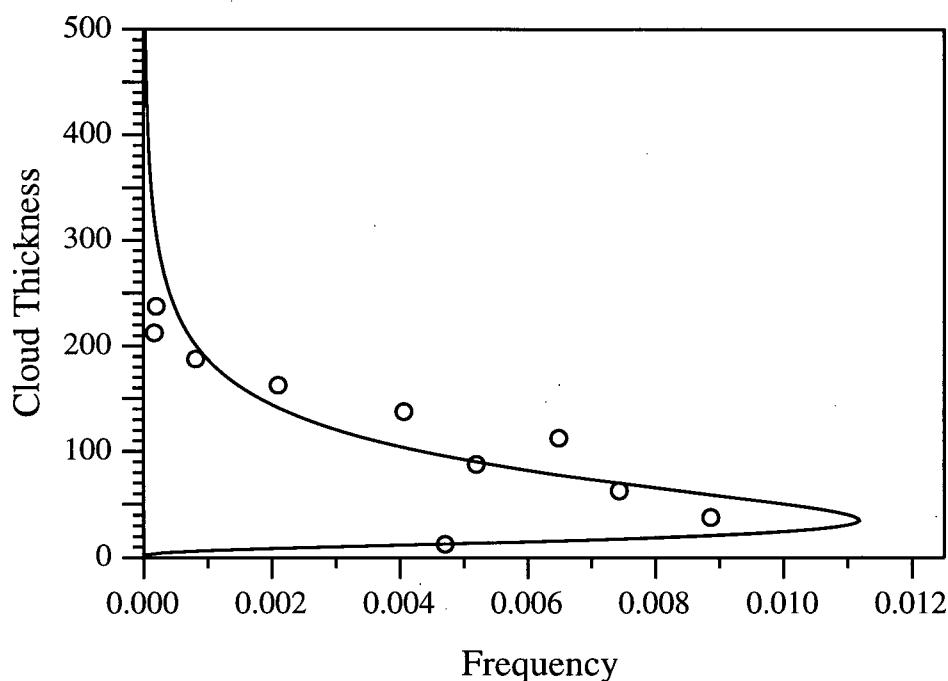


Figure 7.7. Plot of CuP cloud thickness vs. height for 1430 LST on 27 July 1994. The solid line is a best-fit log-normal curve.

The CuP-model estimated cloud thickness along with the best-fit log-normal distributions are shown in figures 7.8a, 7.8b and 7.9. These plots show the logarithm of cloud thickness verses the accumulated frequency on a log-probability scale. In these plots log-normal curves appear as straight lines. The CuP estimates, using the value of $\theta_{v,Best}$ and $z_{LCL,Best}$ to locate the JFD, are marked with symbols in the figures. The straight lines in the figures are the best fit log-normal distribution to the CuP estimates. The best-fit lines

were found using maximum likelihood methods. Figure 7.8 a and b includes times that had cloud thicknesses ranged from near 10 to 300 m, figure 7.9 includes times that had cloud thicknesses ranged from 2000 to 10,000 m. At 1130 and 1430 LST on 6 July 1995, and at 1130 LST on 13 July 1995 the CuP model predicted a bimodal cloud distribution. Both modes are plotted for 1430 LST on 6 July 1995 and 1130 LST on 13 July 1995, at 1130 LST on 6 July 1995 the second mode consists of only a few points so no curve was fit. The accumulated frequency of each mode was allowed to range from 0 to 100%.

On most of the days the CuP model predicted a distribution of clouds that are nearly log-normal over part of the range of cloud thicknesses. The lowest cloud thicknesses are to the right of the best fit line in almost all of the cases plotted in figure 7.8 a and b. The model predicted more low cloud thicknesses than would be observed from a log-normal distribution. The CuP estimates fell below the the best-fit line at larger cloud thicknesses; the model predicted more high tops than would be observed from a log-normal distribution. These results were consistent with Lopez (1977) who found that at larger cloud thicknesses observations tend to drop below the log-normal curve.

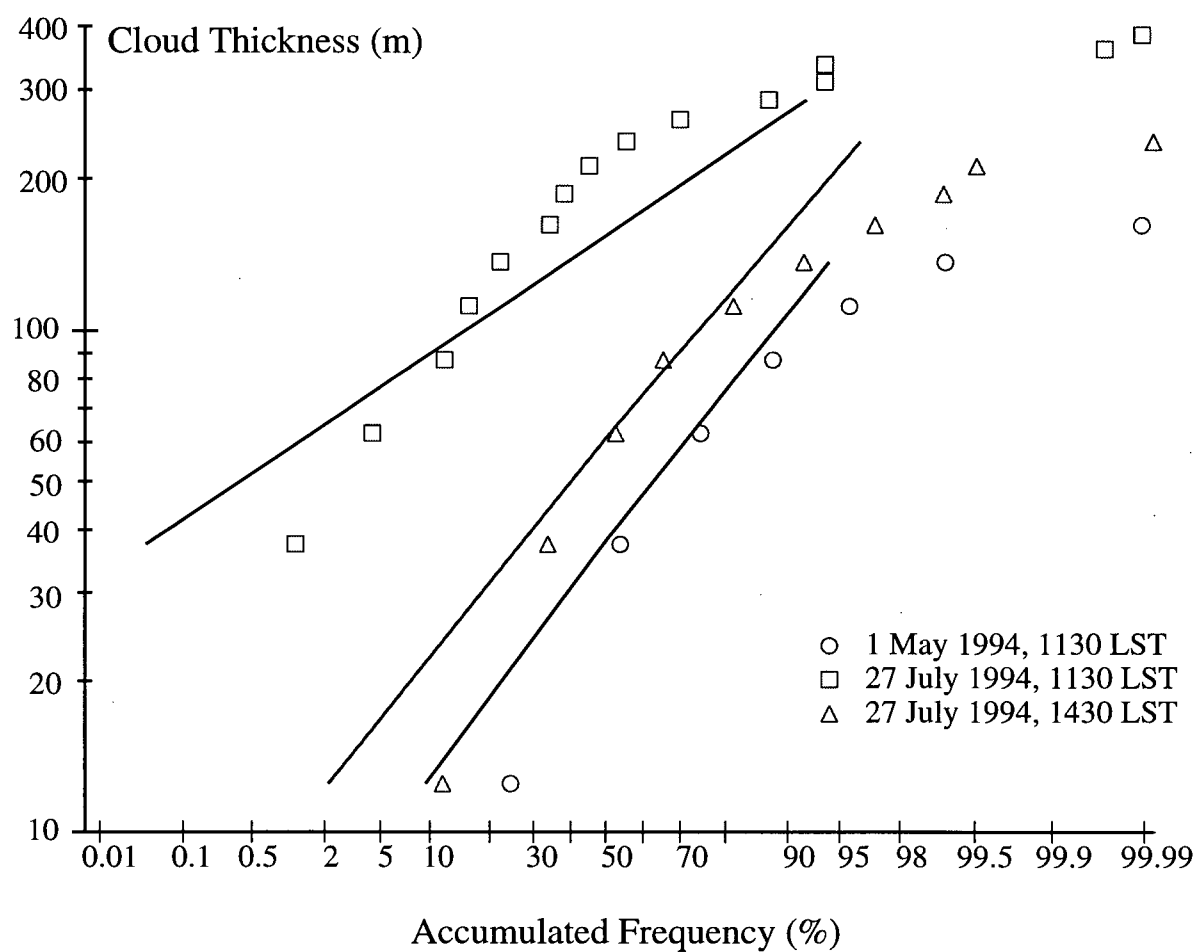


Figure 7.8a. Cloud thickness as predicted by the CuP model. Symbols are the model output. The lines are a best-fit estimate of a log-normal curve to the CuP output.

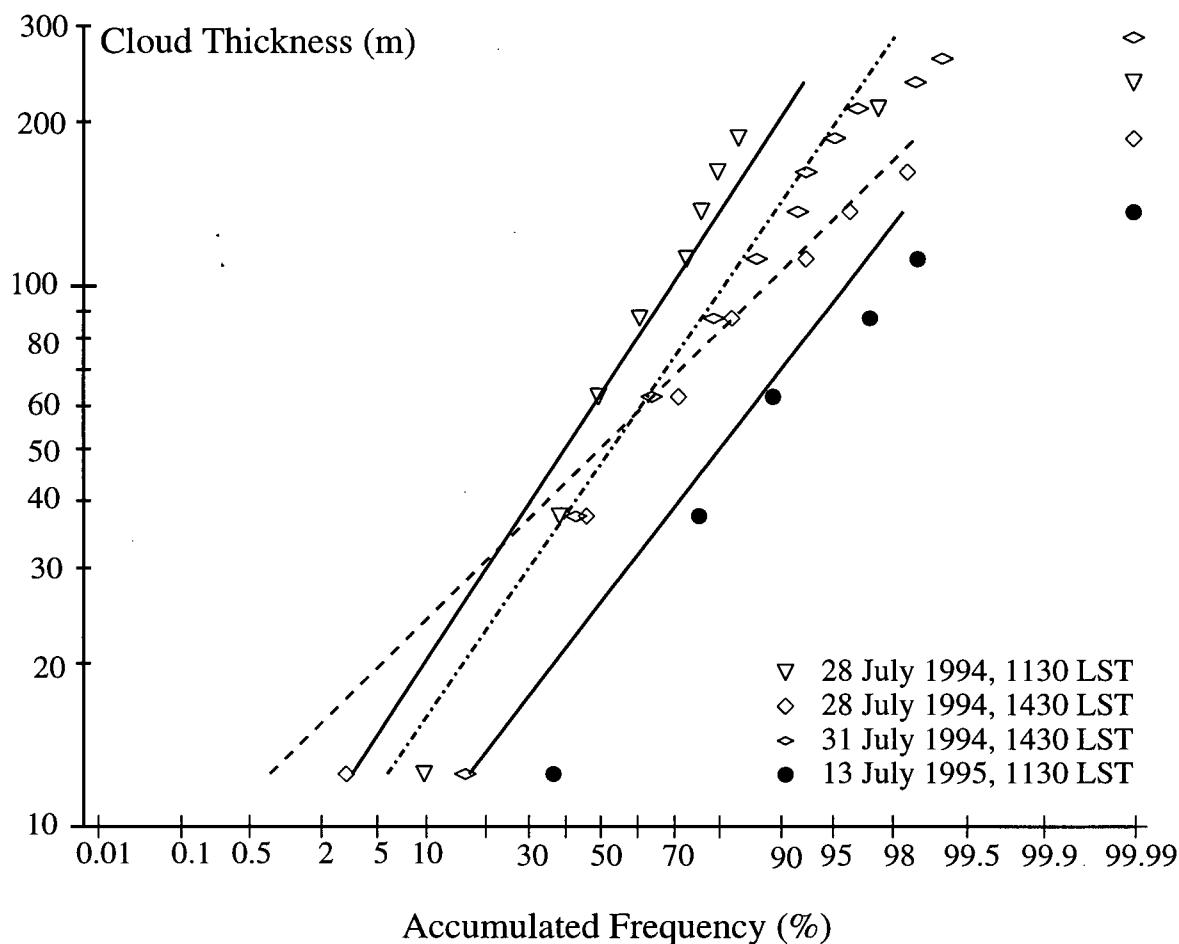


Figure 7.8b. Cloud thickness as predicted by the CuP model. Symbols are the model output. The lines are a best-fit estimate of a log-normal curve to the CuP output. The second mode for 13 July is plotted in figure 7.8. The dot-dashed line is the best-fit curve for 28 July 1994, 1130 LST. The dashed line is the best-fit curve for 28 July 1994, 1430 LST.

On the days with large cloud thickness the CuP model estimates were very close to a log-normal distribution (figure 7.9). At large cloud heights the CuP estimates dropped below the best fit line, consistent with Lopez (1977).

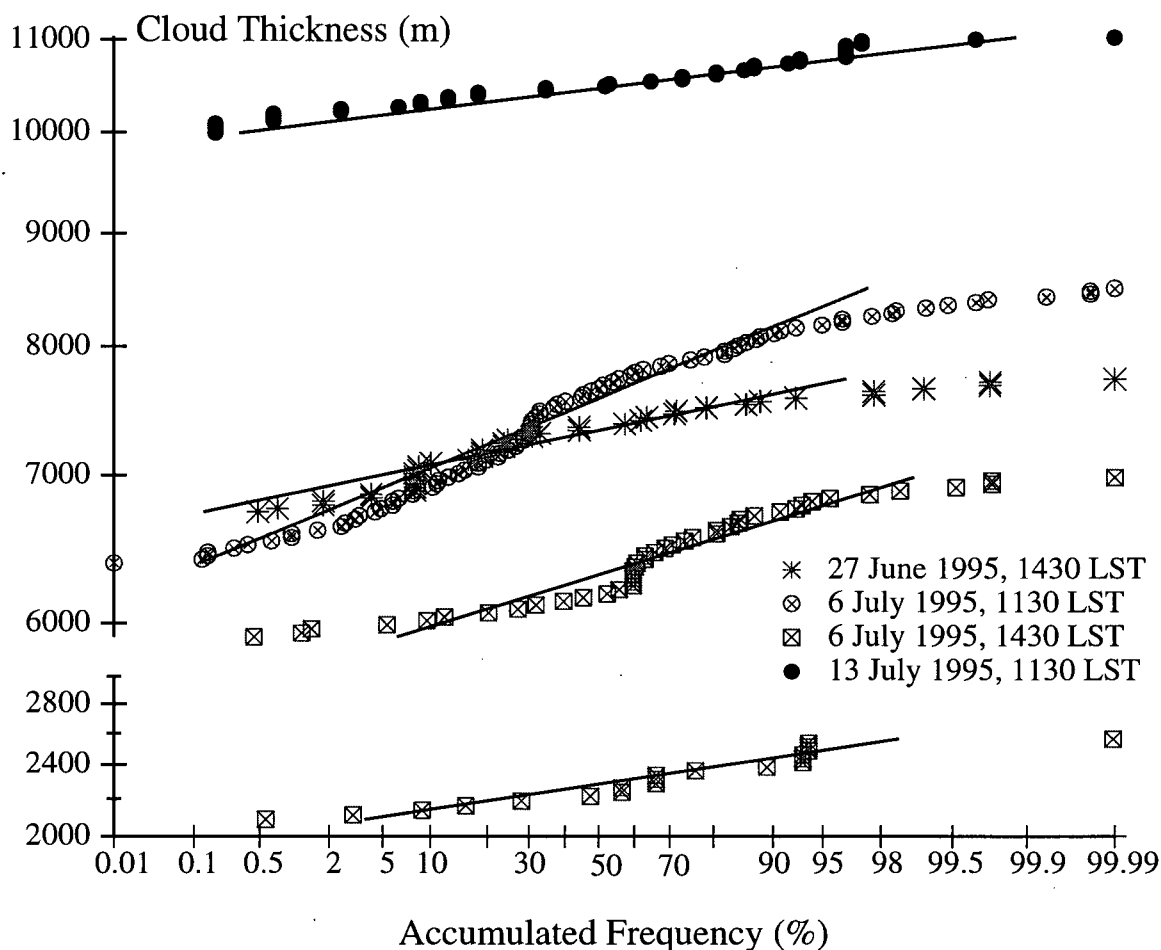


Figure 7.9. Cloud thickness as predicted by the CuP model. Symbols are the model output. The lines are a best-fit estimate of a log-normal curve to the CuP output. On 6 July 1995 the cloud thickness distribution was bimodal. Note the split vertical axis.

The Kolmogorov-Smirnov goodness-of-fit test was used to determine if the log-normal distribution was a good representation of the CuP predictions (Kirkpatrick 1974). Using a level of significance of 0.05, all but one of the CuP distributions were not significantly different from a log-normal distribution. The test compared the maximum difference in the cumulative probability functions. If the difference was larger than a

critical test statistic, than the null hypothesis (that the data is log-normal) is rejected. Table 7.1 lists the critical and calculated statistic used for the Kolmogorov-Smirnov test.

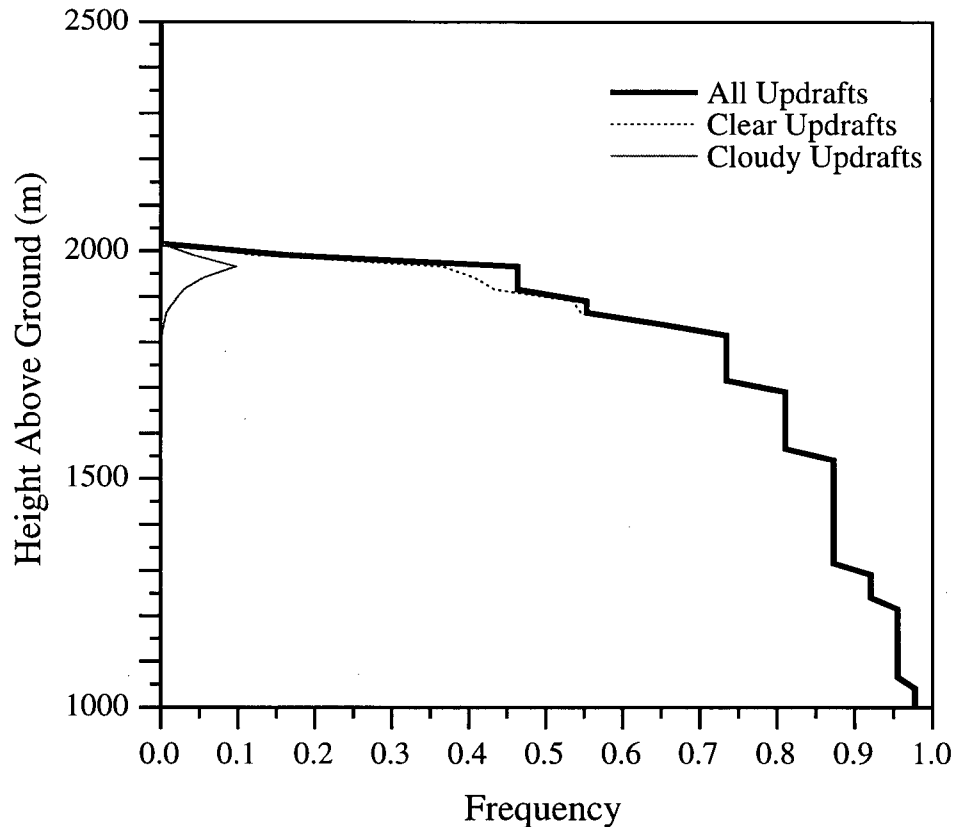
Table 7.1. Calculated and critical statistics for a log-normal fit to the CuP cloud thicknesses. "Lower" after the date and times refers to the smaller cloud thickness at a given time, "upper" after the date and time refers to the larger cloud thickness at a given time.

Date and Time (LST)	Sample Size	Calculated Statistic	Critical Statistic	Accept/Reject Null Hypothesis
1 May 1994, 1130	7	0.25	0.48	Accept
27 July 1994, 1130	16	0.03	0.34	Accept
27 July 1994, 1430	10	0.17	0.41	Accept
28 July 1994, 1130	10	0.03	0.41	Accept
28 July 1994, 1430	8	0.00	0.45	Accept
31 July 1994, 1430	12	0.00	0.37	Accept
27 June 1995, 1430	41	0.15	0.21	Accept
6 July 1995, 1130	86	0.12	0.15	Accept
6 July 1995, 1430 lower	20	0.22	0.29	Accept
6 July 1995, 1430 upper	44	0.27	0.21	Reject
13 July 1995, 1130 lower	6	0.36	0.52	Accept
13 July 1995, 1130 upper	43	0.13	0.25	Accept

7.3.2 Clear and Cloudy Updrafts

The CuP model predicted the frequency of both clear and cloudy up drafts at any level. No observations were made at the ARM site to verify these results. Figure 7.10 shows a plot of all rising thermals from 1430 LST on 28 July 1994 using $\theta_{v,Best}$ and $z_{LCL,Best}$ to center the JFD. This plot is very similar to those made on other days in 1994. The very lowest thermals were all cloud free. Cloudy thermals began to form near 1850 m and increased in number with height. The number of cloudy updrafts increased with height to some level. In general the number of clear thermals steadily decreases with height until

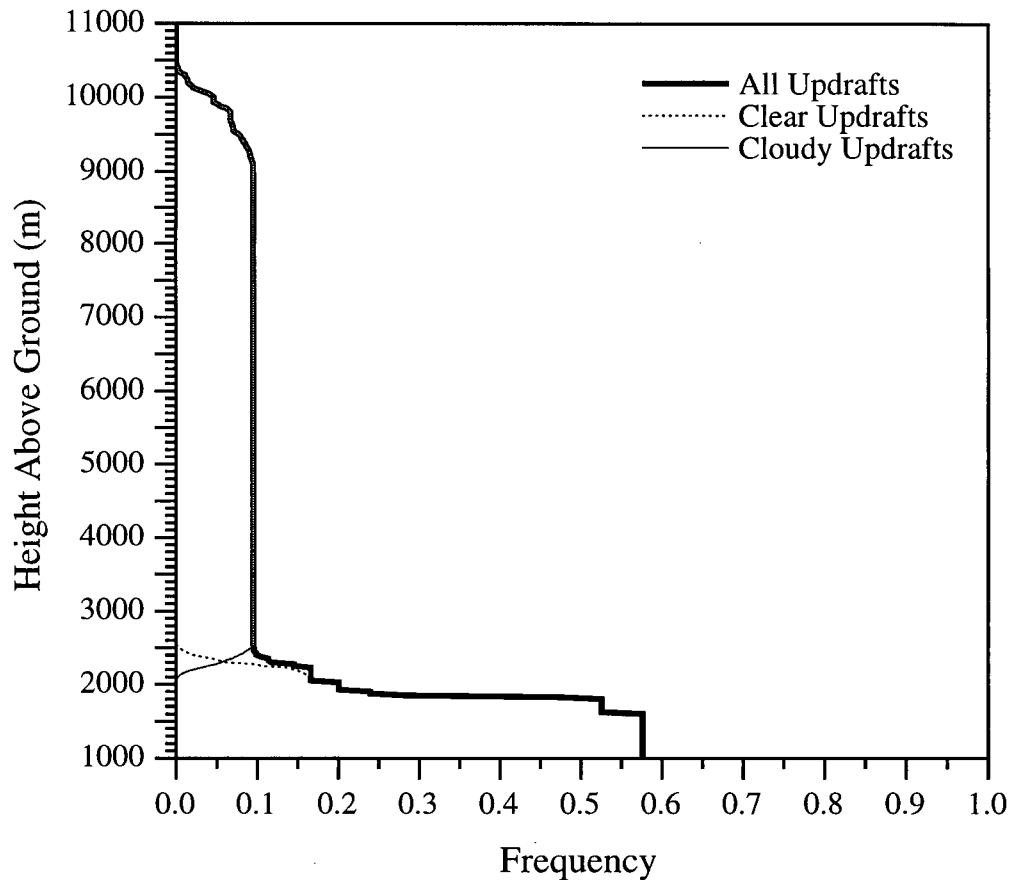
all thermals are cloudy. This plot shows many of the features that were discussed in section 6.5. The large step near 2000 m is caused by clear parcels reaching z_i . In this case the inversion is strong enough that the cloudy parcels were not able to rise higher than the clear updrafts.



7.10. CuP modeled up drafts for 28 July 1994, 1430 LST using surface layer means. All updrafts below 1000 m were clear. “All rise” is the sum of clear and cloud parcel at any given height.

The CuP predicted updrafts are quite different for the 1995 case study days (figure 7.11). The plot shows many of the features that were discussed in section 6.5. The lower step was caused by clear parcels reaching z_i . Cloudy parcels were able to rise to 9000 m

before they begin to reach the θ_v profile. An explanation of the deep clouds is in section 7.3.1.



7.11. CuP modeled up drafts for 6 July 1995, 1430 LST using surface-layer means. All updrafts below 1000 m were clear. “All rise” is the sum of clear and cloud parcels at any given height.

7.3.3 Cloud-Base Height

As described in section 4, cloud-base height was measured by the Belfort Laser Ceilometer (BLC) and the Micropulse Lidar (MPL) at the Central Facility. The mean cloud base for the study period reported by the BLC was 2169.9 m, the standard deviation reported was 580 m. The mean cloud base for all of the study days reported by the MLP was 2039.6 m, the standard deviation reported was 744 m. Using a t-test the difference

between these means was not statistically significant at the 0.05 level of significance. But the P-value obtained (0.069) was close to the level of significance, indicating that the t-test results were weak. A test was also done comparing the variances. They were found to be different at the 0.05 level of significance (P-value of 0.001). The P-value is the probability that the sample outcome could have been more extreme than the observed one, given that the null hypothesis (such as equal means or variances) is true. Large (greater than the level of significance) P-values support the null hypothesis, while small (smaller than the level of significance) refute the null hypothesis. A P-value that is close to the level of significance indicates that the evidence is not as strong as would be obtained from a simple accept/reject test.

Tests were made comparing the mean cloud-base height and variance computed from the CuP model using the JFD centered at three different locations: $\theta_{v,sfc}$ and $z_{LCL,sfc}$, $\overline{\theta_{v,ML}}$ and $\overline{z_{LCL,ML}}$, and $\theta_{v,Best}$ and $z_{LCL,Best}$. When using $\theta_{v,sfc}$ and $z_{LCL,sfc}$, the CuP model gave the lowest cloud-base heights (table 7.2). Using $\overline{\theta_{v,ML}}$ and $\overline{z_{LCL,ML}}$ the CuP model gave the highest cloud-base heights. The $\theta_{v,Best}$ and $z_{LCL,Best}$ gave a result between the mixed layer and surface layer values.

Table 7.2. Mean and variance of cloud base height observed at the CF with the BLC and MLP. The CuP estimates were made using the JFD set to the mean mixed layer, surface layer, and best estimate values of z_{LCL} and θ_v . See text for details.

	MPL	BLC	Mixed Layer	Surface Layer	Best Fit
Mean (m)	2039.6	2169.9	1680.5	2269.8	1946.6
Variance (m ²)	552911.4	337500.3	231560.2	158735.2	342986.2

The CuP model estimated mean cloud base, using a JFD centered at $\overline{\theta_{v,ML}}$ and $\overline{z_{LCL,ML}}$ was greater than the MPL, but statistically equivalent to the BLC values at the 0.05 level of significance (Table 7.3). However the small P-value between the CuP model and BLC indicates that the evidence was weak. The CuP model estimated mean cloud base using a JFD centered at the $\theta_{v,sfc}$ and $z_{LCL,sfc}$ was less than the MPL and BLC values at the 0.05 level of significance. With the JFD centered at $\theta_{v,Best}$ and $z_{LCL,Best}$ the CuP cloud base heights were less than the BLC, but equal to the MPL at the 0.05 level of significance (P-values of 0.001 and 0.32, respectively).

Table 7.3. Statistical tests comparing CuP and observed means. Level of significance was chosen to be 0.05. Means are represented by the symbol μ . The null hypothesis is rejected if absolute value of the test statistic is greater than the critical value.

Null Hypothesis	Test Statistic	Critical Value	P-Value	Accept/Reject
$\mu_{BLC} = \mu_{sfc}$	10.407	1.647	<0.001	Reject
$\mu_{BLC} = \mu_{ML}$	-1.570	-1.651	0.059	Accept
$\mu_{BLC} = \mu_{Best}$	3.253	1.650	0.001	Reject
$\mu_{MPL} = \mu_{sfc}$	5.536	1.648	<0.001	Reject
$\mu_{MPL} = \mu_{ML}$	-2.746	-1.653	0.003	Reject
$\mu_{MPL} = \mu_{Best}$	1.004	1.652	0.317	Accept

The estimates of the variance by the CuP model using $\overline{\theta_{v,ML}}$ and $\overline{z_{LCL,ML}}$, and $\theta_{v,sfc}$ and $z_{LCL,sfc}$ to locate the JFD were statistically different than those observed by the BLC and MPL. The variance predicted by the CuP model using $\theta_{v,Best}$ and $z_{LCL,Best}$ to locate the JFD was significantly different than the MPL observed variance, however the variance predicted

by the CuP model using $\theta_{v,Best}$ and $z_{LCL,Best}$ to locate the JFD was not significantly different than the BLC variance at the 0.05 level.

Table 7.4. Statistical tests comparing CuP and observed variances. Level of significance was chosen to be 0.05. Variances are represent by the symbol σ^2 . The null hypothesis is rejected if test statistic is greater than the large critical value or less than the low critical value.

Null Hypothesis	Test Statistic	Low Critical Value	High Critical Value	P-Value	Accept/Reject
$\sigma_{BLC}^2 = \sigma_{sfc}^2$	1.457	0.779	1.283	0.001	Reject
$\sigma_{BLC}^2 = \sigma_{ML}^2$	0.470	0.704	1.421	<0.001	Reject
$\sigma_{BLC}^2 = \sigma_{Best}^2$	1.016	0.718	1.394	0.536	Accept
$\sigma_{MPL}^2 = \sigma_{sfc}^2$	0.419	0.695	1.437	<0.001	Reject
$\sigma_{MPL}^2 = \sigma_{ML}^2$	0.287	0.657	1.523	<0.001	Reject
$\sigma_{MPL}^2 = \sigma_{Best}^2$	0.620	0.664	1.507	0.011	Reject

7.4 Daily Results

The values z_i , mixed layer θ_v ($\overline{\theta_{v,ML}}$), mixed layer z_{LCL} ($\overline{z_{LCL,ML}}$), the slopes of the JFD axes, and standard deviations for the CuP model were determined as described in section 4. Table 7.5 lists values of z_i , $\overline{\theta_{v,ML}}$, and $\overline{z_{LCL,ML}}$, while values of the other JFD parameters are listed in appendix E. Values of the Bowen ratio and solar-forcing slopes, and the standard deviations along each of the axes are consistent with those found by Schrieber et al. (1996).

Table 7.5. Values of z_i , $\overline{\theta_{v,ML}}$, and $\overline{z_{LCL,ML}}$ taken from sondes for all case study days (continued on next page).

Date	Time	z_i (km)	$\overline{\theta_{v,ML}}$ (°C)	$\overline{z_{LCL,ML}}$ (km)
1 May 1994	0838	0.718	8.7	1.142
	1130	0.932	11.5	1.196
	1452	1.057	14.7	1.331
	1730	1.372	16.5	1.635
27 July 1994	0830	0.138	22.1	1.118
	1130	2.372	26.0	2.002
	1430	2.499	27.1	2.221
	1730	2.321	28.6	2.407
28 July 1994	0830	0.234	23.8	1.004
	1135	0.820	27.5	1.604
	1430	1.981	28.7	2.060
	1730	1.937	29.4	2.269
31 July 1994	0830	0.509	27.3	1.050
	1130	0.752	32.6	1.700
	1430	2.030	35.1	2.302
	1730	2.434	35.5	2.380

Table 7.1 continued. Values of z_i , $\overline{\theta_{v,ML}}$, and $z_{LCL,ML}$ taken from sondes for all case study days

Date	Time	z_i (km)	$\overline{\theta_{v,ML}}$ ($^{\circ}\text{C}$)	$z_{LCL,ML}$ (km)
27 June 1995	0830	0.229	29.6	1.428
	0910	0.470	30.8	1.721
	1128	1.753	32.9	2.183
	1429	2.081	34.6	2.130
6 July 1995	0829	0.177	31.3	1.559
	1128	1.833	35.5	2.185
	1431	3.083	37.7	2.730
9 July 1995	0830	0.309	24.0	1.443
	1130	0.705	38.0	2.239
	1431	1.079	39.4	2.390
11 July 1995	0830	0.357	34.7	1.619
	1130	0.671	41.7	2.869
	1430	2.932	43.8	3.394
13 July 1995	0830	0.405	35.3	1.307
	1131	1.855	38.8	2.008
	1430	2.314	40.0	2.190

7.4.1 Date: 1 May 1994

Profiles of θ_v from 1 May are shown in figure 7.12. At 1130 LST z_i was about 0.95 km. The 1130 LST θ_v profile was nearly moist adiabatic from 1.3 to 1.6 km. But this layer was above z_i , indicating the observed cloud layer may not be turbulently coupled to the mixed layer. At 1130 and 1452 the mixing ratio (r) (figure 7.13) was almost constant to 1.0 km. At 1730 LST, r decreased slowly with height to an altitude of about 1

km where r began to decrease more quickly with height. There was no jump in r to indicate z_i as there was in the earlier profiles.

A plot of z_{LCL} with height (figure 7.14) showed a well-mixed layer below 1.0 km at 1130 LST. There was a jump in z_{LCL} near 0.90 km at z_i . The layer from 0.7 to 1.0 km could be the Betts (1982) transition layer. There was a cloud layer from 1.0 to 1.7 km. This implied the cloud layer was only weakly linked to the well mixed layer, as shown by the mixing line structure on the z_{LCL} profile. Betts (1985) found that there was often a layer between the well mixed layer and the cloud layer that had a z_{LCL} gradient different than that of the cloud layer. The z_{LCL} gradient in the well mixed layer should be zero. More examples of the transition layer are shown for some of the later case study days. The z_{LCL} measured by the sonde never reached the height reported by the sonde, because the sonde did not rise through a cloud.

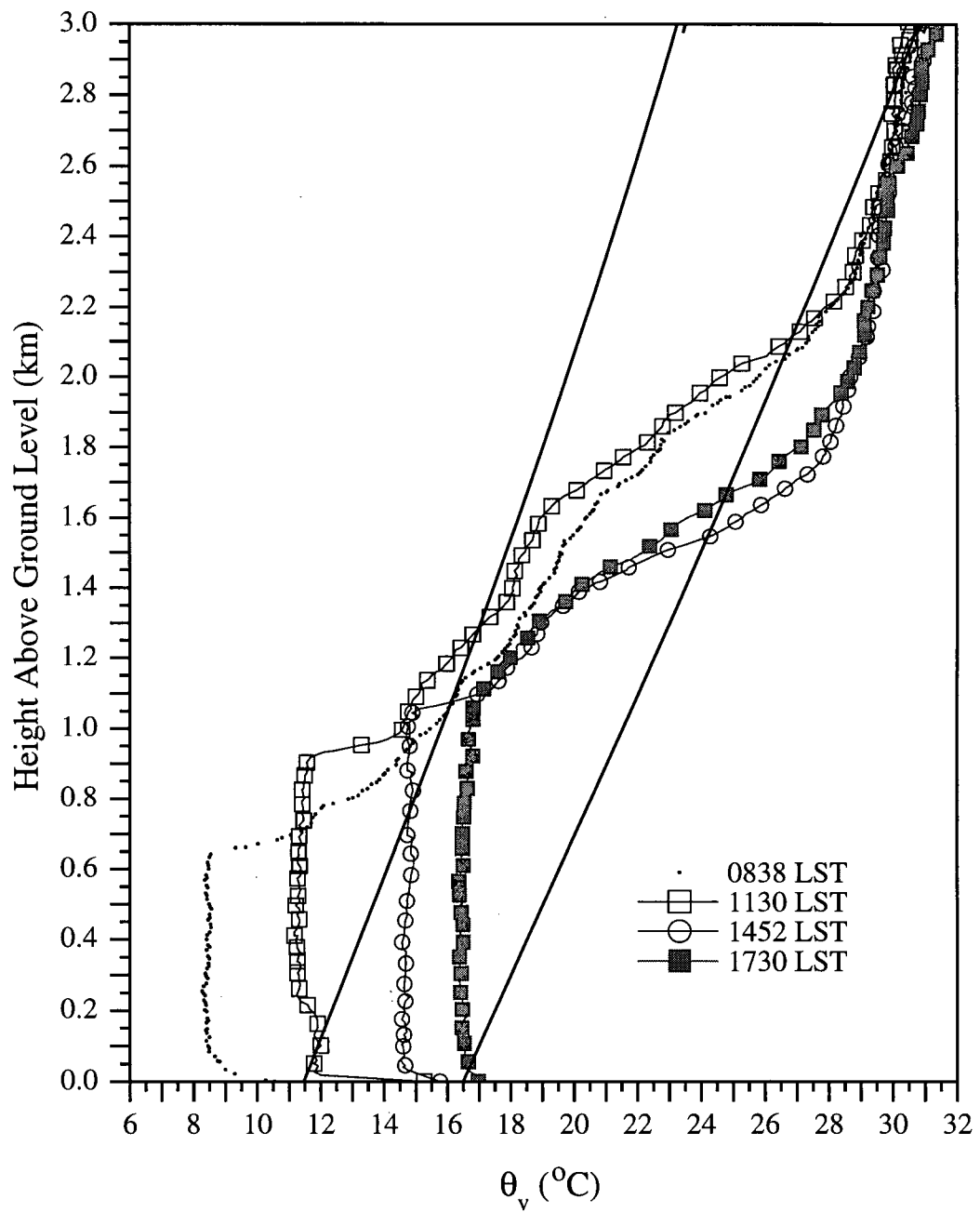


Figure 7.12. Profiles of θ_v taken from CF sondes on 1 May 1994. Solid lines are moist adiabats.

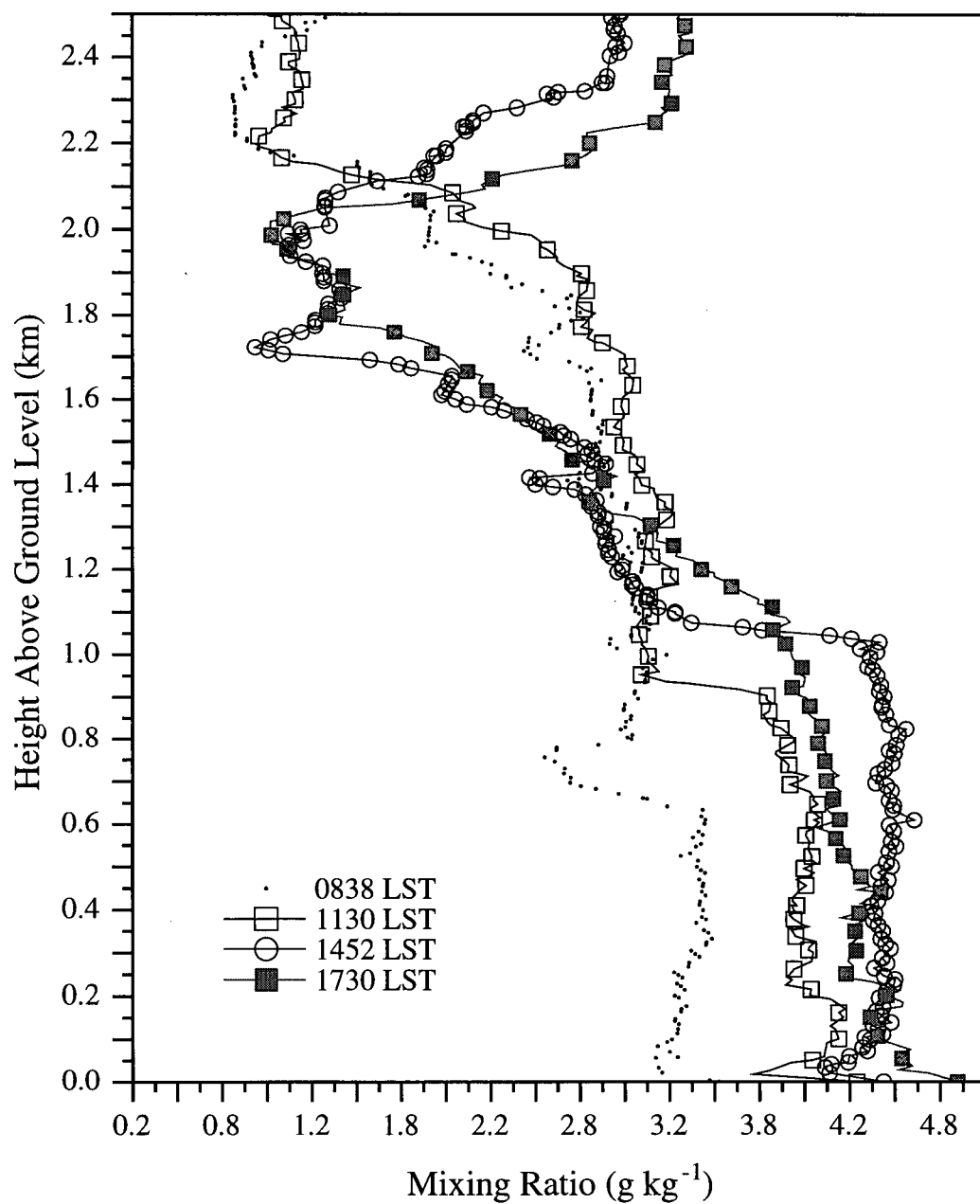


Figure 7.13. Profiles of r taken from CF sondes on 1 May 1994

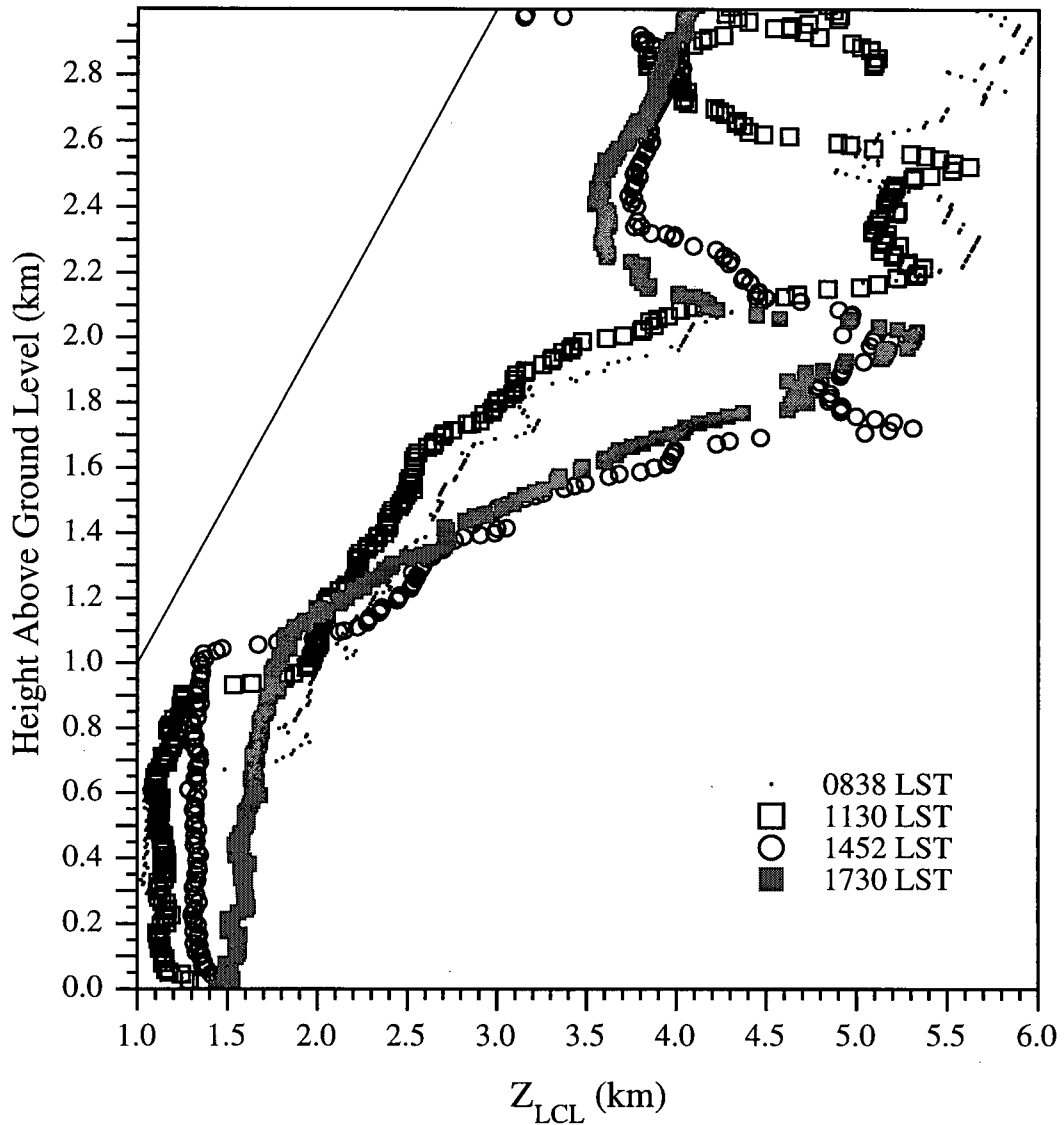


Figure 7.14. Profiles z_{LCL} taken from CF sondes on 1 May 1994. Thin solid line is z equal to z_{LCL} . Cloudy air is above the line, clear air below.

Figure 7.15 shows both observed and CuP modeled cloud cover. The observed cloud cover at 1130 LST may not have been due to local boundary-layer processes, because of the weak turbulent coupling between the mixed and cloud layers. Perhaps the clouds were advected from a neighboring region. Model results for 1 May were typical. With the mean of the JFD set to the $\theta_{v,ML}$ and $z_{LCL,ML}$ the CuP model underestimated the

cloud cover. Using a JFD with its mean set $\theta_{v,sfc}$ and $z_{LCL,sfc}$ the model greatly overestimated the cloud cover. One exception occurred on 1 May. At 1200 LST the human observer at the CF reported 80% cloud cover. At that time both the MPL and the BLC did not report any cloud-base heights. It was unlikely that there are so many clouds over the CF with no reported cloud bases, the human probably over estimated the cumulus-cloud cover at 1200 LST. Some high clouds were observed at 1600 and 1700 LST, but have not been included in figure 7.7. The time interval between the CuP calculations was caused by the BBSS launch times.

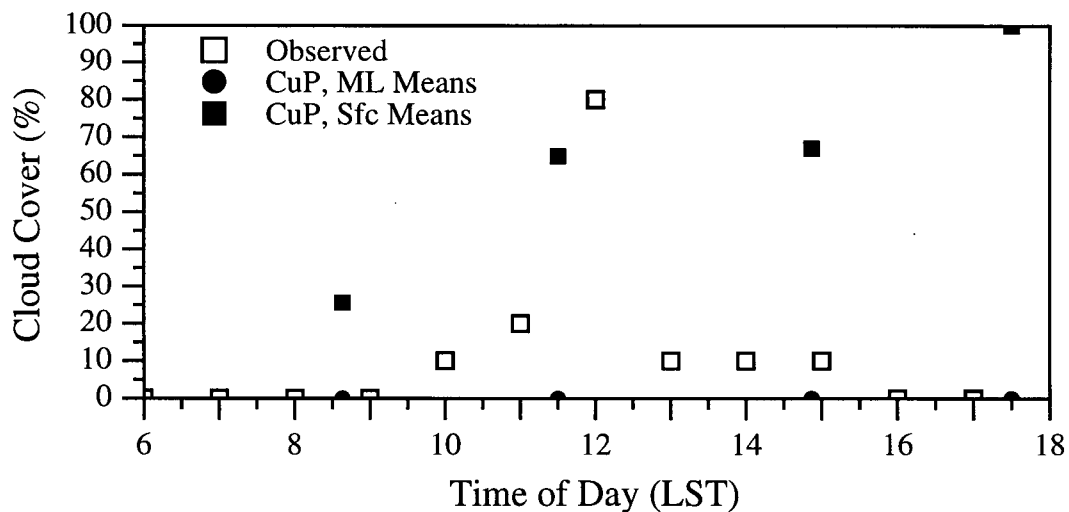


Figure 7.15. Observed and CuP modeled cloud cover on 1 May 1994. CuP cloud cover was determine using a JFD set to the both the mixed layer (ML) and surface-layer (Sfc) means. Cloud amounts that were above the convective boundary layer have been removed (see text for details).

Values and ranges of cloud base heights predicted by the CuP model were consistent with observations (figure 7.16). The mean cloud-base height from the CuP model, using a JFD centered at $\theta_{v,sfc}$ and $z_{LCL,sfc}$ were smaller than the observed sample mean cloud-base height from the BLC and larger than the sample mean from the MPL.

Statistical t-tests were used to determine if the mean cloud-base height predicted by the CuP model was the same as the inferred population mean from the BLC and MPL. Differences between the CuP cloud-base heights, and the MPL and BLC cloud base heights were statistically significant at a 0.05 level (P-values 0.0089 and 0.019, respectively) indicating that the CuP mean was probably between the BLC and MPL means. The BLC and MPL did not report any clouds later in the day, although clouds were reported by the human observer. The CuP model did predict cloud coverage later in the day when using $\theta_{v,sfc}$ and $z_{LCL,sfc}$ to center the JFD.

The variance predicted by the CuP model was less than the sample variance measured by the BLC. All MPL observed cloud-base heights were at same level so no variance could be determined. Tests were made to determine if the CuP and BLC variances were the same. The model overestimated the variance of cloud-base heights compared to the BLC (P-value of <0.0001).

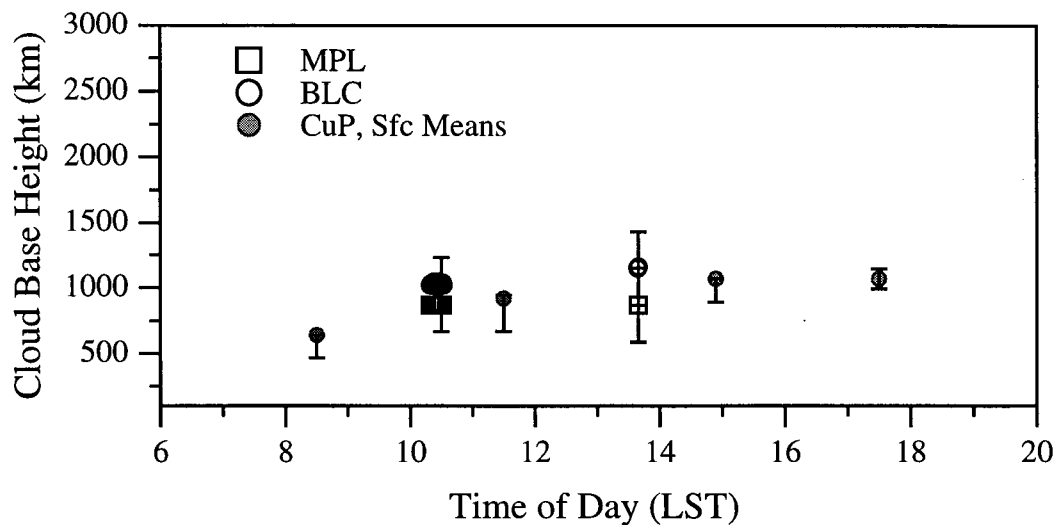


Figure 7.16. Observed and CuP model predicted cloud base heights for 1 May 1994. CuP points are the predicted mode cloud-base height. Error bars on the CuP points correspond to range of cloud base heights predicted by the model. Error bars on the MPL and BLC correspond to the difference between the observations.

7.4.2 Date: 27 July 1994

The θ_v profiles for the CF sondes are plotted in figure 7.17. The mixed layer reached a steady-state depth by 1130 LST. The capping inversion at the top of the mixed layer remained strong throughout the day. The value of z_i decreased from 2.5 km at 1430 LST to 2.3 km at 1730 LST, probably due to advection and/or subsidence. The layer from 2.4 to 2.7 km was nearly moist adiabatic at 1430 LST, while the layer from 2.1 to 2.5 km was nearly moist adiabatic at 1730 LST.

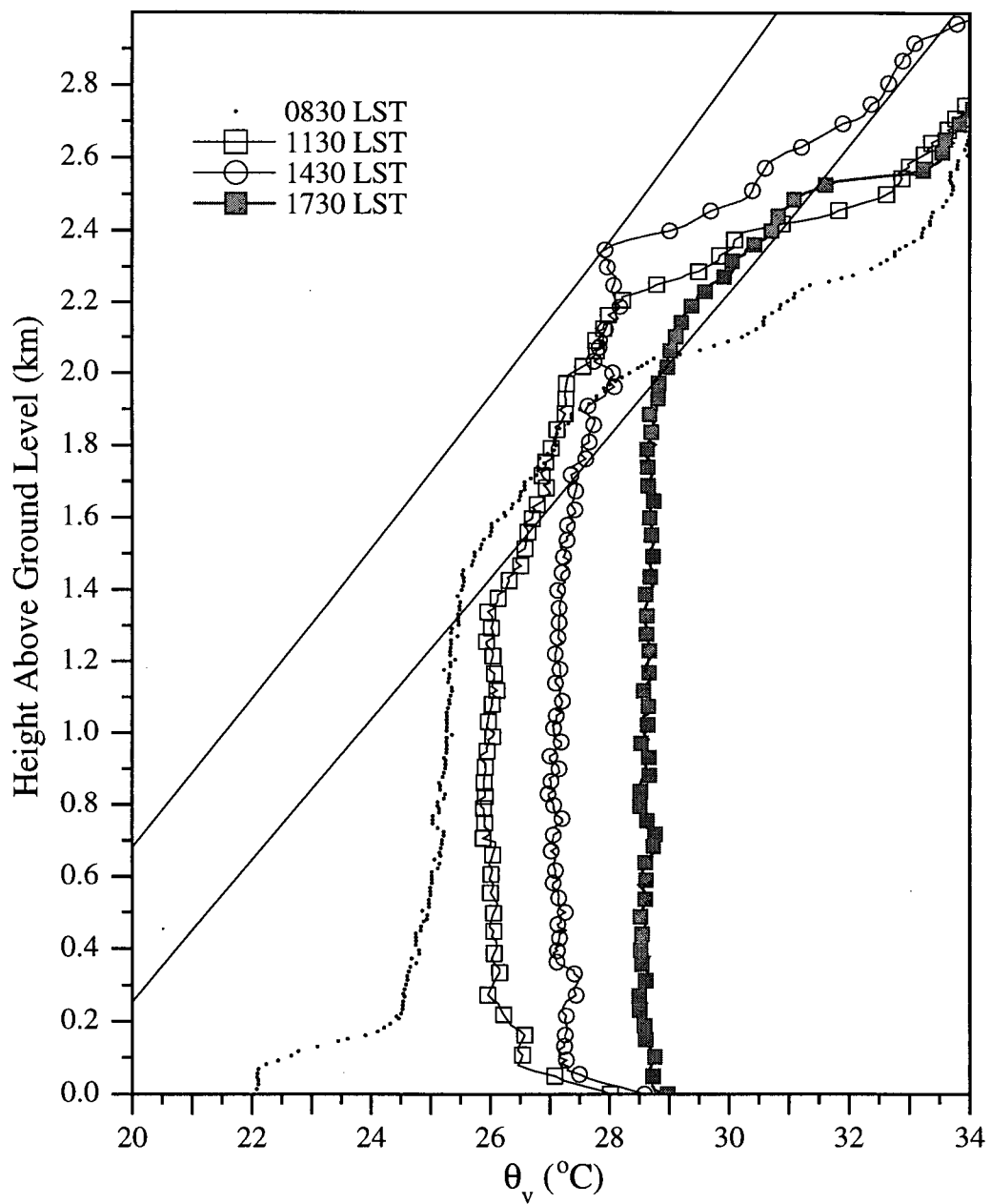


Figure 7.17. Profiles of θ_v taken from CF sondes on 27 July 1994. Solid lines are moist adiabats.

Observed and modeled cloud cover is presented in figure 7.18. Again, using a JFD with means set to $\theta_{v,ML}$ and $z_{LCL,ML}$ the CuP model predicted no cloud cover at most times. At 830 LST the model did predict a very slight amount of coverage. This was caused by an

unusually large JFD. Using $\theta_{v,sfc}$ and $z_{LCL,sfc}$ the model greatly overestimated the cloud cover, with predicted cover values reaching 100%.

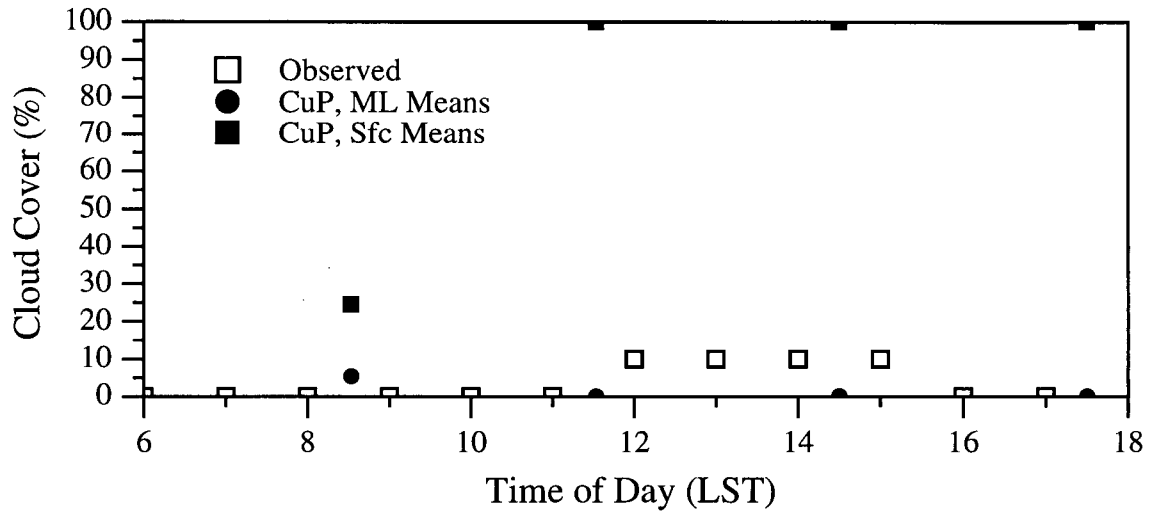


Figure 7.18. Observed and CuP model predicted cloud cover on 27 July 1994. CuP cloud cover was determine using a JFD set to the both the mixed layer (ML) and surface-layer (Sfc) means.

Using $\theta_{v,sfc}$ and $z_{LCL,sfc}$ to center the JFD, the CuP model mode cloud-base height was less than the cloud-base heights observed by the BLC (figure 7.19). At 830 LST the $z_{LCL,sfc}$ was also quite low and the CuP prediction for the mode cloud-base height was very close to the ground, although no fog was reported. Tests were made to determine if the mean from the CuP model and the population mean of the observations were the same. The difference in the means was significant at a 0.05 level (P-value <0.0001). The CuP model, using $\overline{\theta_{v,ML}}$ and $\overline{z_{LCL,ML}}$ also had a smaller mean daily averaged cloud base. The difference between the CuP mean and the BLC population mean was significant at the 0.05 level (P-value <0.001).

The variance predicted by the CuP model using both $\theta_{v,sfc}$ and $z_{LCL,sfc}$, and $\overline{\theta_{v,ML}}$ and $\overline{z_{LCL,ML}}$ was larger than the sample variance measured by the BLC. The CuP variance was larger than BLC population variance at the 0.05 level (P-value <0.001).

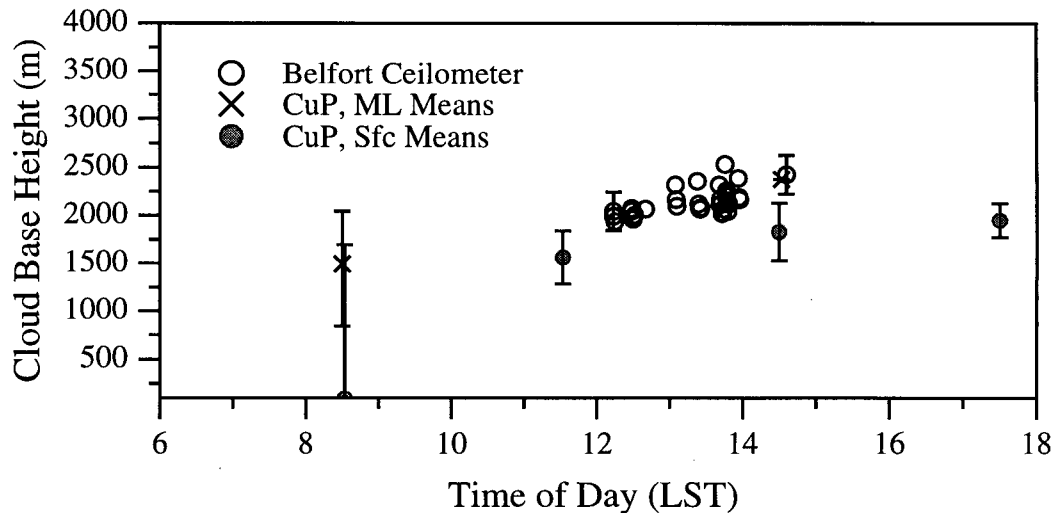


Figure 7.19. Observed and CuP model predicted cloud base height for 27 July 1994. CuP points are the predicted mode cloud-base height. Error bars correspond to range of cloud base heights predicted by the model. The MPL was inoperative. Note that the time axis does not cross the cloud base axis at 0.

7.4.3 28 July 1994

Profiles of θ_v for 28 July are plotted in figure 7.20. By 1135 LST there was only a small inversion between the well-mixed and the residual layers near 0.8 km. The mixed layer reached steady state between 1130 and 1430 LST. At 1730 LST θ_v began to increase some with height above 1 km. At 1730 the z_{LCL} profile also began to increase slowly with height above the same level (figure 7.21). These changes could show that the layer was not completely well mixed or that there was a sampling problem with the sonde. Perhaps it drifted into a region of warm and dry entrained free-atmosphere air. The layer from 1.6 to

2 km at 1730 LST was the Betts transition layer, it was turbulently coupled to the well mixed layer and the cloud layer.

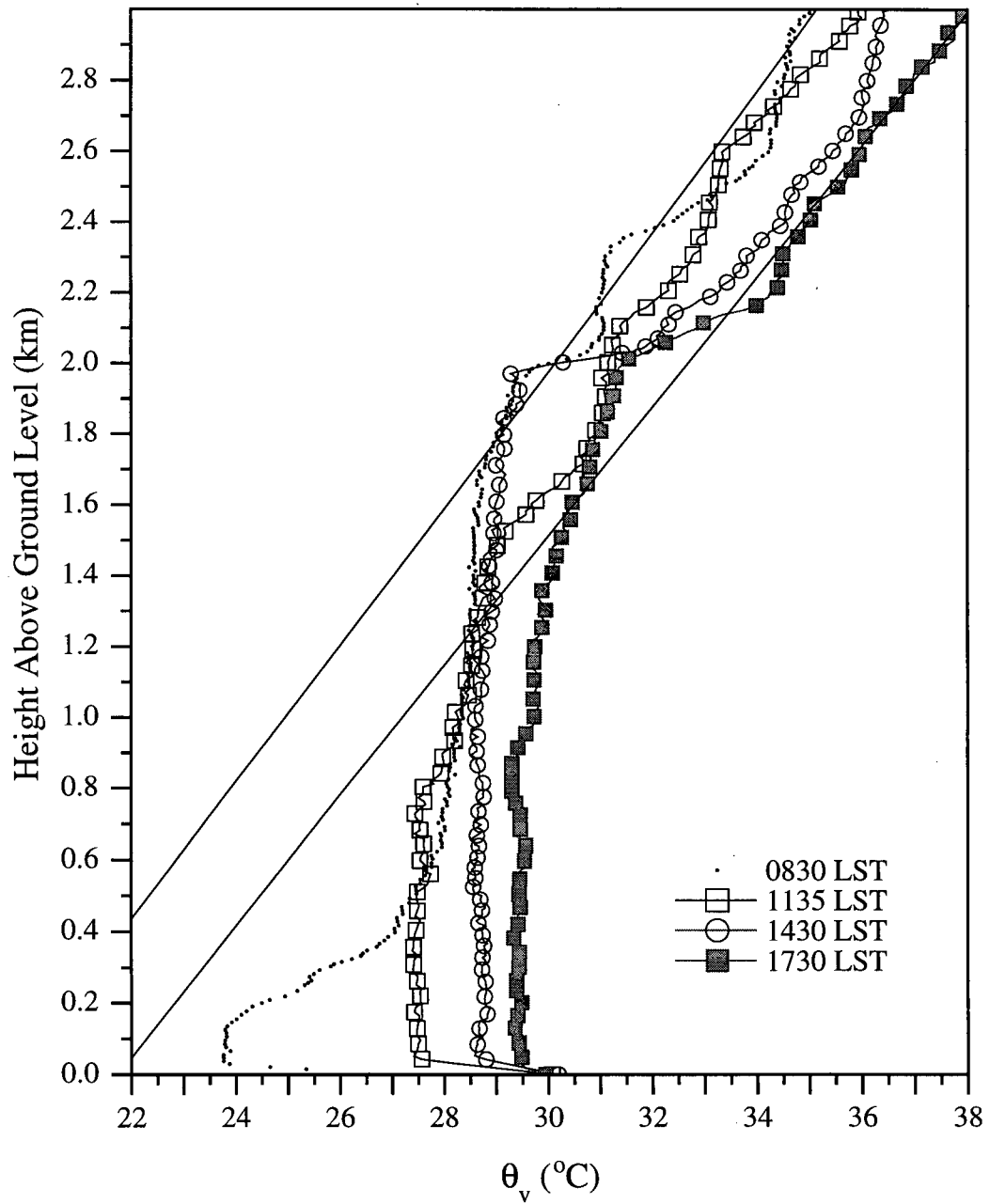


Figure 7.20. Profiles of θ_v taken from CF sondes on 28 July 1994. Solid lines are moist adiabats

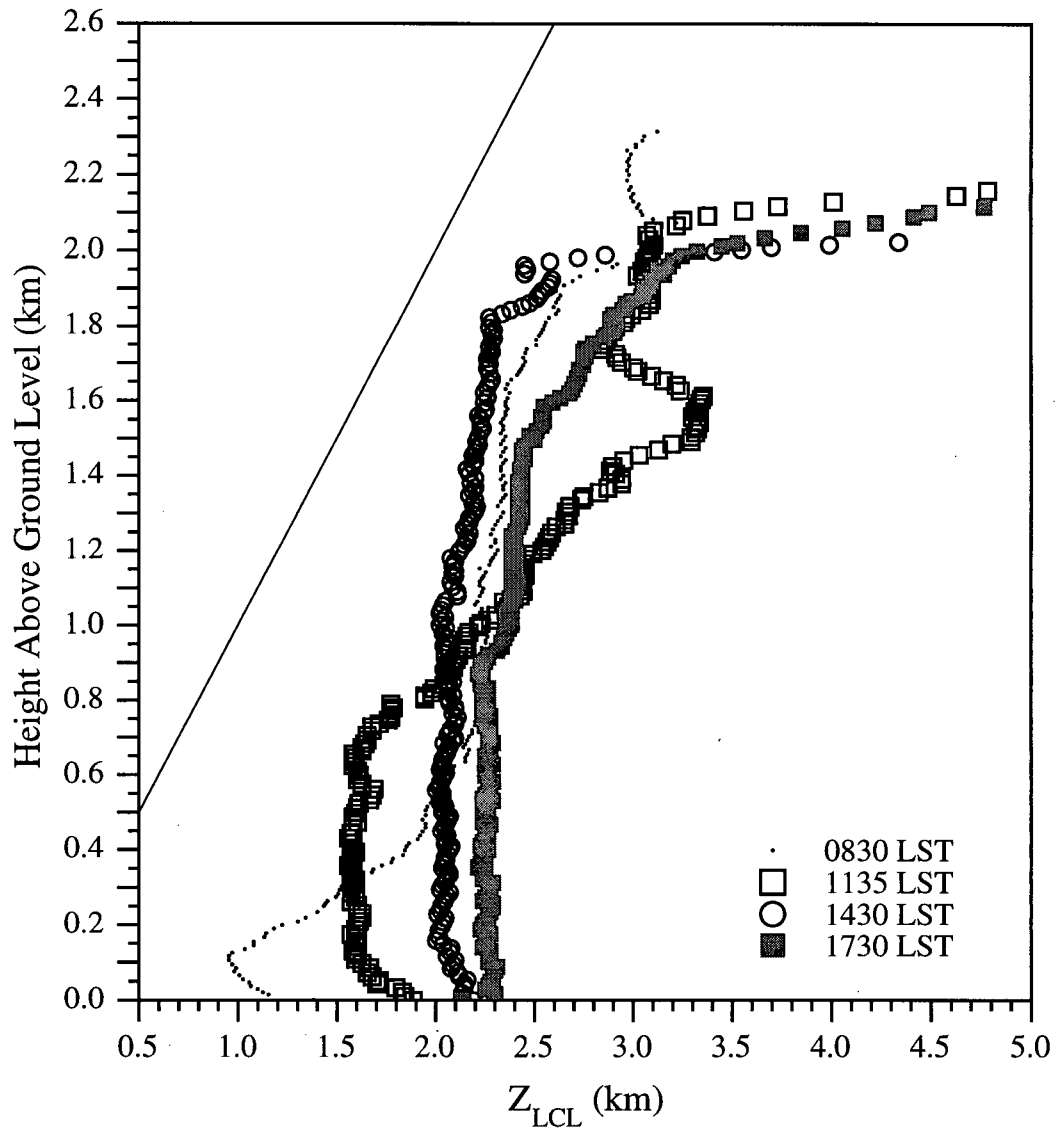


Figure 7.21. Profiles of z_{LCL} taken from CF sondes on 28 July 1994. Thin solid line is z equal to z_{LCL} . Cloudy air is above the line, clear air below.

The observed and modeled cloud cover is shown in figure 7.22. Using $\theta_{v,ML}$ and $z_{LCL,ML}$ the model predicted 0% coverage at all times. Using $\theta_{v,sfc}$ and $z_{LCL,sfc}$ the model over predicted the cloud coverage by 90% through much of the day. Some high clouds were reported at 1700 LST but have not been included in figure 7.23.

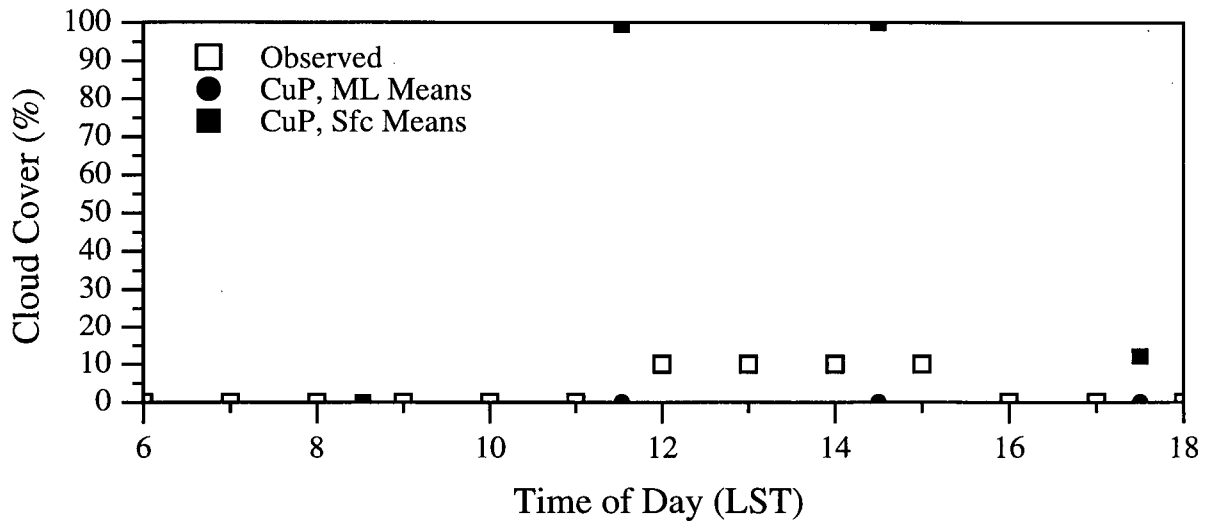


Figure 7.22. Observed and CuP model predicted cloud cover on 28 July 1994. CuP cloud cover was determined using a JFD set to the both the mixed layer (ML) and surface-layer (Sfc) means. Cloud amounts that were above the convective boundary layer have been removed (see text for details).

Using a JFD set to $\theta_{v,sfc}$ and $z_{LCL,sfc}$ the CuP model mean cloud-base height was smaller than those measured by the MPL and BLC. A t-test was used to determine if the CuP mean was the same as the inferred population mean of the observations at the 0.05 level of significance. The tests found that the means were different (P-values were both <0.0001). Although the CuP means were smaller, the mode cloud-base height predicted was within the margin of error of the BLC and the MPL (figure 7.23).

The CuP variance was larger than the BLC and MPL sample variances. Tests showed that the CuP variance and the inferred population variances from the BLC were different at the 0.05 level of significance (P-value <0.0001), but no statistical difference could be determined between the CuP and MPL observations (P-value of 0.859). The instantaneous range of cloud-base height reported by the CuP model appears to be larger than the range reported by the BLC and MPL.

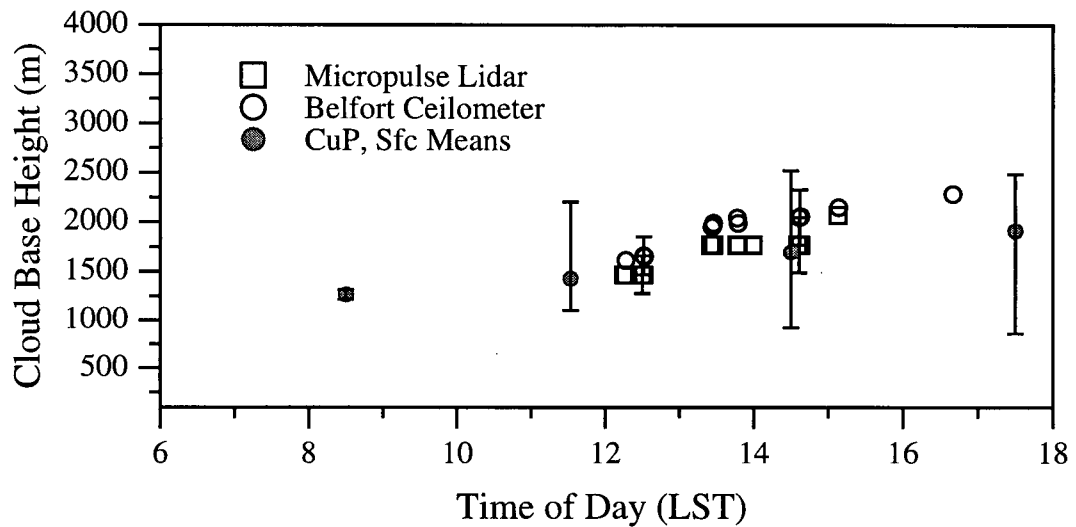


Figure 7.23. Observed and CuP model predicted cloud-base height for 28 July 1994. CuP points are the predicted mode cloud-base height. Error bars correspond to range of cloud base heights predicted by the model.

7.4.4 Date: 31 July 1994

Profiles of θ_v from the CF sonde are shown in figure 7.24. The mixed layer reached steady state between 1130 and 1430 LST. The θ_v profile above the mixed layer remained almost unchanged throughout the day, indicating that advection and subsidence are not important. The θ_v increases with height from 1.2 to 2.2 km in the 1430 LST profile. The Betts transition layer was evident below cloud base in the 1430 and 1730 LST sondes from 1 to 2 km (figure 7.25). Below the transition layer and at 1130 LST the bottom layer was well mixed.

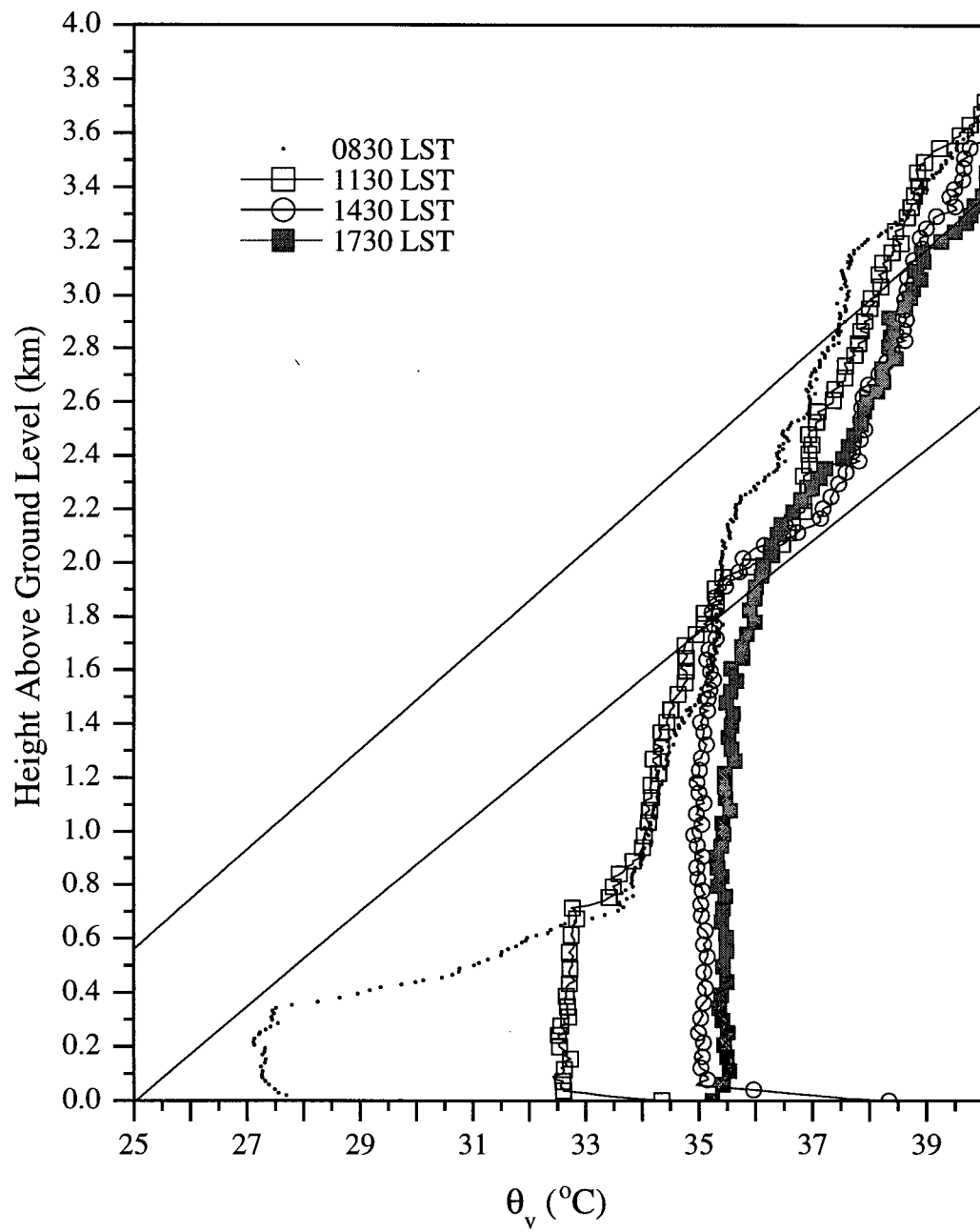


Figure 7.24. Profiles of θ_v taken from CF sondes on 31 July 1994.

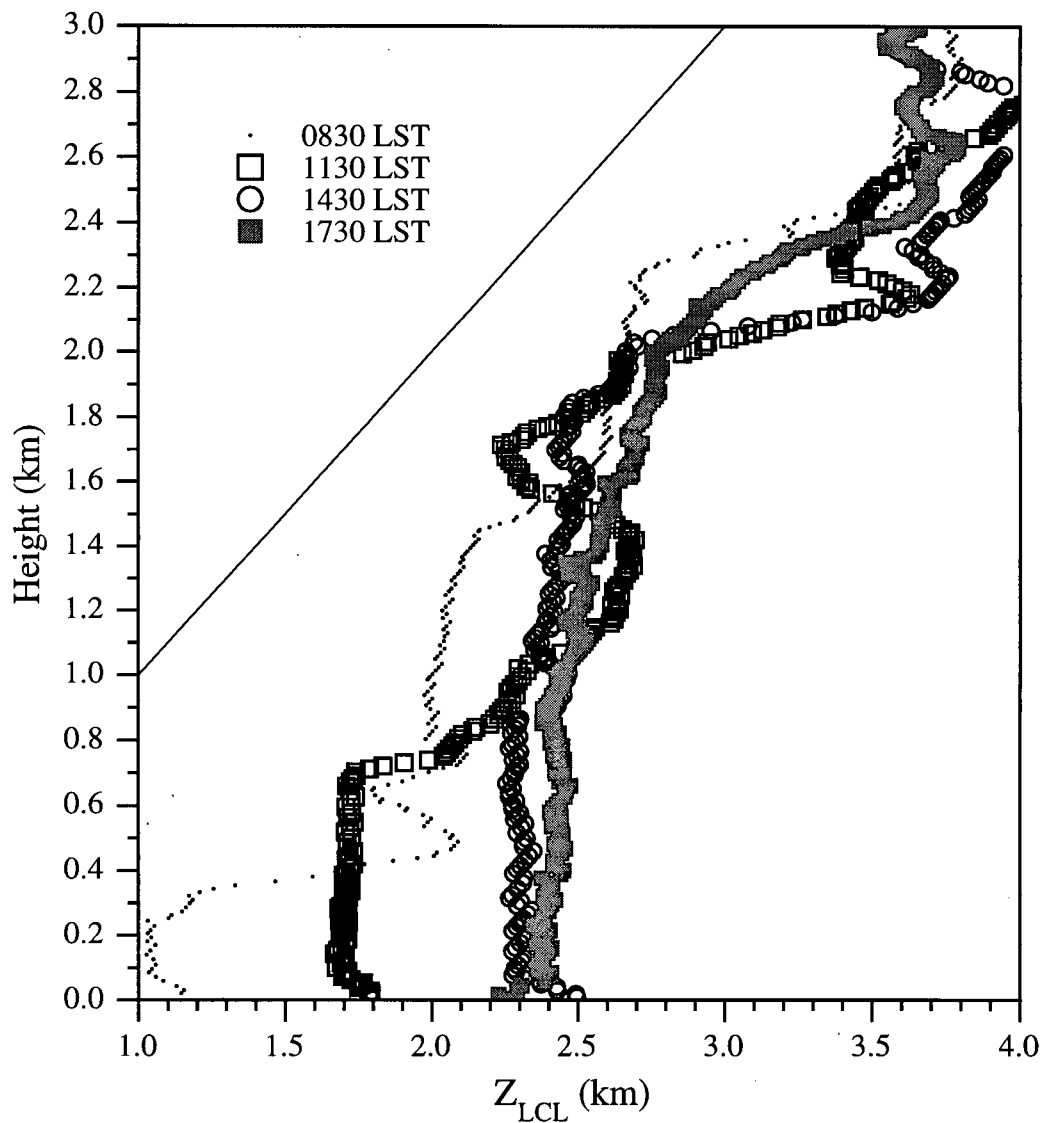


Figure 7.25. Profiles of z_{LCL} taken from CF sondes on 31 July 1994. Thin solid line is z equal to z_{LCL} . Cloudy air is above the line, clear air below.

Observed and modeled cloud cover is presented in figure 7.26. Some cirrus and cirrocumulus were reported at 0600 LST. These cloud amounts were not included in figure 7.18 because they are well above the boundary layer. Observed cloud cover peaked at 1718 because they are well above the boundary layer. Observed cloud cover peaked at 1400 with an onset time of 1300 LST. At 1600 LST a mixture of stratocumulus and cumulus were reported. With $\theta_{v,ML}$ and $z_{LCL,ML}$ the CuP model predicts 0% cloud

coverage at each time. Using the surface-layer means the model predicted 0% at 830 LST.

At the other times the model over predicted cloud cover, but seemed to capture the trend.

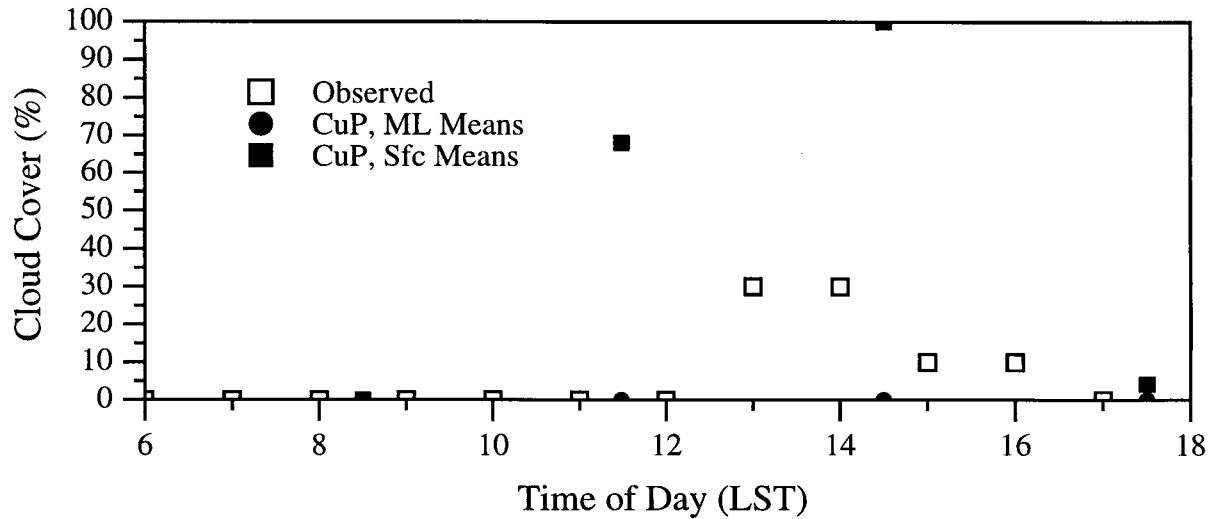


Figure 7.26. Observed and CuP model predicted cloud cover on 31 July 1994. CuP cloud cover was determine using a JFD set to the both the mixed layer (ML) and surface layer (Sfc) means. Cloud amounts that were above the convective boundary layer have been removed (see text for details).

At 0830 LST both the MPL and BLC reported clouds well above the boundary layer (figure 7.27). MPL data was missing through much of the afternoon. The CuP model daily mean cloud-base height using $\theta_{v,sfc}$ and $z_{LCL,sfc}$ was smaller than those observed by the BLC and MPL. The CuP mean and inferred MPL population mean are the same at the 0.05 level of significance (P-value of 0.086). The CuP mean was found to be less than the inferred BLC population mean (P-value <0.0001). The range of CuP cloud-base heights fell within the range of uncertainty of the BLC.

The variance predicted by the CuP model was larger than the sample variance reported by the BLC. Tests showed the difference to be significant at the 0.05 level (P-

value of 0.015). All cloud-base heights reported by the MPL in the afternoon were at the same height so no sample variance was computed.

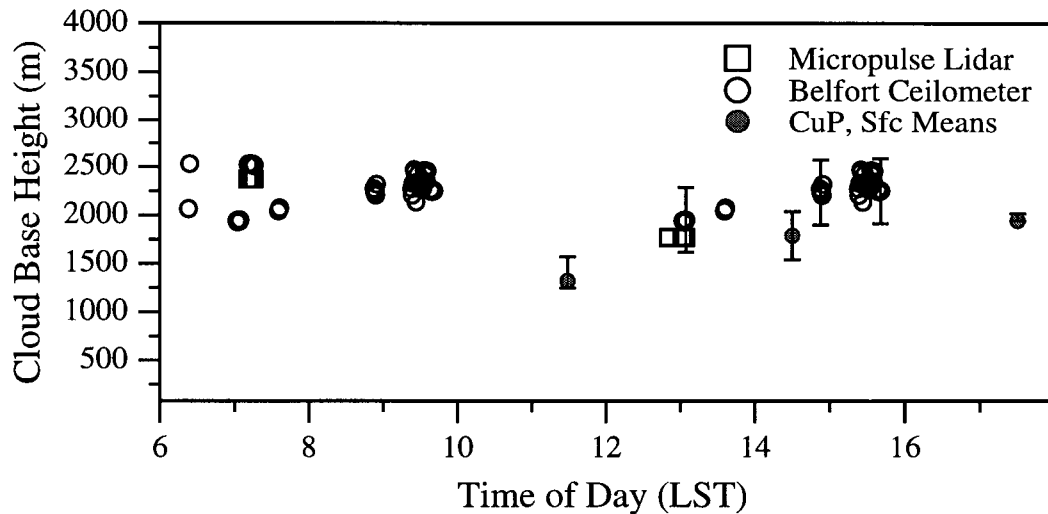


Figure 7.27. Observed and CuP model predicted cloud base height for 31 July 1994. CuP points are the predicted mode cloud-base height. Error bars correspond to range of cloud base heights predicted by the model.

7.4.5 Date: 27 June 1995

Profiles of θ_v taken from the CF sonde are shown in figure 7.28. The 0830 LST sonde stopped reporting near 7.0 km so a second sonde was launched at 0910 LST. All of the θ_v curves seemed to collapse on each other between 1.6 and 2.2 km.

The z_{LCL} plot showed that the boundary layer at 1128 is not as well mixed in the vertical as might be guessed from the θ_v profile because z_{LCL} increases with height (figure 7.29). The Betts' transition layer between the cloud and well mixed layer was evident in the z_{LCL} profiles at 1429 LST between 1.9 and 2.2 km.

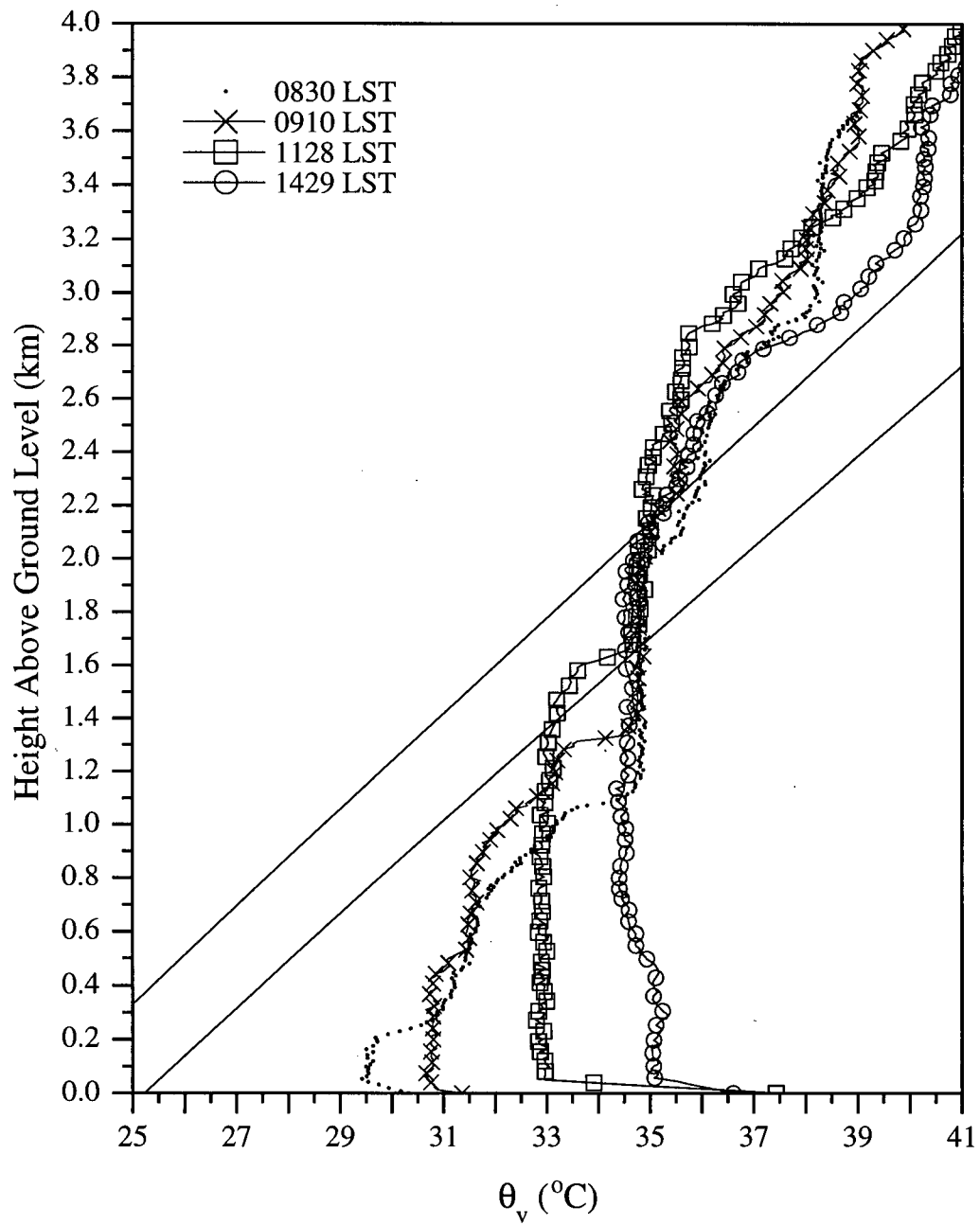


Figure 7.28. Profiles of θ_v taken from CF sondes on 27 June 1995. Solid lines are moist adiabats.

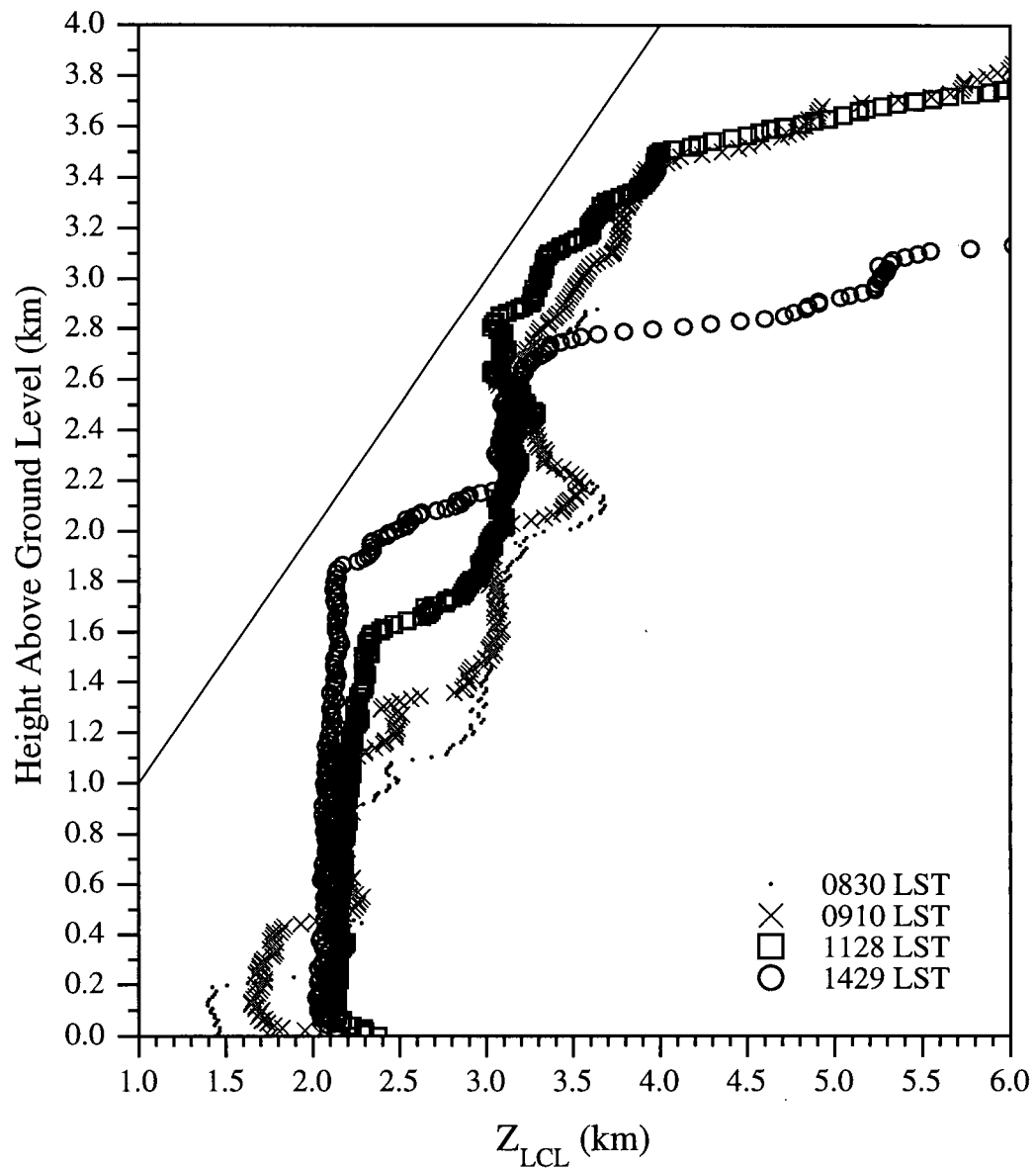


Figure 7.29. Profiles of z_{LCL} taken from CF sondes on 27 June 1995. Thin solid line is z equal to z_{LCL} . Cloudy air is above the line, clear air below.

The time evolution of the cloud cover is shown in figure 7.30. The observer at the CF reported cumulus humilis coverage near 30% at 0800 and 0900 LST, with bases near 1 or 1.5 km. The profiles of θ_v at those times showed there was a very shallow mixed layer (0.2 km). The clouds were in the residual layer and not associated with mixed-layer

physics and have not been included in figure 7.30. The BLC and the MPL did not report any cloud-base heights at those times to confirm the observed cloud bases. At 830 LST the model, using both the surface and mixed-layer mean values, predicts 0% coverage. Through the rest of the day the model over predicted the cloud coverage using the surface-layer means. At 1430 LST the model came very close to the observed values using the mixed-layer means.

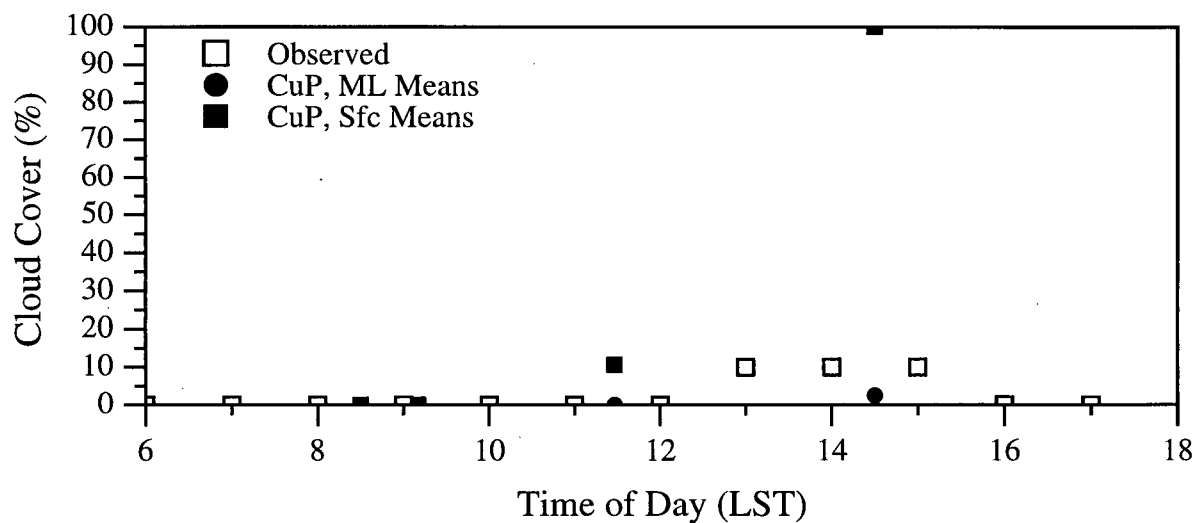


Figure 7.30. Observed and modeled cloud cover for 27 June 1995. CuP cloud cover was determined using a JFD set to the both the mixed-layer (ML) and surface-layer (Sfc) means. Cloud amounts that were above the convective boundary layer have been removed (see text for details).

CuP model estimated cloud-base heights and observed cloud-base heights are shown in figure 7.31. The CuP predictions were within the region of uncertainty of the BLC and MPL (figure 7.31). At 1130 LST no clouds were reported by the BLC or MPL. The CuP daily mean cloud-base heights were smaller than those observed by the BLC regardless of the center location of the JFD. The CuP mean was smaller than the population mean inferred from the BLC and MPL at the 0.05 level (P-values of <0.001 in

each case). Using a JFD centered at $\theta_{v,sfc}$ and $z_{LCL,sfc}$ the CuP model mean was less than the MPL inferred population mean at the 0.05 level (P-value of <0.001). Using a JFD centered at $\overline{\theta_{v,ML}}$ and $\overline{z_{LCL,ML}}$, and $\theta_{v,Best}$ and $z_{LCL,Best}$ the CuP mean cloud-base heights were close to those observed by the MPL. Tests indicated that the CuP mean and the inferred population mean from the MPL were the same (P-values of 0.190 and 0.765, respectively). While both agree with the MPL, (Table 7.3) there was stronger agreement between the MPL and the CuP model using $\theta_{v,Best}$ and $z_{LCL,Best}$.

The CuP model did a good job predicting the variance in cloud-base height. The CuP model variance using a JFD centered at $\theta_{v,sfc}$ and $z_{LCL,sfc}$ was close to both the BLC and MPL sample variances. Tests showed evidence that the variances were the same at the 0.05 level of significance (P-values of 0.37 and 0.34, respectively). The CuP model variance using a JFD set to $\overline{\theta_{v,ML}}$ and $\overline{z_{LCL,ML}}$, and $\theta_{v,Best}$ and $z_{LCL,Best}$ was less than observed sample variance. With a JFD centered at $\theta_{v,Best}$ and $z_{LCL,Best}$ there was a difference in the variances of the CuP model and the MPL (P-value of 0.045). Tests indicated that the CuP variance using $\overline{\theta_{v,ML}}$ and $\overline{z_{LCL,ML}}$ was less than the BLC and MPL observed population variance (P-values of <0.0001 and 0.014, respectively).

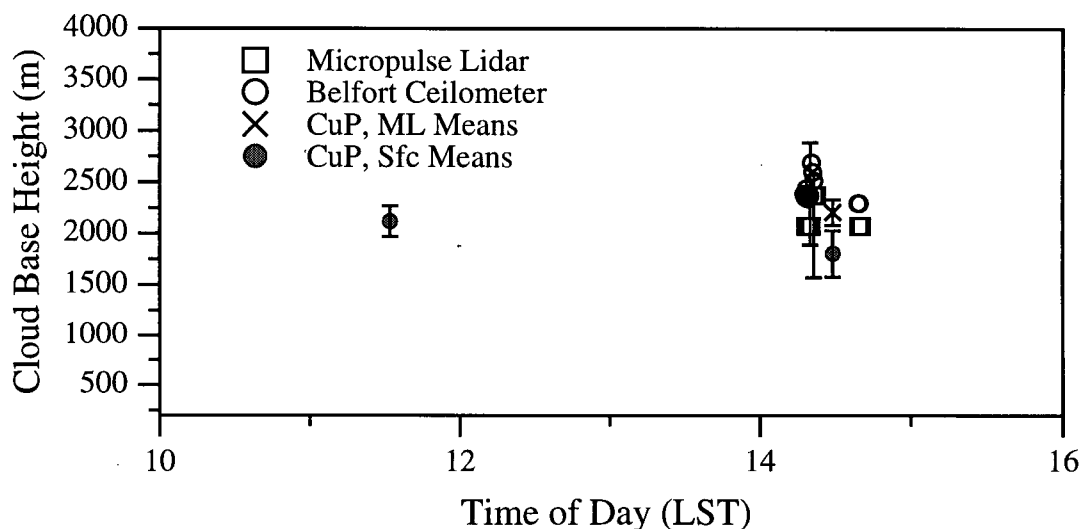


Figure 7.31. Observed and CuP modeled cloud base heights for 27 June 1995. CuP points are the predicted mode cloud-base height. Error bars on the CuP points correspond to the range of cloud base heights predicted. Note the change of scale on the vertical axis, compared to previous graphs.

7.4.6 Date: 6 July 1995

A much deeper mixed layer developed on 6 July 1995 than was observed on the other days. At 1128 LST z_i was estimated to be 1.8 km. From the θ_v profile, however it appeared that a much higher z_i might be appropriate because the inversion near 1.8 km was weak (figure 7.32). But, the profile of r showed that the well mixed layer extended to near 1.8 km where there was a 4 g kg^{-1} jump in r (figure 7.33). At 1431 LST z_i was near 3.1 km. A typical boundary-layer structure could be seen in the z_{LCL} profile at 1431 LST (figure 7.34). The well mixed layer extended from the surface to 2.2 km, a subcloud transition layer ranged from 2.2 to 2.5 km and there was a cloud layer from 2.5 to 3.3 km.

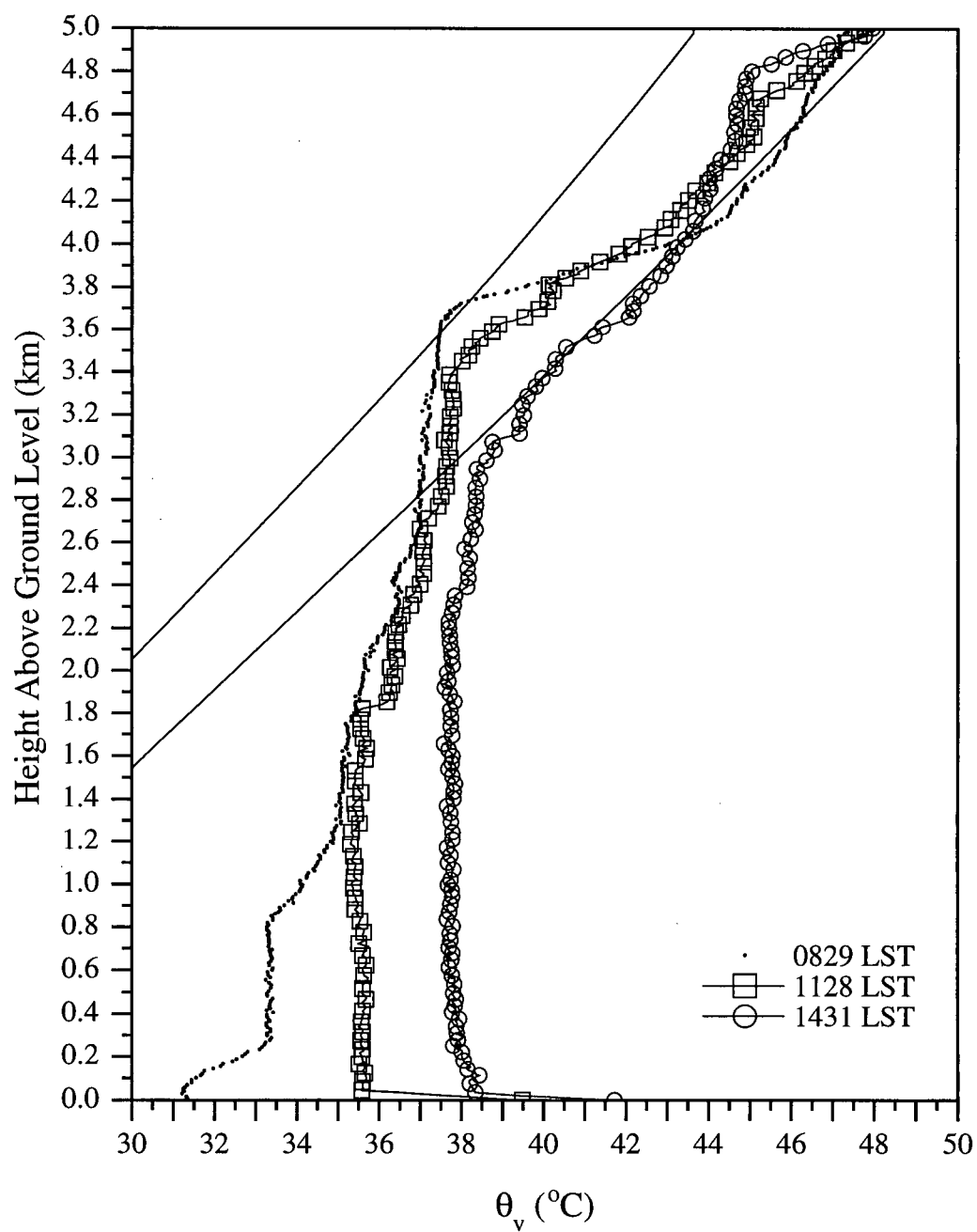


Figure 7.32. Profiles θ_v taken from CF sondes on 6 July 1995. Solid lines are moist adiabats

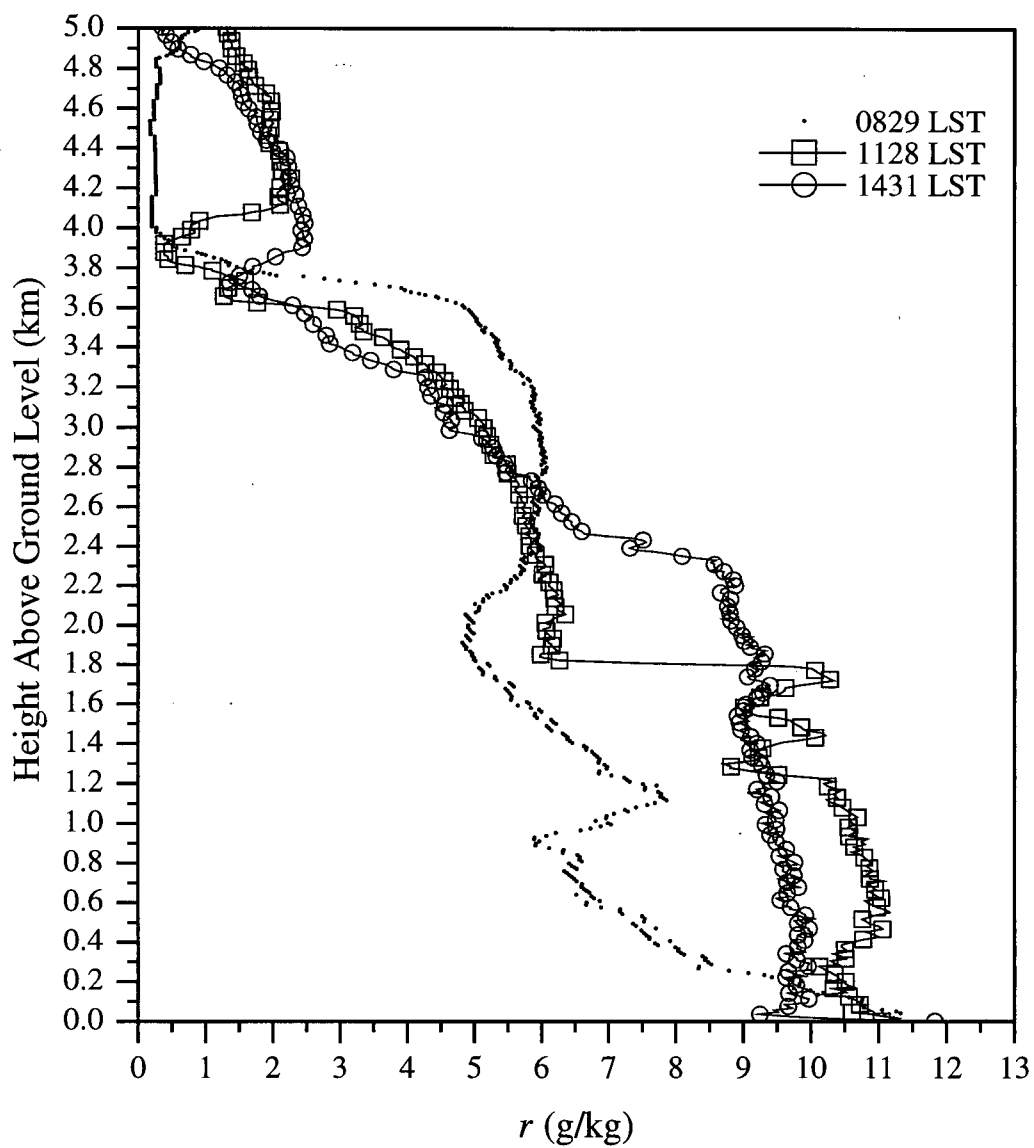


Figure 7.33. Profiles of r taken from the CF sondes on 6 July 1995

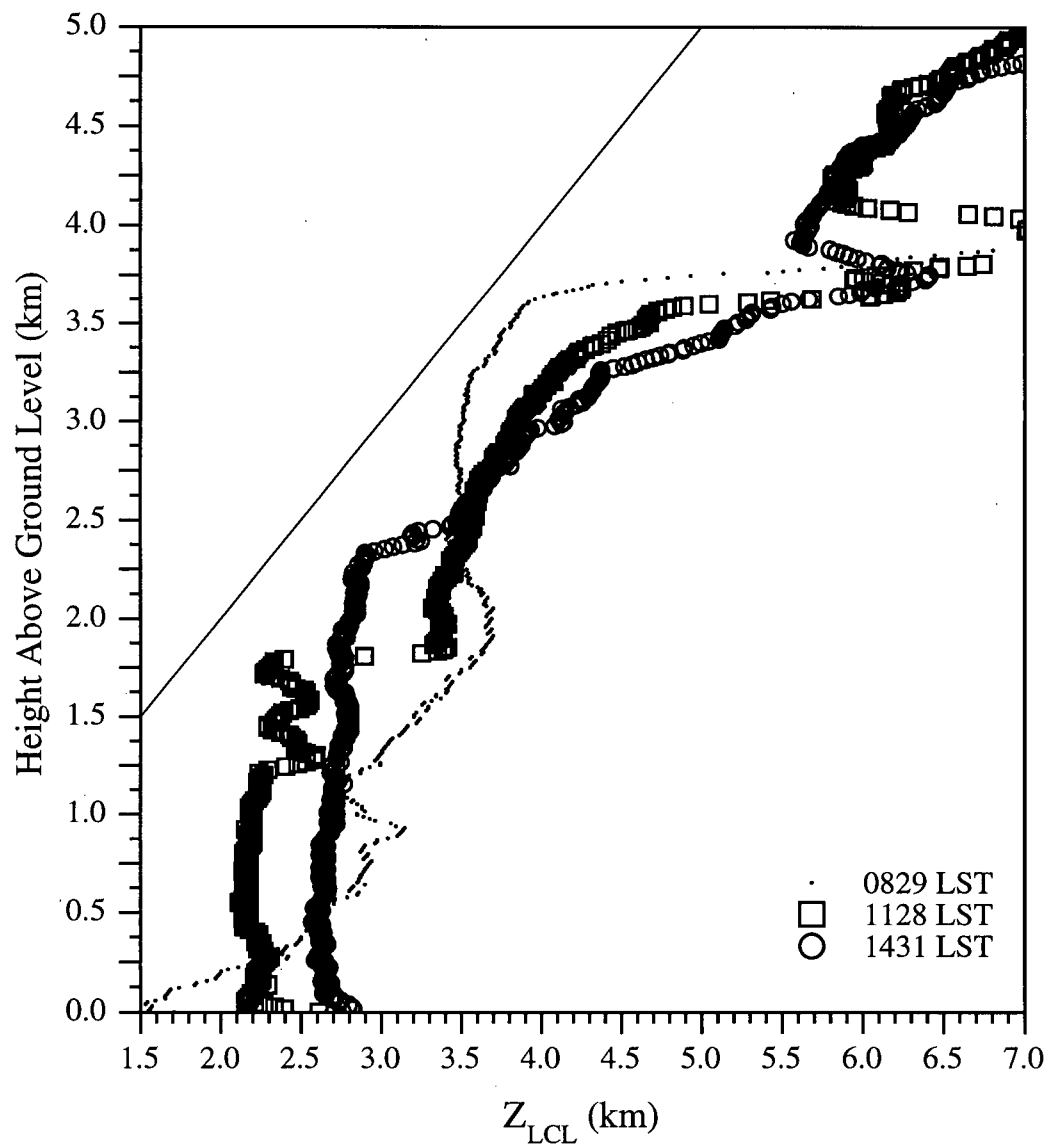


Figure 7.34. Profiles z_{LCL} taken from CF sondes on 6 July 1995. Thin solid line is z equal to z_{LCL} . Cloudy air is above the line, clear air below.

The model did a good job predicting the amount of cloud cover observed at 1431 and 1730 LST using the mixed-layer means (figure 7.35). Using the surface-layer means the model overestimated the amount of cloud cover. At 0800 and 0900 LST cumulus humilis were reported at the CF, but the CuP model predicted no cloud cover. At this time

of day the mixed layer was very shallow and the clouds were not caused by convective thermals. Neither the MPL nor the BLC reported clouds at that time. At 1100 LST some patches of altocumulus were reported. The clouds at 0800, 0900, and 1100 LST were not included in figure 7.36 because they were above the boundary layer.

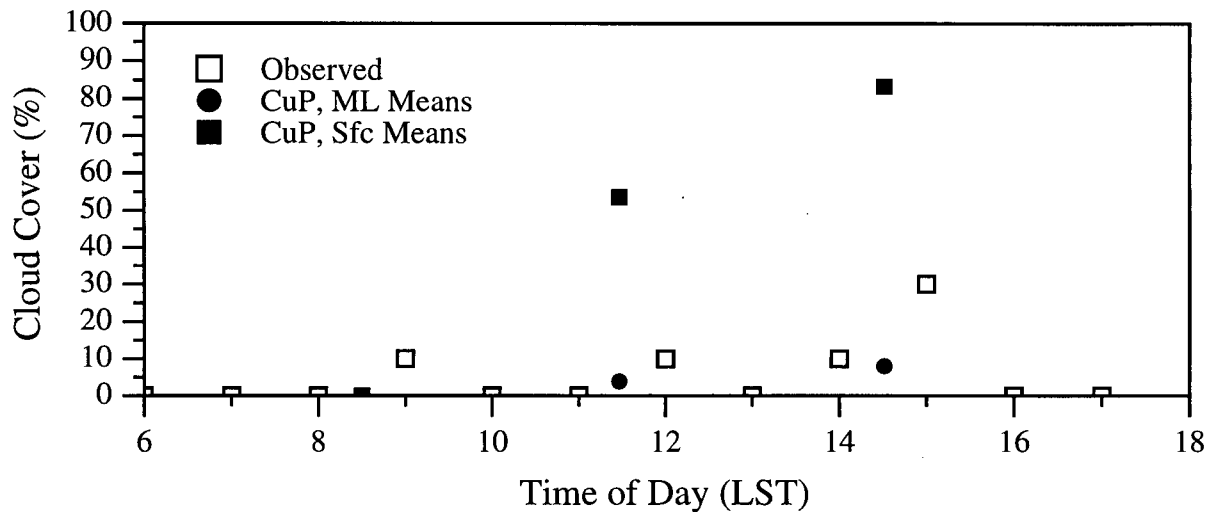


Figure 7.35. Observed and modeled cloud cover for 6 July 1995. CuP cloud cover was determined using a JFD set to the both the mixed-layer (ML) and surface-layer (Sfc) means. Cloud amounts that were above the convective boundary layer have been removed (see text for details).

Model predicted and observed cloud-base heights are shown in figure 7.36. The model mode cloud-base heights were very close to the observations. The daily mean cloud-base heights predicted by the CuP model were less than the sample mean heights observed by the MPL and BLC, with one exception. The CuP model, using a JFD centered at $\overline{\theta_{v,ML}}$ and $\overline{z_{LCL,ML}}$, and the inferred MPL population means, were the same at the 0.05 level of significance, although the test was weak because the P-value was only 0.0567.

The CuP model variances were smaller than those observed regardless of the JFD. Tests showed that the differences were significant. The P-values ranged from 0.01 between the MPL and CuP using $\overline{\theta_{v,ML}}$ and $\overline{z_{LCL,ML}}$ and <0.001 between the BLC and the CuP model using $\theta_{v,sfc}$ and $z_{LCL,sfc}$.

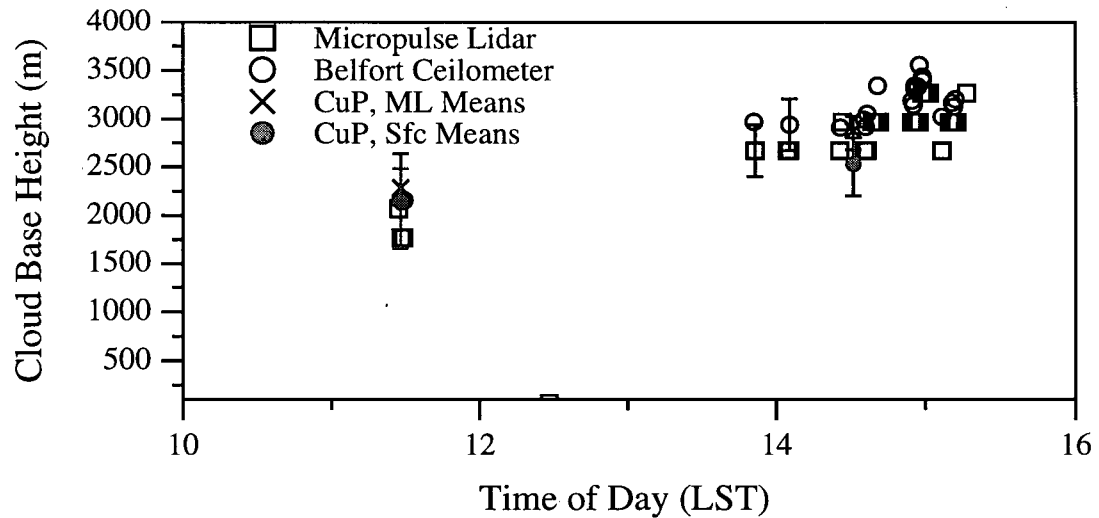


Figure 7.36. Observed and CuP predicted cloud base heights for 6 July 1995. CuP points are the predicted mode-cloud base height. Error bars on the CuP predictions correspond to the range of cloud base heights.

7.4.7 Date: 9 July 1995

While z_i was quite high on 6 July 1995, values were much lower on 9 July 1995 (figure 7.37). Values of z_i changed due to the passage of a weak surface trough overnight on 8 to 9 July 1995. A shallow mixed layer was apparent at each observation with little growth between times, probably due to subsidence over the area. The mixed layer was not very well-mixed for any of the profiles. The change in z_{LCL} with height is a good measure of how well-mixed the mixed layer is. In a perfectly well mixed layer dz_{LCL}/dz should be zero. On 9 July at 1130 LST dz_{LCL}/dz was near 0.72 and at 1430 LST it was nearly 0.3. In contrast, at 1430 LST on 13 July 1995 dz_{LCL}/dz was only 0.05.

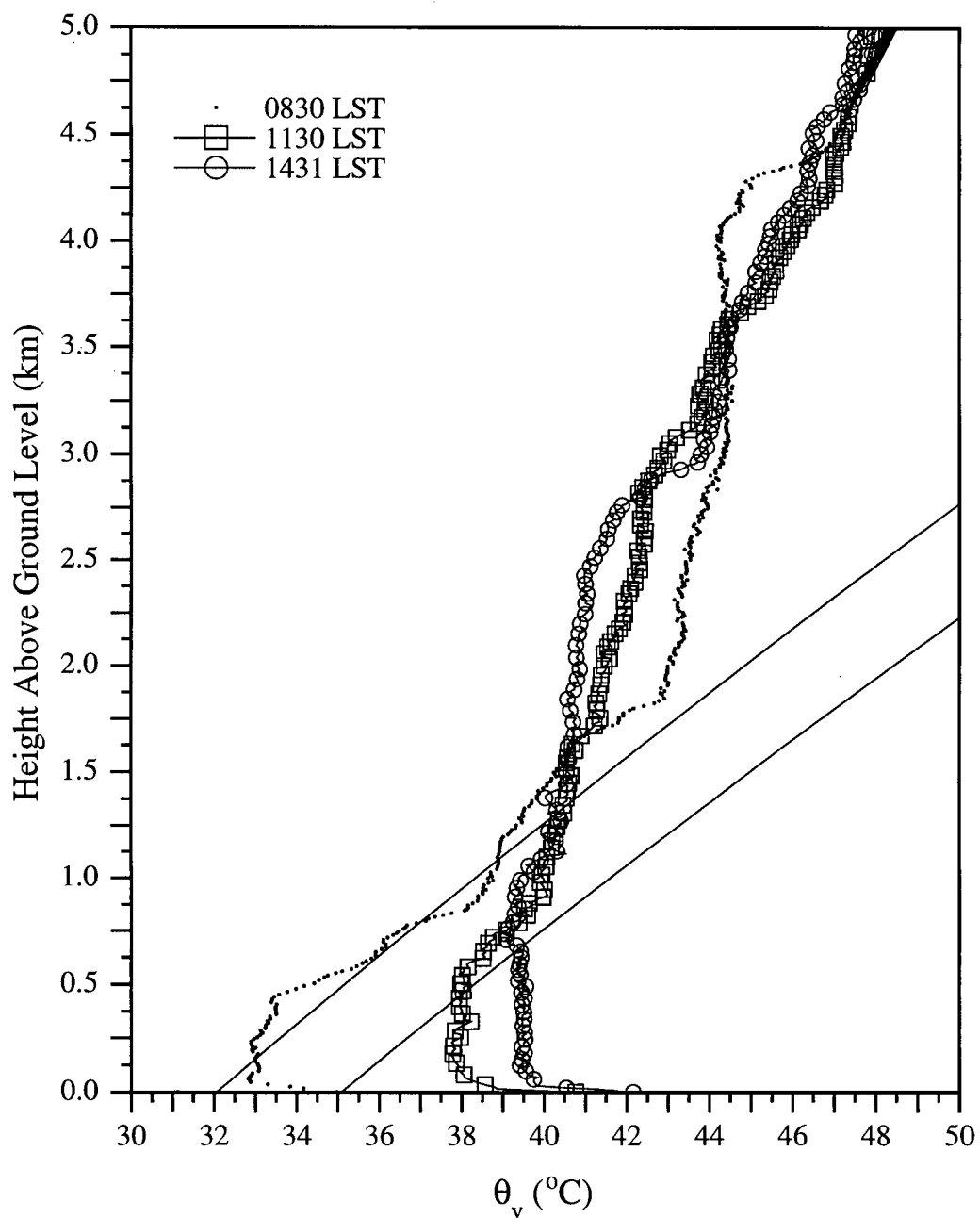


Figure 7.37. Profiles θ_v taken from CF sondes on 9 July 1995. Solid lines are moist adiabats

No low-level clouds were observed and the CuP model predicted no cloud cover at 0830 and 1130 LST. Using a JFD centered at $\overline{\theta_{v,ML}}$ and $\overline{z_{LCL,ML}}$ the model predicted no

cloud cover at 1430 LST. With a JFD centered at $\theta_{v,sfc}$ and $z_{LCL,sfc}$ the model predicted coverages near 40% at 1430 LST (figure 7.38).

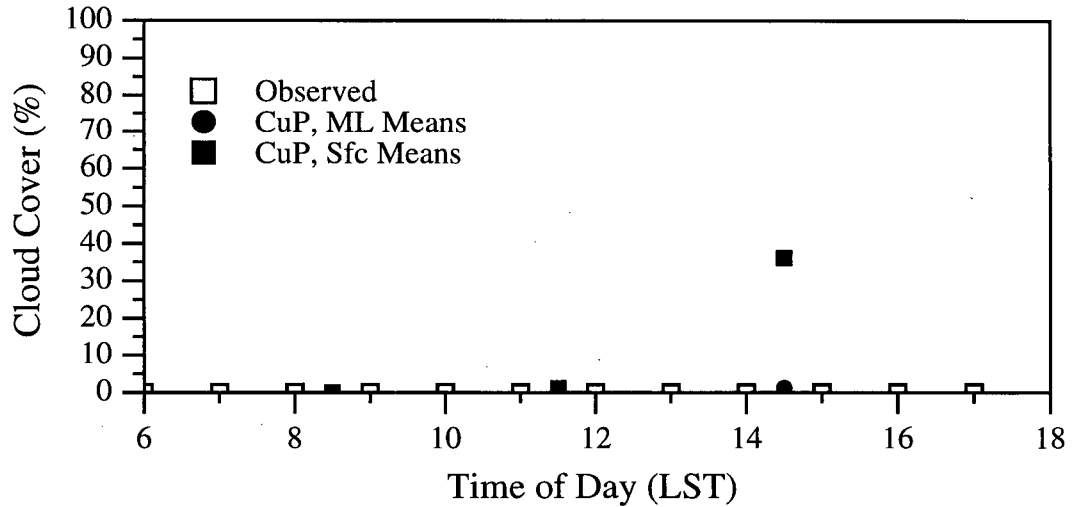


Figure 7.38. Observed and modeled cloud cover for 9 July 1995. CuP cloud cover was determined using a JFD set to the both the mixed-layer (ML) and surface-layer (Sfc) means.

7.4.8 Date: 11 July 1995

The warmest, deepest, driest mixed layer of any day used in the study occurred on 11 July. Figure 7.39 shows plots of θ_v with height. At 1130 LST the classic convective mixed layer was not apparent. There was a relative maximum near the bottom of the mixed layer in the θ_v profile, below the level of confidence for sonde measurements. The mixed-layer depth was difficult to define in this case, but was estimated to be near 0.7 km. By 1430 LST the mixed layer had taken on the classic shape and had grown to a depth of nearly 3 km. The mixed layer had also dried, so that $\overline{z_{LCL,ML}}$ was near 3.4 km. The CuP model did not predict any cloud cover using a JFD centered at $\overline{\theta_{v,ML}}$ and $\overline{z_{LCL,ML}}$, but

overestimated the cloud coverage by as much as 30% using a JFD centered at $\theta_{v,sfc}$ and $z_{LCL,sfc}$ (figure 7.40).

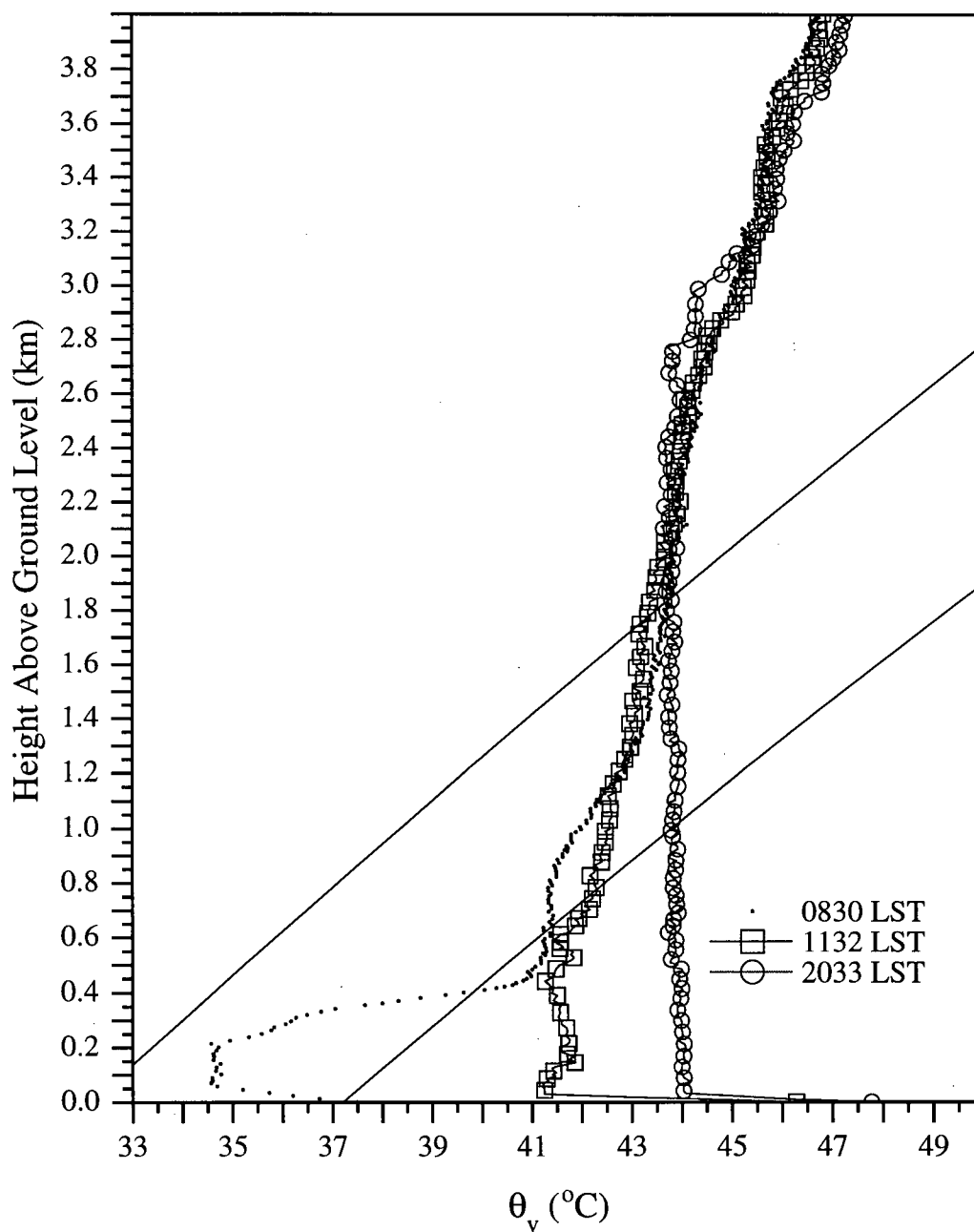


Figure 7.39. Profiles of θ_v taken from CF sondes on 11 July 1995. Solid lines are moist adiabats.

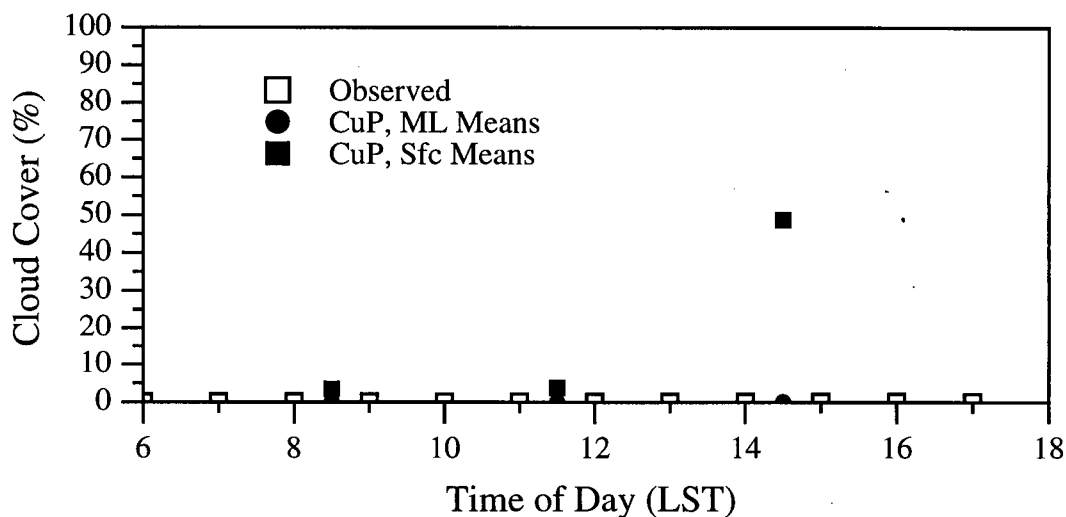


Figure 7.40. Observed and CuP modeled cloud cover for 11 July 1995. CuP cloud cover was determined using a JFD set to the both the mixed-layer (ML) and surface-layer (Sfc) means.

7.4.9 Date: 13 July 1995

Plots of θ_v are shown in figure 7.41. A well defined layer was evident at each time, although the layer was not very well mixed. There was a temperature jump at 1131 LST near 0.3 km, θ_v then decreased slowly through the top of the mixed layer. At 1430 LST there was a region near 0.6 km that was slightly warmer than the rest of the mixed layer. The profile of z_{LCL} showed that at 1131 z_{LCL} was fairly constant, while at 1430 z_{LCL} steadily increased with height throughout the layer (figure 7.42). In both cases the strange behavior seen in the θ_v profile was not apparent. At 1131 and 1430 LST the cloud layer above 2.0 km was fairly well mixed. The Betts' transition layer was evident from about 1.8 to 2.2 km at 1130 LST and from 2 to 2.2 km at 1430 LST. Above these layers was the cloud layer.

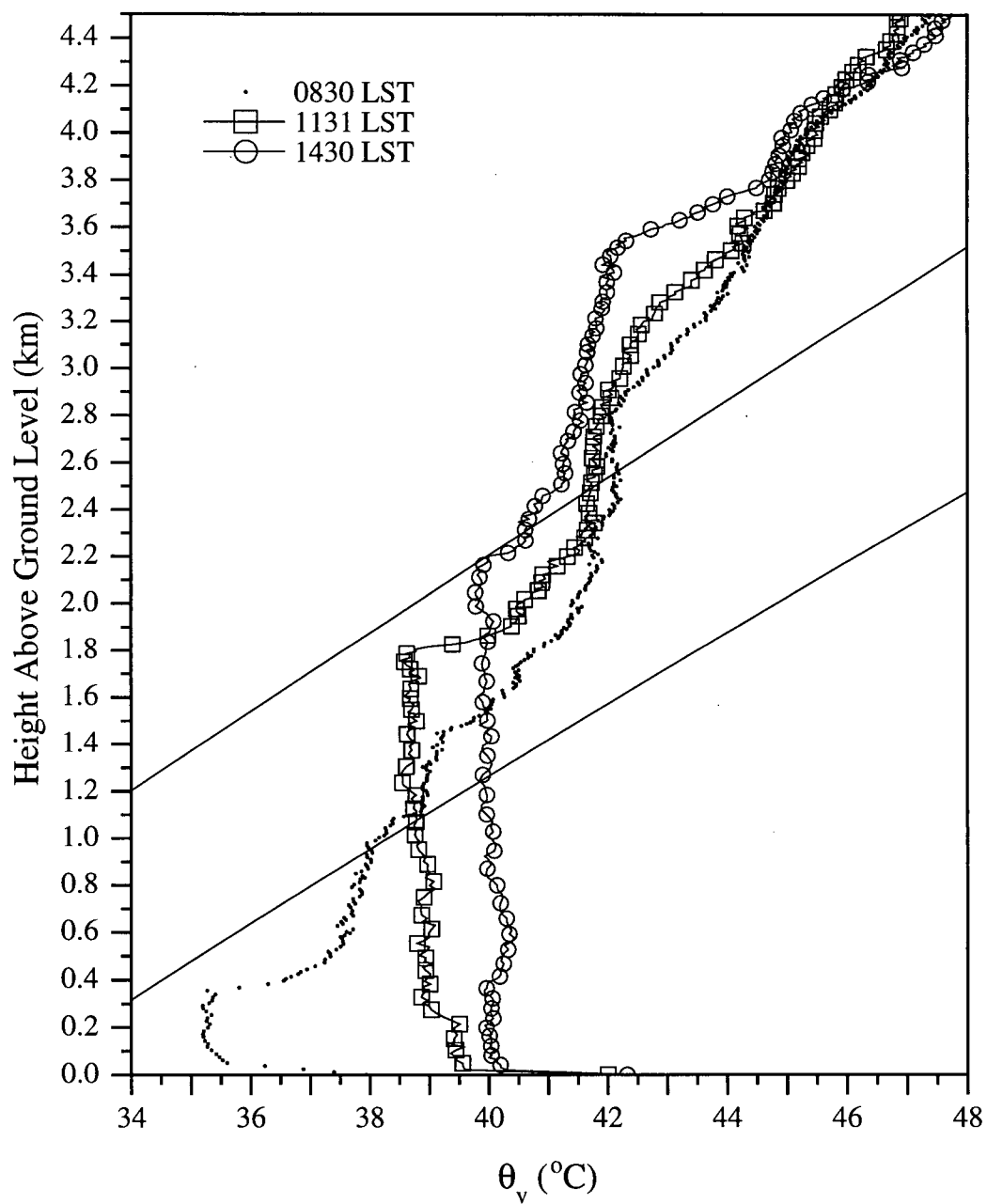


Figure 7.41. Profiles θ_v taken from CF sondes on 13 July 1995. Solid lines are moist adiabats.

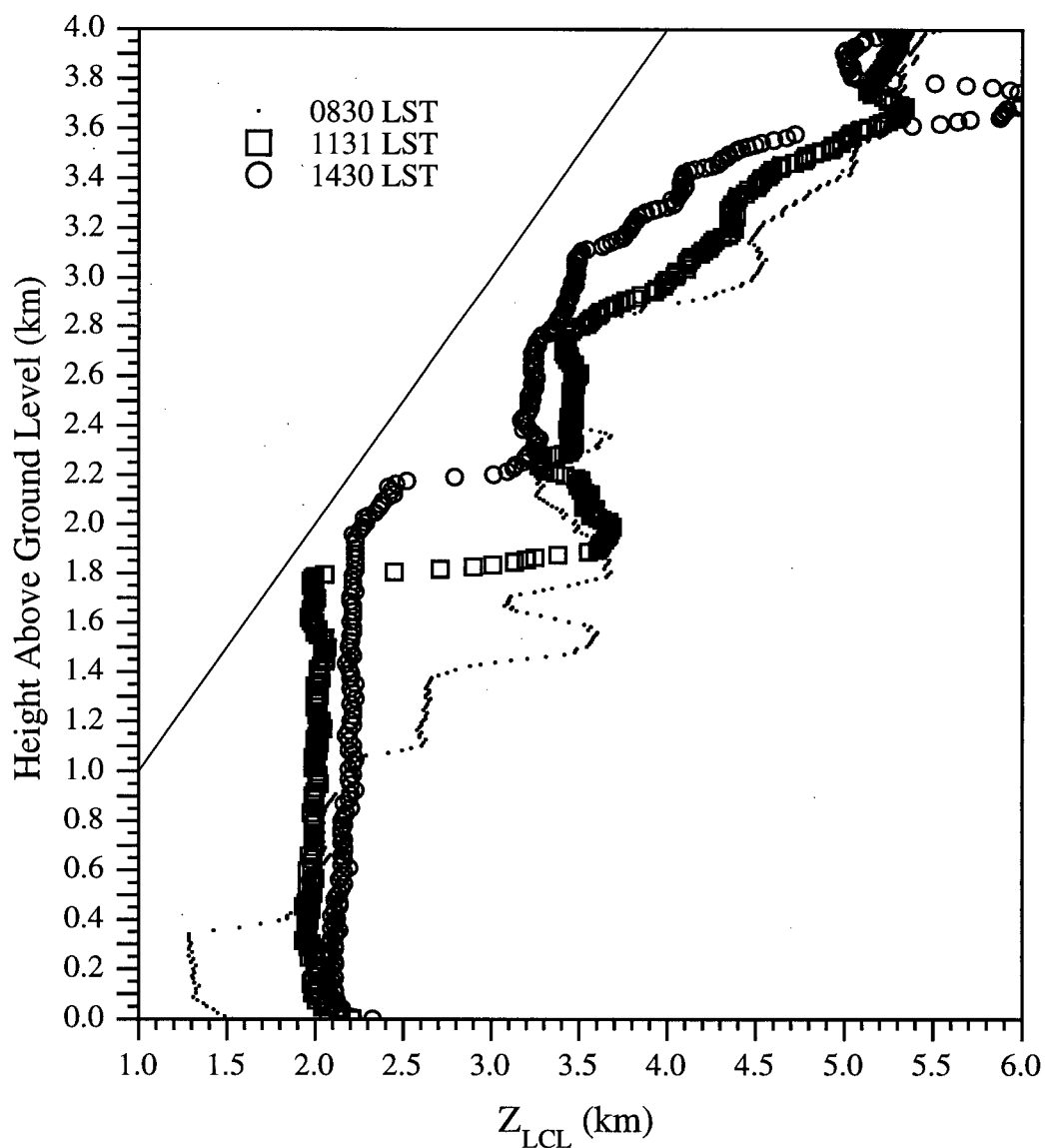


Figure 7.42. Profiles of z_{LCL} taken from CF sondes on 13 July 1995. Thin solid line is z equal to z_{LCL} . Cloudy air is above the line, clear air below.

Some scattered cloud cover was reported by the human observer near sunrise, but these have not been included in figure 7.43 because they were above the boundary layer. The CuP model, using both a JFD centered at $\overline{\theta_{v,ML}}$ and $\overline{z_{LCL,ML}}$, and $\theta_{v,sfc}$ and $z_{LCL,sfc}$ predicted no cloud cover at 830 LST. Later in the day the CuP model overestimated the

cloud coverage using a JFD centered at $\theta_{v,sfc}$ and $z_{LCL,sfc}$. At 1130 LST no cloud was estimated with a JFD at $\overline{\theta_{v,ML}}$ and $\overline{z_{LCL,ML}}$. At 1430 the model overestimate the cloud coverage, even with the mixed-layer means.

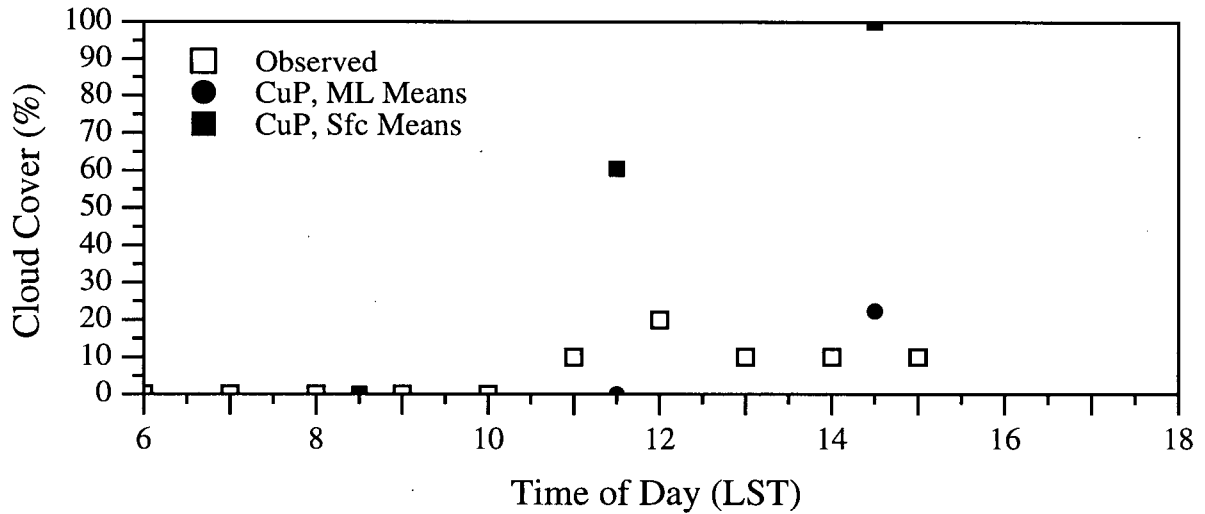


Figure 7.43. Observed and modeled cloud cover for 13 July 1995. CuP cloud cover was determined using a JFD set to the both the mixed-layer (ML) and surface-layer (Sfc) means. Cloud amounts that were determined to be disconnected from the boundary layer have been removed (see text for details).

CuP cloud base heights and observed cloud-base heights for 13 July are shown in figure 7.44. The CuP model results fell between the BLC and MPL observations. Using a JFD centered at $\overline{\theta_{v,ML}}$ and $\overline{z_{LCL,ML}}$, and $\theta_{v,sfc}$ and $z_{LCL,sfc}$ the CuP model daily mean cloud-base heights were larger than the sample mean observed by the MPL. Tests supported a difference between the CuP mean and the inferred MPL population mean (P-values <0.001). With the same JFD the CuP mean cloud-base height were smaller than the inferred BLC population mean (P-values of <0.001). Using a JFD centered at $\theta_{v,Best}$ and $z_{LCL,Best}$ the CuP mean was smaller than that observed by the BLC and slightly larger than

the MPL observations. Statistical tests indicated that the CuP mean and inferred MPL population means were the same.

Using a JFD centered at $\overline{\theta_{v,ML}}$ and $\overline{z_{LCL,ML}}$ the CuP variance was smaller than that observed by the BLC and MPL. The CuP variance and the BLC inferred population variances were the same (P-value of 0.38), but not the CuP variance and the MPL population variance (P-value of 0.01). With the JFD centered at $\theta_{v,Best}$ and $z_{LCL,Best}$ the CuP variance was greater than the sample variance obtained by the BLC, but less than the sample variance from the MPL. Tests showed that differences between the CuP and BLC were significance at the 0.05 level (P-values of <0.001). The CuP variance and the inferred MPL population variance were the same although the evidence was weak (P-value of 0.07).

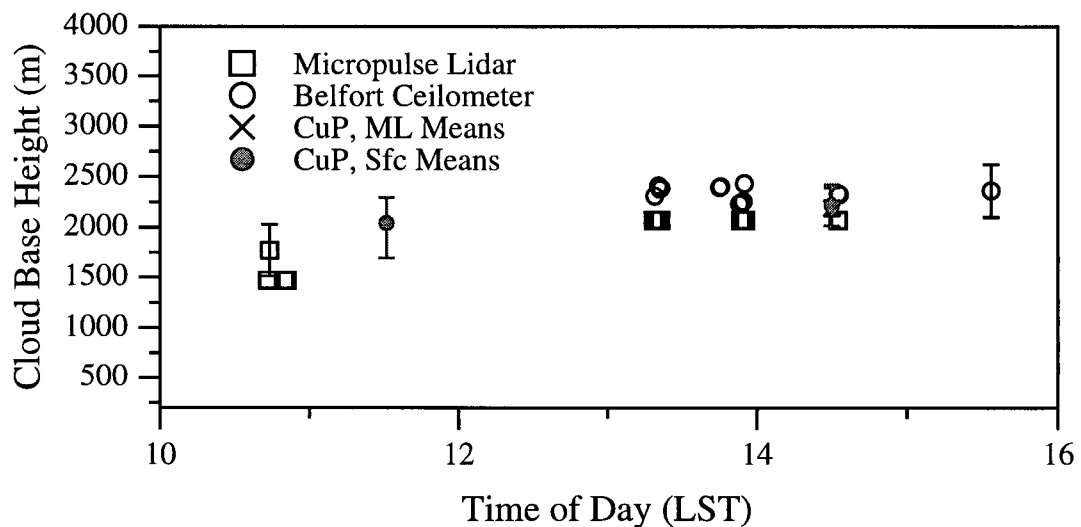


Figure 7.44. Observed and CuP modeled cloud base height 13 July 1995. CuP points are the predicted mode-cloud base height. Error bars on the CuP points correspond to range of predicted cloud base heights.

8.0 Conclusions and Future Work

The CuP model was designed to provide a quick method for determining the amount of fair-weather cumulus cloud cover, cloud onset time, cloud-base height and cloud thickness. The verification of CuP model results will be reviewed first. A discussion of some possible shortcomings and corrections will follow. A brief look at future work related to the study of both the CuP model, the JFD, and the cloud-atmosphere system will be presented.

The model showed skill predicting the cloud-base altitude. With the mean of the JFD set to the values of θ_v and z_{LCL} which gave the observed cloud cover, the predicted cloud-base estimates were nicely bracketed by the Micropulse Lidar (MPL) and Belfort Laser Ceilometer (BLC) observations. Although the predicted cloud base was greater than the MPL observations on all days, on half of the days the difference was not statistically significant. The CuP cloud-base heights estimated with the mean of the JFD set to the surface values of θ_v and z_{LCL} were greater than those observed by either the MPL or BLC, while the CuP estimates using a JFD set to the mean mixed layer θ_v and z_{LCL} were lower than those observed.

Predictions of cloud cover using a single station as input, for the case-study days were not encouraging, but also not conclusive. On the case-study days there was little skill determining the cloud cover. Using a JFD calculated from surface instruments at the Central Facility (CF) the cloud cover and variance were overestimated. Using a JFD with the same size and shape, but with it centered at the mixed-layer values of θ_v and z_{LCL} , the cloud cover and variance were underestimated.

Estimates of the vertical size distribution of clouds are provided, but no data existed to verify these results. However, on all but one of the days the cloud thicknesses were nearly log-normally distributed consistent with the observations of Lopez (1977) and Stull (1988). On some of the days the model predicted cloud thicknesses well above 8 km. These very large thicknesses are not consistent with the observations made at the CF.

8.1 Shortcomings and Improvements

Errors can be traced to four probable causes: 1) the representation of the mean mixed layer from the sondes, 2) the adequacy of the surface observations used to make the JFD, 3) the physics in the CuP model and 4) advection of clouds. From the data collected at the ARM site it is impossible to determine which scenario is dominant, although a combination of each is likely.

Work has started to address problems 1 and 2. During the summer of 1996, a field program was conducted during which high-resolution data was collected by aircraft at six heights in the mixed layer to examine how the JFD changes with height. The aircraft also measured vertical profiles from the surface to above cloud top. These aircraft profiles are more representative of the mean mixed layer than a radiosonde profile, because the plane passes through many convective thermals during its slant ascent and descent. Cloud cover will be determined from the upward looking radiometer on the plane, and from cloud cover estimates based on cloud shadows, as observed by the airborne scientist. Thus the main areas of uncertainty will be addressed with this new data source and a more conclusive determination of the CuP scheme will be possible.

The physical basis of the the CuP model will be examined. Wetzel and Boone (1995) and Wetzel (1989) have reported success using a parcel model. Crum et al. (1987) found that some parcels near the entrainment zone had mixing ratios identical to those measured near the surface, indicating individual parcels are lifted from the surface to the top of the mixed layer. The CuP model addresses only the formation of clouds due to rising thermals. Many other important physical processes, such as cloud-atmosphere interactions, cloud-cloud interactions, radiative properties of the clouds, advection, and the effects of cloud shading on the surface energy balance are not included. These physical processes could to be addressed to develop an accurate cumulus parameterization. We have hypothesized that the very deep clouds predicted by the CuP model are due to the absence of entrainment-induced evaporative cooling in the cloud. Bretherton (1988) found that clouds have some equilibrium spacing from their nearest neighbor. These type of affects are important to include in a cumulus parameterization. Unfortunately these parameters are hard to quantify for the case-study days used because, with the exception of the sondes, all of the instruments at the ARM site are surface based.

Advection is a very difficult problem which was ignored in this case study. The days used had light winds, in part to help minimize the advection of clouds and other atmospheric variables. However, the winds are rarely calm through the depth of the mixed layer so that advection could be contributing some of the cloud cover. A few possibilities exist for estimating the advection of cloud cover. One method would be to use a computer model, such as a Large Eddy Simulation (LES) model that would explicitly predict the clouds along the boundary of the case-study region. Each cloud in the model could be

tracked as it moved into or out of the study region. Problems exist with this method. The computer model would include uncertainty, and large errors in predicted cloud cover could exist. Another source of insight into the advection would be a time series of satellite images. Individual cloud fields could be tracked and the advection of clouds estimated. A difficulty of this method would be tracking individual cloud fields from the relatively coarse resolution satellite data.

8.2 Other Future Work

A more complete statistical picture of the cloud cover will be constructed from data at the ARM site for comparison with the CuP model. Hourly human observations will be combined with the MPL, BLC, and the whole sky imager data to construct longer term statistics.

Investigation of the skill of the CuP's predicted cloud onset time could be done using data from a more continuous ground-based sensor, although in general at the expense of vertical resolution. The CuP model could also be placed into a meso-scale or boundary-layer forecast model to utilize greater temporal resolution and gain a more representative picture of the mean-mixed layer.

In section 6 we showed that the cloud characteristics predicted by the CuP model were very sensitive to the atmospheric conditions. It is important to determine if the formation of boundary-layer cumulus in the atmosphere is equally sensitive. A LES model could be used to help determine the sensitivity of the real atmosphere, assuming an accurate representation of cloud formation and other boundary-layer processes in the model. Small random perturbations could be added to the LES parameters to ascertain the sensitivity of

the cloud-atmosphere system. If the atmosphere is as sensitive as the CuP model, then the accurate prediction of boundary-layer cumulus clouds in AGCMs would be impossible due to inherent uncertainty in the AGCM. In many cases the behavior of the atmosphere has been shown to have a sensitive dependence on the initial conditions, the formation of boundary-layer cumulus could be an example.

A boundary-layer cumulus scheme needs to be further developed to include both forced and free convection. This will allow forecasts of different cloud types with the same parameterization. Perhaps rather than looking at θ_v to determine buoyancy, some other energy parameter could be used that includes both forced and free convection.

REFERENCES

- Angevine, W. M., A. B. White, and S. K. Avery, 1994: Boundary-layer depth and entrainment zone characterization with a boundary-layer profiler. *Boundary-Layer Meteo.*, **68**, 375-385.
- Avissar, R., 1992: Conceptual aspects of a statistical-dynamic approach to represent landscape subgrid-scale heterogeneities in atmospheric models. *J. Geophys. Res.*, **79**, 2729-2742.
- Avissar, R. and R. A. Pielke, 1989: A parameterization of heterogeneous land surface for atmospheric numerical models and its impact on regional meteorology. *Mon. Wea. Rev.*, **117**, 2113-2136.
- Barnes, S. L., 1968: An empirical shortcut to the calculation of temperature and pressure at the lifted condensation level. *J. Appl. Meteor.*, **7**, 511.
- Betts, A. K., 1982a: Saturation point analysis of moist convective overturning. *J. Atmos. Sci.*, **39**, 1484-1505.
- Betts, A. K., 1982b: Cloud thermodynamic models in saturation point coordinates. *J. Atmos. Sci.*, **39**, 2182-2191.
- Betts, A. K., 1985: Mixing line analysis of clouds and cloudy boundary layers. *Atmos. Sci.*, **42**, 2751-2763.
- Bretherton, C. S., 1988: A theory for nonprecipitating convection between two parallel plates. Part II: nonlinear theory and cloud field organization. *J. Atmos. Sci.*, **45**, 2391-2415.
- Cahalan, R. F., 1991: LANDSAT observations of fractal cloud structure. *Non-Linear Variability in Geophysics*, D. Schertzer and S. Lovejoy Eds., Kluwer Academic Publishers, 281-295.
- Chen, F., and R. Avissar, 1994: Impact of land-surface moisture variability on local shallow convective cumulus and precipitation in large-scale models. *J. Appl. Meteor.*, **33**, 1382-1401.
- Crum, T. D., and R. B. Stull, 1987: Field Measurements of the amount of surface layer air versus height in the entrainment zone. *J. Atmos. Sci.*, **44**, 2743-2753.
- Deardorff, J. W., G. E. Willis, and B. H. Stockton, 1980: Laboratory studies of the entrainment zone of a convective mixed layer. *J. Fluid Mech.*, **100**, 41-64.

- Doran, J. C., S. Zhong, 1995: Variations in mixed layer depths arising from inhomogeneous surface conditions. *J. of Climate*, **8**, 1965-1973.
- Driedonks, A. G. M., 1982: Models and observations of the growth of the atmospheric boundary layer. *Boundary-Layer Meteor.*, **23**, 281-306.
- Hong X., M. J. Leach, and S. Raman, 1995: A sensitivity study of convective cloud formation by vegetation forcing with different atmospheric conditions. *J. Appl. Meteor.*, **34**, 2008-2028.
- Hozumi, K., T. Harimaya, and C. Magono, 1982: The size distribution of cumulus clouds as a function of cloud amount. *J. Meteor. Soc. Japan*, **60**, 691-699.
- Joseph, J. H., and R. F. Cahalan, 1990: Nearest neighbor spacing of fair weather cumulus clouds, *J. Appl. Meteor.*, **29**, 793-805.
- Kirkpatrick, E. G., 1974: *Introductory Statistics and Probability for Engineering, Science, and Technology*. Prentice-Hall, 446 pp.
- Liu, Yongiang, and R. Avissar, 1996: Sensitivity of shallow convective precipitation induced by land-surface heterogeneities to dynamical and cloud microphysical parameters. *Second International Scientific Conference on the Global Energy and Water Cycle*. Washington D. C., World Climate Research Programme., 411.
- Lopez, R. E., 1977: The log-normal distribution and cumulus cloud populations. *Mon. Wea. Rev.*, **105**, 865-872.
- Malkus, J. A., 1958: On the structure of the trade wind moist layer. *Papers in Physical Oceanography and Meteorology*. Contr # 969. Woods Hole Ocean. Inst. 47pp.
- Noilhan, J., and S. Planton 1989: A simple parameterization of land surface processes for meteorological models. *Mon. Wea. Rev.*, **117**, 536-549.
- Plank, V. G., 1969: The size distribution of cumulus clouds in representative Florida populations. *J. Appl. Meteor.*, **8**, 46-67.
- Raga, G. B., and P. R. Jonas, 1993: Microphysical and radiative properties of small cumulus clouds over the sea. *Q. J. Meteor. Soc.*, **119**, 1399-1417.

- Rabin, R. M., S. Stadler, P. J. Wetzel, D. J. Stensrud, and M. Gregory, 1990: Observed effects of landscape variability on convective clouds. *Bull. Amer. Meteor. Soc.*, **71**, 272-280.
- Ruffner, J. A., 1985: *Climates of the States*. Gale Research Co, Detroit. 1572 pp.
- Schrieber, K., R. B. Stull, and Q. Zhang, 1996: Distribution of surface-layer buoyancy verses lifting condensation level over a heterogeneous land surface. *J. Atmos Sci.*, **53**, 1086-1107.
- Sengupta, S. K., R. M. Welch, M. S. Navar, T. A. Berendes, and D. W. Chen, 1990: Cumulus cloud field morphology and spatial patterns derived from high spatial resolution Landsat imagery. *J. Appl. Meteor.*, **29**, 1245-1267.
- Siebert, J., U. Sievers, and W. Zdunkowski, 1992: A one-dimensional simulation of the interaction between land surface processes and the atmosphere. *Boundary-Layer Meteo.*, **59**, 1-34.
- Slingo, J. M., U. C. Mohanty, M. Tiedtke, and R. P. Pearce, 1988: Prediction of the 1979 summer monsoon onset with modified parameterization schemes. *Mon. Wea. Rev.*, **116**, 328-346.
- Slingo, J. M., 1987: The development and verification of a cloud prediction scheme for the ECMWF model. *Q. J. Meteor. Soc.*, **113**, 899-927.
- Smith, R. N. B., 1990: A scheme for predicting layer clouds and their water content in a general circulation model. *Q. J. Meteor. Soc.*, **116**, 435-460.
- Splitt, M. E., P. J. Lamb, and D. L. Sisterson, 1995: *Site scientific mission plan for the southern great plains CART site, July-December 1995*. ARM-95-002, Argonne National Laboratory, Argonne, Illinois.
- Stull, R. B., 1992: Impact of boundary-layer clouds--a case study of cover hours. *J. of Climate*, **5**, 390-394.
- Stull, R. B., 1988: *An Introduction to Boundary Layer Meteorology*. Kluwer Academic Publishers, 666 pp.
- Stull, R. B. E. Santoso, L. K. Berg, J. Hacker, 1996: Boundary layer experiment 1996. Submitted to *Bull. Amer. Meteor. Soc.*

- Stull, R. B., and K. M. Schrieber, 1995: Size distributions of boundary-layer clouds. *11th Symposium on Boundary Layers and Turbulence*, Charlotte, NC, Amer. Meteor. Soc., 217-219.
- Stull, R. B., and E. Eloranta, 1985: A case study of the accuracy of routine fair-weather cloud-base reports. *Natl. Wea. Dig.*, **10**, 19-24.
- Sud, Y. C., W. C. Chao, and G. K. Walker: Contributions to the implementation of the Arakawa-Schubert cumulus parameterization in the GLA GCM. *J. Atmos Sci.*, **48**, 1573-1586
- Weger, R. C., J. Lee, T. Zhu, and R. M. Welch, 1992: Clustering, randomness, and regularity in cloud fields: 1. theoretical considerations. *J. Geophys. Res.*, **97**, 20519-20536.
- Wetzel, P. J., 1990: A simple parcel method for prediction of cumulus onset and area-averaged cloud amount over heterogeneous land surfaces. *J. Appl. Meteor.*, **29**, 516-523
- Wetzel, P. J., and A. Boone, 1995: A parameterization for land-atmosphere-cloud exchange (PLACE): Documentation and testing of a detailed process model of the partly cloudy boundary layer over heterogeneous land. *J. of Climate*, **8**, 1810-1837.
- White, A. B., C. W. Fairall, and D. E. Wolfe, 1991: Use of 915 MHz wind profiler data to describe the diurnal variability of the mixed layer, in Preprints, 7th Joint Conference on Applications of Air Pollution Meteorology with AWMA, New Orleans, Jan 14-18, 1991, Amer. Meteor. Soc., pp J161-J166.
- Wielicki, B. A., and R. M. Welch, 1986: Cumulus cloud properties derived using Landsat satellite data. *J. Climate Appl. Meteor.*, **25**, 261-276.
- Wilde, N. P., R. B. Stull, and E. W. Eloranta, 1985: The LCL Zone and Cumulus Onset. *J. of Climate and Appl. Meteor.*, **24**, 640-657.
- Williams, A. G., and J. M. Hacker, 1992: The composite shape and structure of coherent eddies in the convective boundary layer. *Boundary-Layer Meteor.*, **61**, 213-245.
- Tiedtke, M., 1993: Representation of clouds in large-scale models. *Mon. Wea. Rev.*, **121**, 3040-3061.

- Tiedtke, M., 1989: A comprehensive mass flux scheme for cumulus parameterization in large-scale models. *Mon. Wea. Rev.*, **117**, 1779-1799.
- Turner D. D., 1996: Comparisons of the Micropulse Lidar and the Belfort Laser Ceilometer at the ARM SGP CART. U.S. Department of Energy, 1990: Atmospheric Radiation Measurement Program Plan, 1990, DOE/ER-0441. Washington D. C.
- Xu, K., and S. K. Krueger, 1991: Evaluation of cloudiness parameterizations using a cumulus ensemble model. *Mon. Wea. Rev.*, **119**, 342-367.
- Zhu, T., J. Lee, R. C. Weger, and R. M. Welch, 1992: Clustering, randomness, and regularity in cloud fields: 2. cumulus cloud fields. *J. Geophys. Res.*, **97**, 20537-20558.

Appendix A. Instrument Uncertainty

Table A.1. Accuracy of SMOS pressure, humidity and precipitation measurements. Precipitation uncertainty increases in cases of high winds and heavy rain greater than 75 mm hr^{-1} (Wesely personal communication 1996).

Measurement	Accuracy
Pressure	$\pm 0.035 \text{ kPa}$
Humidity	$\pm 2.06\%$ for relative humidity less than 90% $\pm 3.04\%$ for relative humidity greater than 90%
Precipitation	$\pm 0.254 \text{ mm}$

Table A.2. Wind accuracy for a given wind speed for SMOS 13 (Wesely personal communication 1996)

Wind Speed	Speed Accuracy	Direction Accuracy
2.5 to 30 m/s	$\pm 1\%$	$\pm 5^\circ$
2.0 m/s	-0.12 to $+0.02$	$\pm 5^\circ$
1.5 m/s	-0.22 to $+0.00$	$\pm 5^\circ$
1.0 m/s	-0.31 to -0.20	$\pm 180.0^\circ$
0.5 m/s	-0.51 to -0.49	$\pm 180.0^\circ$

Table A.3. Temperature accuracy for a given wind speed for SMOS 13 (Wesely personal communication 1996)

Wind Speed	Accuracy
≥ 6.00 m/s	± 0.45 °C
3.00 m/s	± 0.89 °C
2.00 m/s	± 1.46 °C
1.00 m/s	± 3.07 °C

Table A.4. Accuracy of EBBR measurements (Wesely personal communication 1996).

Measurement	Accuracy
Pressure	± 0.14 kPa
Temperature	± 0.5 °C
Humidity	$\pm 2\%$ for relative humidity less then 90% $\pm 3\%$ for relative humidity greater then 90%

Table A.5. Accuracy of sonde measurements (Wesely personal communication 1996).

Measurement	Accuracy
Pressure	± 0.05 kPa
Temperature	± 0.2 °C
Humidity	$\pm 2\%$
Wind direction	$\pm 5^\circ$
Wind speed	± 0.1 m/s

Appendix B. Comparison of Empirical and Parcel Determination of z_{LCL}

Table B.1. Values z_{LCL} calculated from equation 4.7 and calculated from an iterative method for 27 July 1994, 1430 LST. Difference is the absolute value of the difference in the two methods. Difference (%) is the calculated from the iterative method and the difference.

Pressure (kPa)	z_{LCL} (km) from Approximation	z_{LCL} (km) from Iteration	Difference (m)	Difference (%)
97.97	2.375	2.368	6.891	0.291
95.91	2.223	2.208	15.207	0.689
94.95	2.248	2.242	6.717	0.300
94.03	2.220	2.208	12.308	0.557
93.02	2.214	2.208	5.732	0.260
92.05	2.204	2.194	10.186	0.464
91.05	2.236	2.225	10.238	0.460
90.07	2.203	2.194	9.314	0.424
89.07	2.174	2.176	1.975	0.091
87.99	2.228	2.225	2.195	0.099
86.98	2.276	2.268	7.869	0.347
86.01	2.270	2.268	2.724	0.120
85.05	2.290	2.292	1.571	0.069
80.02	2.424	2.422	1.905	0.079
75.00	2.806	2.814	8.154	0.290
70.01	6.151	6.004	147.666	2.460
64.99	7.264	7.073	190.253	2.690
60.05	6.831	6.713	118.813	1.770

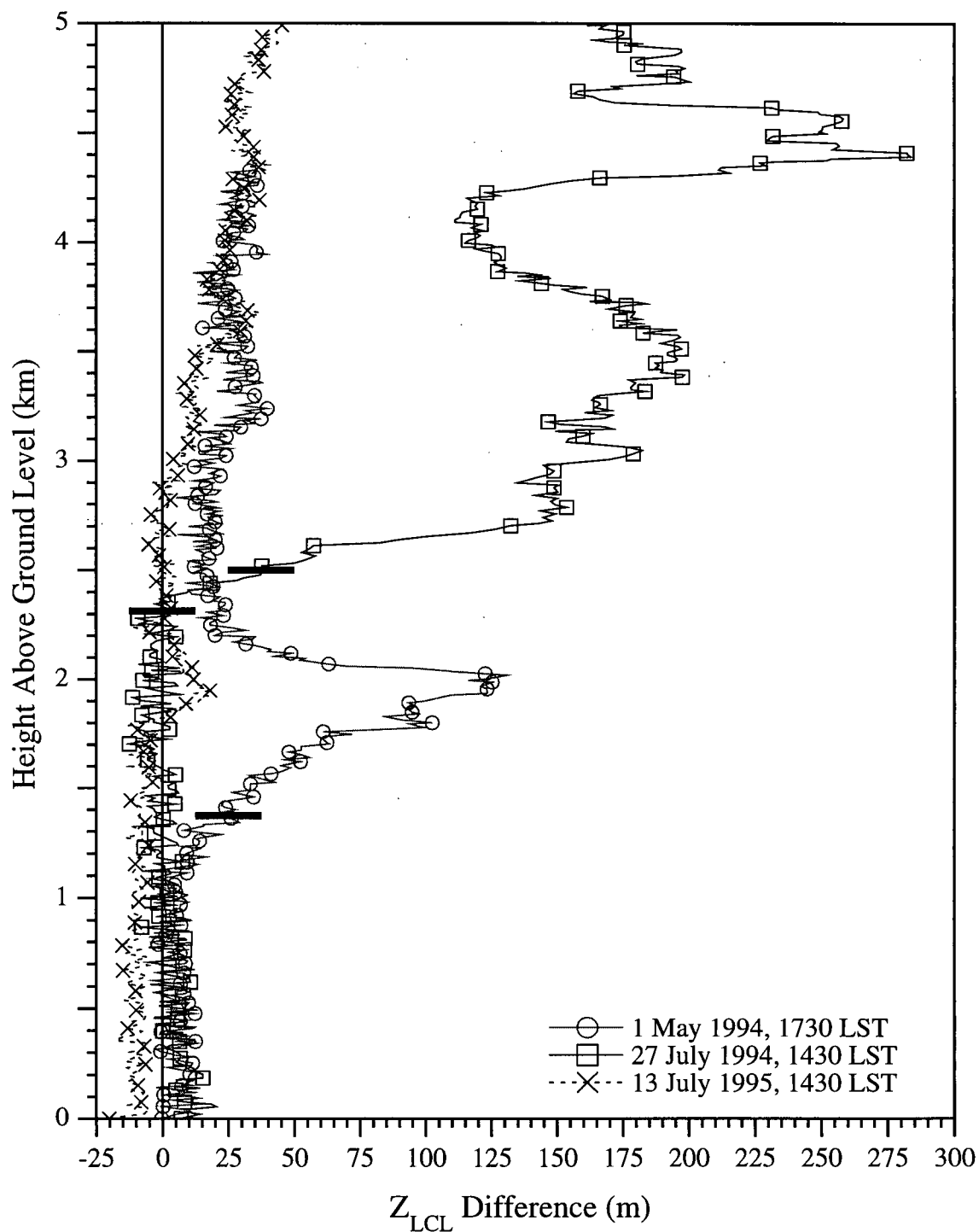


Figure B.2. Difference between z_{LCL} calculated from empirical equation 4.2 and parcel method using the CF sonde. Both methods are described in section 4. Thick solid lines mark z_i for that day and time. There is good agreement between the two methods, especially in the boundary layer.

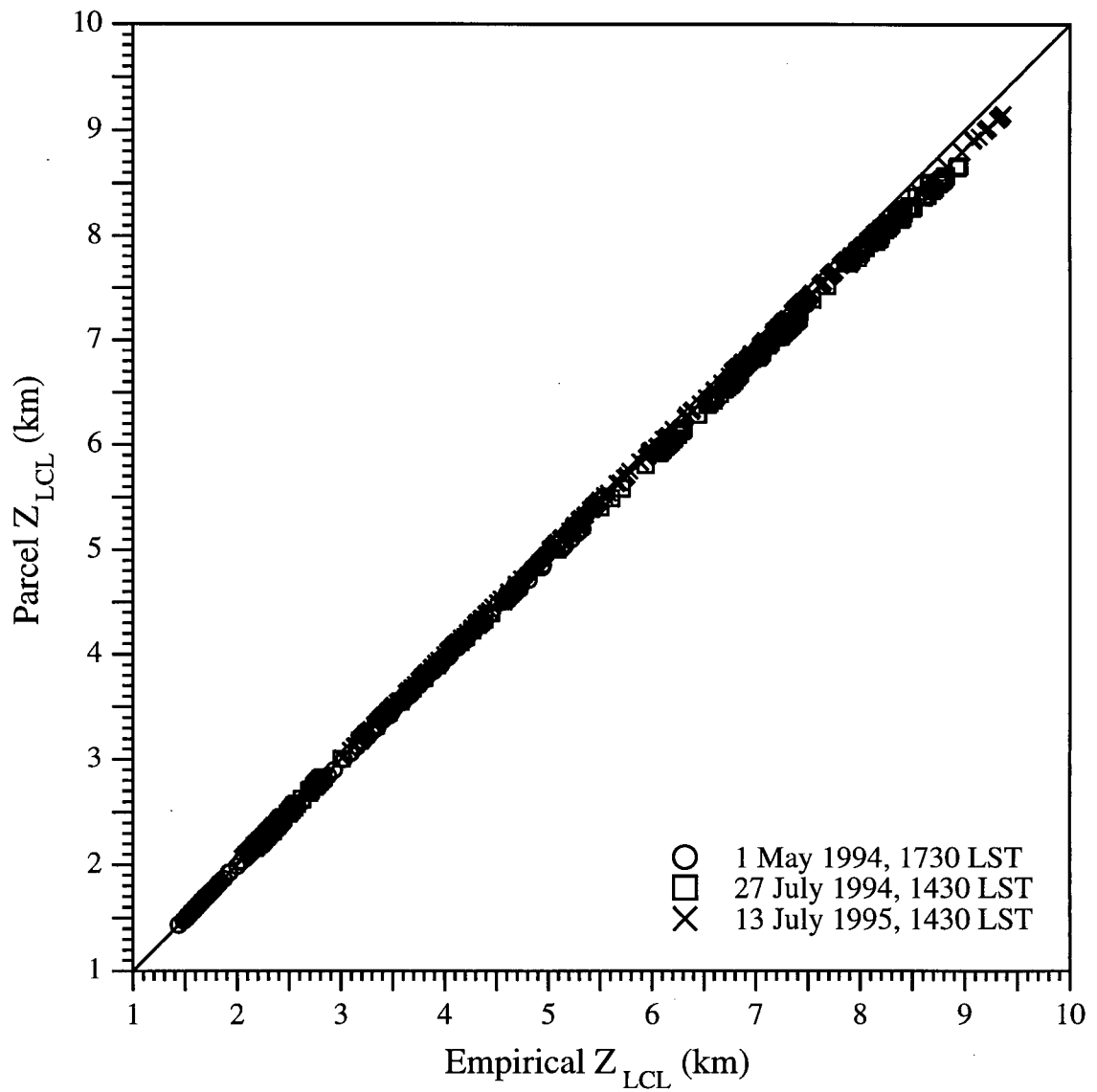


Figure B.3. The z_{LCL} found from the parcel method vs z_{LCL} the calculated using equation 4.2 for three of the case-study days. The straight line is perfect agreement.

Appendix C. Sample Error Calculation

Uncertainties in calculated quantities arise from errors in measured variables. Standard error analysis techniques were used to estimate error propagation (e.g. Bevington 1969). In this appendix the general equations and a specific example will be presented. A temperature of 20 °C and a relative humidity of 88% are assumed. The uncertainty in temperature was ± 0.89 °C, while the uncertainty in relative humidity was 2.06%, as defined for the SMOSs. Uncertainty in the measured pressure for the SMOS is ± 0.035 kPa.

C.1 Error Calculation for θ_v

The atmospheric water vapor mixing ratio (r) was calculated in several steps. Teten's equation is used to find the saturation vapor pressure (e_s):

$$e_s = e_{so} \exp \left[\frac{a(T - 273.16)}{(T - b)} \right] \quad (C1)$$

where a is 17.2694, b is 35.86, T is the temperature in K, and e_{so} is the saturation vapor pressure at the triple point of water. The uncertainties in saturation vapor pressure using Teten's Equation is found in several steps. First the error inside the square brackets of equation C1 will be found. We will let N be the numerator, err_N be the error in numerator as represented by the standard deviation, D be the denominator, and err_D be the error in denominator as represented by the standard deviation. The error propagation from multiplying a variable by a constant is:

$$err_{product} = \pm a(err_A) \quad (C2)$$

where err_A is the uncertainty and a is a constant. Using (C2) the error in our example case becomes:

$$err_N = \pm a(err_T) = \pm(17.2694 \times 0.89) = \pm 15.369 \quad (C3)$$

The value of N is 345.388. The error in the denominator, err_D is err_T . The value of D is 257.3. The error propagation due to the division is:

$$err_{div} = \frac{N}{D} \sqrt{\left(\frac{err_N}{N}\right)^2 + \left(\frac{err_D}{D}\right)^2} \quad (C4)$$

Equation (C4) becomes:

$$err_{div} = \pm \frac{345.388}{257.3} \sqrt{\left(\frac{15.369}{345.388}\right)^2 + \left(\frac{0.89}{257.3}\right)^2} = \pm 0.0599 \quad (C5)$$

Now the error propagation from computing the exponential will be found. The error propagation is defined as:

$$err_{exp} = \pm \exp\left(\frac{N}{D}\right) err_{div} \quad (C6)$$

where N , D , and err_{div} are defined as before. Equation C6 becomes:

$$err_{exp} = \pm \exp\left(\frac{345.388}{257.3}\right) \times 0.0599 = \pm 0.2293 \quad (C7)$$

The error propagation in e_s is found by using (C2):

$$err_{e_s} = \pm e_{so} err_{exp} \quad (C8)$$

Equation (C8) becomes:

$$err_{e_s} = \pm 0.61078 \times 0.2293 = \pm 0.1401 \quad (C9)$$

and e_s is 2.337 kPa.

For each instrument platform err_{e_s} was combined with the error in measured relative humidity (err_{RH}) to find the error in the vapor pressure, err_e . For the example

case e is 2.0566 kPa. The equation for the error propagation in a product is:

$$err_{AB} = AB \sqrt{\left(\frac{err_A}{A}\right)^2 + \left(\frac{err_B}{B}\right)^2} \quad (C10)$$

For the example case (C10) becomes:

$$err_e = \pm RH \times e_s \sqrt{\left(\frac{err_{RH}}{RH}\right)^2 + \left(\frac{err_{e_s}}{e_s}\right)^2} \quad (C11)$$

where RH is the relative humidity. Substituting values for the test case, (C11) becomes:

$$err_e = \pm 0.88 \times 2.337 \times \sqrt{\left(\frac{0.1401}{2.337}\right)^2 + \left(\frac{0.0206}{0.88}\right)^2} = \pm 0.1324 \quad (C12)$$

The mixing ratio (r) is found using:

$$r = \frac{\varepsilon e}{p - e} \quad (C13)$$

where p is the atmospheric air pressure and ε is the ratio of the dry air and water vapor gas constants. The error in e was found using (C12). The error propagation in the numerator of (C13) is found using (C2):

$$err_N = \pm \varepsilon \times e = \pm 0.622 \times 0.1324 = \pm 0.0824 \quad (C14)$$

The value of N is 1.27918. The error propagation due to adding two numbers when each have some uncertainty is:

$$err_{A+B} = \sqrt{err_A^2 + err_B^2} \quad (C15)$$

The error propagation in the denominator of (C13) becomes:

$$err_D = \pm \sqrt{err_p^2 + err_e^2} = \pm \sqrt{0.035^2 + 0.1324^2} = \pm 0.1369 \quad (C16)$$

where err_p is the uncertainty in the pressure measurement. The denominator is 95.843 kPa. The cumulative error in the mixing ratio can then be found using (C14):

$$err_r = \pm \frac{1.27918}{95.843} \times \sqrt{\left(\frac{0.0824}{1.27918}\right)^2 + \left(\frac{0.1369}{95.843}\right)^2} = \pm 8.995 \times 10^{-4} \quad (C17)$$

Uncertainty in θ_v occurs from errors in the measured temperature, pressure or mixing ratio. The error propagation from calculating θ is found by first finding the error propagation from p_o/p using (C6) where N is set to p_o , D is set to p , err_N is set to err_p , and err_D is set to 0. Equation (C6) becomes:

$$err_{div} = \pm \frac{100.0}{97.90} \times \sqrt{\left(\frac{0.035}{97.90}\right)^2 + \left(\frac{0.0}{100.0}\right)^2} = \pm 3.652 \times 10^{-4} \quad (C18)$$

The error propagation from rising a quantity to a power is defined as:

$$err_{power} = \pm n A^{n-1} err_A \quad (C19)$$

where n is the power, and A is value being raised to the power n . Equation (C19)

becomes:

$$err_{power} = \pm 0.286 \times \left(\frac{100.0}{97.90}\right)^{0.286-1} \times 3.652 \times 10^{-4} = 1.028 \times 10^{-4} \quad (C20)$$

The value of err_{power} is then combined with err_r to give the error in θ using (C10):

$$err_{\theta} = \pm T \times \left(\frac{p_o}{p}\right)^{0.286} \times \sqrt{\left(\frac{err_r}{T}\right)^2 + \left(\frac{err_p}{\{p_o/p\}^{0.286}}\right)^2} \quad (C21)$$

Equation example (C21) becomes:

$$err_{\theta} = \pm 293.16 \times 1.006 \times \sqrt{\left(\frac{0.89}{293.16}\right)^2 + \left(\frac{1.028 \times 10^{-4}}{1.006}\right)^2} = \pm 0.896 \quad (C22)$$

For this example, θ was found to be 294.93 K. The value of θ_v is then found using:

$$\theta_v = \theta(1 + 0.61r) \quad (C23)$$

The error propagation for the right most term inside the brackets is found using (C2)

$$err = \pm 0.61 \times 8.995 \times 10^{-4} = \pm 5.487 \times 10^{-5} \quad (C24)$$

Equation (C10) is used to complete the the uncertainty calculations for θ_v :

$$err_{\theta_v} = \pm 294.93 \times 1.008 \times \sqrt{\left(\frac{0.896}{294.93}\right)^2 + \left(\frac{5.487 \times 10^{-5}}{1.008}\right)^2} = \pm 0.903 \quad (C25)$$

C.2 Error Calculation for z_{LCL}

Teten's equation is inverted to find the dew point (T_D):

$$T_D = \frac{35.86 \ln(e/e_{so}) - 4717.31}{\ln(e/e_{so}) - 17.2694} \quad (C26)$$

The uncertainty associated with $err_{e/e_{so}}$ is found using (C6):

$$err_{e/e_{so}} = \pm \frac{2.0566}{0.61078} \times \frac{0.1324}{2.0566} = \pm 0.2168 \quad (C27)$$

The error propagation due to the natural logarithm is expressed by:

$$err_{\ln} = \pm \frac{err_y}{y} \quad (C28)$$

where y is the argument of the logarithm and err_y is the uncertainty in y . In this case it becomes:

$$err_{\ln} = \pm \frac{err_{e/e_{so}}}{e/e_{so}} = \pm \frac{0.2168}{3.3671} = \pm 0.0644 \quad C29$$

Once the error in the logarithm is found the errors in the numerator are found using (C2):

$$err_N = \pm 35.86 \times err_{\ln} = \pm 2.309 \quad (C30)$$

The error in the denominator remains err_{\ln} . The error propagation in T_D is then found using (C4):

$$err_{T_D} = \pm \frac{-4671.2076}{-16.046} \times \sqrt{\left(\frac{2.309}{-4671.2076}\right)^2 + \left(\frac{0.0644}{-16.046}\right)^2} = \pm 1.177 \quad (C31)$$

While T_D is found to be 291.11 K. The z_{LCL} is then found from the simple empirical equation:

$$z_{LCL} = a(T - T_D) \quad (C32)$$

The uncertainty in the brackets is found using (C15):

$$err_{Add} = \pm \sqrt{err_T^2 + err_{T_D}^2} = \pm \sqrt{0.89^2 + 1.177^2} = \pm 1.476 \quad (C33)$$

The uncertainty in z_{LCL} is then found using (C2):

$$err_{z_{LCL}} = \pm 125.0 \times err_{Add} = \pm 125.0 \times 1.476 = \pm 184.5 \quad (C34)$$

In the example z_{LCL} was found to be 256.25 m. These calculations were carried out at each time for the SMOS calculated θ_v and z_{LCL} , and the θ_v calculated from the sondes.

Appendix D. Cloud and Weather Observations

D.1 Cloud Description

Table D.1. Cloud descriptions used by human observers at the ARM CART site (Cederwall Personal Communication). These codes are used in the daily tables of observed cloud type. Acceptable low cloud types for any case study day was type 1 or 2.

Low Cloud Layer

Type	Technical Description	Non-Technical Description
0	No Stratocumulus, Stratus, Cumulus or Cumulonimbus	No low clouds
1	Cumulus humilis or Cumulus fractus other than of bad weather, or both	Fair-weather Cumulus with little vertical extent, and/or ragged Cumulus
2	Cumulus mediocris or congestus, with or without Cumulus of species fractus or humilis or Stratocumulus, all having their bases at the same level	Cumulus with moderate to strong vertical extent, generally with bulges in the form of domes or towers, they can be accompanied by other Cumulus or by Stratocumulus, all with bases at the same level
3	Cumulonimbus calvus, with or without Cumulus, Stratocumulus or Stratus	Cumulonimbus whose summits, at least partially, lack sharp outlines, but are neither clearly fibrous nor in the form of an anvil; Stratocumulus, Cumulus, or Stratus may also be present
4	Stratocumulus cumulogenitus	Stratocumulus formed by the spreading out of Cumulus; Cumulus may also be present
5	Stratocumulus other than stratocumulus cumulogenitus	Stratocumulus not resulting from the spreading out of Cumulus

Low Cloud Layer (continued)

Type	Technical Description	Non-Technical Description
6	Stratus nebulosus or Stratus fractus other than of bad weather, or both	Fair-weather Stratus in a more or less continuous sheet or layer, or in ragged shreds, or both
7	Stratus fractus or Cumulus fractus of bad weather, or both (pannus), usually below Altostratus or Nimbostratus	Bad weather Stratus fractus or bad weather Cumulus fractus of, or both (pannus), below Altostratus or Nimbostratus
8	Cumulus and Stratocumulus other than Stratocumulus cumulogenitus, with bases at different levels	Cumulus and Stratocumulus other than those formed from the spreading out of Cumulus; the base of the Cumulus is at a different level from that of the Stratocumulus
9	Cumulonimbus capillatus (often with an anvil), with or without Cumulonimbus calvus, Cumulus, Stratocumulus, Stratus or pannus	Cumulonimbus, with a clear fibrous (cirriform) upper part, or an upper part in the form of an anvil, may or may not be accompanied by Cumulonimbus without an anvil or fibrous upper part, by Cumulus, Stratocumulus, Stratus or pannus
x	Low clouds invisible owing to darkness, fog, blowing dust or sand, or other similar phenomena	Any low cloud invisible owing to darkness, fog, blowing dust or sand, or other similar phenomena

Mid Cloud Layer

Type	Technical Description	Non-Technical Description
0	No Altocumulus, Altostratus or Nimbostratus	No mid clouds
1	Altostratus translucidus	Altostratus, most of which is semitransparent; through which the sun or moon may be weakly visible, as through ground glass
2	Altostratus opacus or Nimbostratus	Altostratus, most of which is sufficiently dense to hide the sun or moon, or Nimbostratus
3	Altocumulus translucidus at a single level	Altocumulus, most of which is semi-transparent; the elements of the cloud change slowly and are all at a one level
4	Patches (often lenticular) of Altocumulus translucidus, continually changing and occurring at one or more levels	Patches (often in the form of almonds or fish) of Altocumulus, the most of which is semi-transparent; the clouds occur at one or more levels and the elements are continually changing in appearance
5	Altocumulus translucidus in bands, or one or more layers of Altocumulus translucidus or opacus, progressively invading the sky; these Altocumulus clouds generally thicken as a whole	Semi-transparent Altocumulus in bands, or Altocumulus in one or more fairly continuous layers (semi-transparent or opaque), progressively invading the sky; with clouds generally thickening as a whole
6	Altocumulus cumulogenitus (or cumulonimbogenitus)	Altocumulus resulting from the spreading out of Cumulus (or Cumulonimbus)

Mid Cloud Layer (continued)

Type	Technical Description	Non-Technical Description
7	Alto cumulus translucidus or opacus in two or more layers, or Alto cumulus opacus in a single layer, not progressively invading the sky, or Alto cumulus with Altostratus or Nimbostratus	Alto cumulus in two or more layers, usually opaque in places, and not progressively invading the sky; or an opaque layer of Alto cumulus, not progressively invading the sky; or Alto cumulus together with Altostratus or Nimbostratus
8	Alto cumulus castellanus or floccus	Alto cumulus with sproutings in the form of small towers or battlements, or Alto cumulus having the appearance of cumuli-form tufts
9	Alto cumulus of a chaotic sky, generally at several levels	Alto cumulus of a chaotic sky, generally at several levels

High Cloud Layer

Type	Technical Description	Non-Technical Description
0	No Cirrus, Cirrocumulus or Cirrostratus	No high clouds
1	Cirrus fibratus, sometimes uncinus, not progressively invading the sky	Cirrus in the form of filaments, strands, or hooks, not progressively invading the sky
2	Cirrus spissatus, in patches or entangled sheaves, which usually do not increase and sometimes seem to be the remains of the upper part of a Cumulonimbus; or Cirrus castellanus or floccus	Dense Cirrus, in patches or entangled sheaves, which usually do not increase and may seem to be the remains of the upper part of a Cumulonimbus; or Cirrus with sproutings in the form of small turrets, or Cirrus having the appearance of cumuliform tufts
3	Cirrus spissatus cumulonimbogenitus	Dense Cirrus, often in the form of an anvil, which are the remains of the upper parts of a Cumulonimbus
4	Cirrus uncinus or fibratus, or both, progressively invading the sky; they generally thicken as a whole	Cirrus in the form of hooks and/or of filaments, progressively invading the sky; generally becoming denser as a whole
5	Cirrus (often in bands) and Cirrostratus, or Cirrostratus alone, progressively invading the sky; they generally thicken as a whole, but the continuous veil does not reach 45 degrees above the horizon	Cirrostratus and/or Cirrus (often in bands converging towards one point or two opposite points of the horizon); in either case, they are progressively invading the sky, and generally growing denser as a whole, but the continuous veil does not reach 45 ° above the horizon

High Cloud Layer (continued)

Type	Technical Description	Non-Technical Description
6	Cirrus (often in bands) and Cirrostratus, or Cirrostratus alone, progressively invading the sky; they generally thicken as a whole, but the continuous veil extends more than 45 ° above the horizon, without the sky being totally covered	Cirrostratus and/or Cirrus (often in bands converging towards one point or two opposite points of the horizon); in either case, they are progressively invading the sky, and generally growing denser as a whole, the continuous veil extends more than 45 ° above the horizon, without the sky being totally covered
7	Cirrostratus covering the celestial dome	Veil of Cirrostratus covering the whole sky
8	Cirrostratus not progressively invading the sky and not entirely covering it	Cirrostratus not progressively invading the sky and not completely covering the sky
9	Cirrocumulus alone, or Cirrocumulus predominant among the high clouds	Cirrocumulus alone; or Cirrocumulus accompanied by Cirrus or Cirrostratus, or both, with Cirrocumulus predominant

D.2 Hourly Weather and Cloud Observations for the Case Study Days

D.2.1 Date: 1 May 1994

Table D.2. Hourly observations from 1 May, 1994 at the Central Facility

Time (LST)	Winds	Press (kPa)	Temp (°C)	RH (%)	Total	Weather Type
	Spd/Dir (m s ⁻¹ /deg)				Cloud Coverage	
0000	3.5/029	98.74	6.2	88	Overcast	
0100	3.3/017	98.71	5.9	87	Overcast	
0200	3.4/013	98.66	4.9	87	Clear	
0300	1.5/332	98.71	4.0	92	Clear	
0400	1.3/340	98.70	3.6	95	Clear	
0500	1.7/295	98.72	3.4	94	Clear	
0600	1.7/333	98.74	2.5	97	Clear	
0700	1.9/019	98.73	4.3	94	Clear	
0800	1.9/019	98.73	4.3	94	Clear	
0900	3.4/062	98.72	6.8	73	Clear	
1000	2.9/072	98.75	8.6	64	Clear	
1100	2.2/090	98.74	9.6	61	Scattered	
1200	2.2/142	98.70	10.3	59	Scattered	
1300	3.4/110	98.61	12.2	59	Scattered	
1400	2.5/114	98.48	12.6	57	Scattered	
1500	3.5/118	98.33	14.7	58	Scattered	
1600	3.5/114	98.24	14.5	59	Scattered	
1700	4.9/121	98.11	15.3	56	Broken	
1800	5.9/139	98.05	15.4	58	Broken	

Table D.3. Hourly cloud coverage by sky quadrant at the Central Facility 1 May, 1994

Cloud Observations, Whole Sky Cloud Types:

Time (LST)	Quadrant	Low			Mid			High		
		Amt	Height (km/10)	Type	Amt	Height (km/10)	Type	Amt	Height (km/10)	Type
0900	NW							0.1	090	1
1000	NE	0.1	15	1						
	SE	0.1	15	1						
	SW	0.1	15	1						
	NW	0.2	15	1	0.1	050	2	0.1	090	1
1100	NE	0.1	15	1				0.1	090	6
	SE	0.1	15	1						
	SW	0.1	15	1						
	NW	0.1	15	1						
1200	NE	0.4	15	1						
	SE	0.3	15	1						
	SW	0.4	15	1						
	NW	0.4	15	1						
1300	NE	0.3	15	1						
	SE	0.6	15	1						
	SW	0.3	15	1						
	NW	0.2	15	1						
1400	NE	0.1	15	1						
	SE	0.1	15	1						
	SW	0.1	15	1						
	NW	0.1	15	1						
1500	NE	0.1	15	1						
	SE	0.1	15	1						
	SW	0.2	15	1						
	NW	0.3	15	1						
1600	NE	0.1	15	1	.4	050	1			
	SE				.3	050	1			
	SW				.6	050	1			
	NW				.4	050	1			

Table D.3. continued. Hourly cloud coverage by sky quadrant at the Central Facility 1 May, 1994

Cloud Observations, Whole Sky Cloud Types:

Time (LST)	Quadrant	Low			Mid			High		
		Amt	Height (km/10)	Type	Amt	Height (km/10)	Type	Amt	Height (km/10)	Type
1700	NE				.8	050	1			
	SE				.7	050	1			
	SW				.6	050	1			
	NW				.9	050	1			

Table D.4. Hourly overhead cloud amounts from 1 May, 1994.

Overhead Cloud Amount (30° Arc)

Time (LST)	Cloud Cover (%)	Height (km/10)	Type
1000	0.1	015	1
1100	0.2	015	1
1200	0.8	015	1
1300	0.1	015	1
1400	0.1	015	1
1500	0.1	015	1
1600	0.2	050	1
1700	0.7	050	1

D.2.2 Date: 27 July 1994

Table D.5. Hourly observations from 27 July, 1994 at the Central Facility

Time (LST)	Winds	Press (kPa)	Temp (°C)	RH (%)	Total	Weather Type
	Spd/Dir (m s ⁻¹ /deg)				Cloud Coverage	
0000	4.7/317	98.06	17.7	85	Clear	
0100	4.3/303	98.06	16.7	89	Clear	
0200	4.2/282	98.05	16.2	89	Clear	
0300	4.7/282	98.03	15.4	91	Clear	
0400	4.3/289	98.04	15.1	92	Clear	
0500	4.5/282	98.06	14.4	94	Scattered	
0600	4.2/300	98.10	14.6	92	Scattered	
0700	3.7/297	98.13	16.7	85	Scattered	light haze
0800	3.0/326	98.16	19.2	77	Scattered	light haze
0900	3.5/354	98.17	22.3	61	Scattered	very light haze
1000	5.3/360	98.16	24.2	49	Scattered	
1100	6.0/347	98.15	24.9	45	Scattered	light haze
1200	7.2/003	98.10	25.6	45	Scattered	
1300	7.2/003	98.10	25.6	45	Scattered	
1400	5.7/020	98.05	26.3	42	Scattered	light haze
1500	6.3/355	98.01	27.1	43	Scattered	light haze
1600	5.2/002	97.95	26.9	39	Scattered	
1700	5.8/015	97.89	27.3	37	Scattered	
1800	7.7/020	97.89	27.1	36	Scattered	

Table D.6. Hourly cloud coverage by sky quadrant at the Central Facility 27 July, 1994

Cloud Observations, Whole Sky Cloud Types:

Time (LST)	Quadrant	Low			Mid			High		
		Amt	Height (km/10)	Type	Amt	Height (km/10)	Type	Amt	Height (km/10)	Type
0500	NE				0.1	55	7			
0600	NE				0.1	55	7			
0700	NE				0.2	60	4	0.2	100	9
	SE							0.1	100	9
0800	NE				0.3	60	4	0.2	100	9
	SE							0.2	100	9
0900	NE				0.2	60	4	0.4	100	9
	SE							0.3	100	9
1000	NE				0.2	60	4	0.2	100	9
	SE				0.1	60	4	0.4	100	9
1100	NE	0.1	15	1						
	SE	0.1	15	1	0.1	60	4	0.2	100	9
	SW	0.1	15	1				0.3	100	9
	NW	0.1	15	1						
1200	NE	0.2	15	1						
	SE	0.2	15	1						
	SW	0.3	15	1						
	NW	0.1	15	1						
1300	NE	0.3	12	8						
	SE	0.3	15	1						
	SW	0.3	15	1						
	NW	0.2	15	1						
1400	NE	0.3	12	8						
	SE	0.3	12	8						
	SW	0.3	15	1						
	NW	0.2	15	1						
1500	NE	0.2	15	1						
	SE	0.2	12	8						
	SW	0.2	15	1				0.2	100	9
	NW	0.1	15	1				0.2	100	9

Table D.6 continued. Hourly cloud coverage by sky quadrant at the Central Facility 27 July, 1994

Cloud Observations, Whole Sky Cloud Types:

Time (LST)	Quadrant	Low			Mid			High		
		Amt	Height (km/10)	Type	Amt	Height (km/10)	Type	Amt	Height (km/10)	Type
1600	NE	0.3	15	1						
	SE	0.3	15	1						
	SW	0.4	15	1						
	NW	0.4	15	1						
1700	NE	0.1	15	1						
	SE	0.2	15	1						
	SW	0.1	15	1						
	NW	0.2	15	1						

Table D.7. Hourly overhead cloud amounts from 27 July, 1994.

Overhead Cloud Amount (30° Arc)

Time (LST)	Cloud Cover (%)	Height (km/10)	Type
1200	0.1	015	1
1300	0.1	015	1
1400	0.1	015	1
1500	0.1	015	1

D.2.3 Date: 28 July 1994

Table D.8. Hourly observations from 28 July, 1994 at the Central Facility

Time (LST)	Winds Spd/Dir (m s ⁻¹ /deg)	Press (kPa)	Temp (°C)	RH (%)	Total Cloud Coverage	Weather Type
0000	0.4/034	97.94	20.7	60	Clear	
0100	2.6/256	97.92	18.3	76	Clear	
0200	3.9/267	97.94	17.8	79	Clear	
0300	4.1/295	97.96	16.1	86	Clear	
0400	4.1/335	97.99	15.5	88	Clear	
0500	4.4/291	97.99	15.8	86	Clear	
0600	3.6/306	98.04	15.5	86	Scattered	
0700	3.0/357	98.07	17.6	84	Scattered	light fog/moderate dew
0800	2.6/359	98.13	20.9	75	Scattered	light haze/dew
0900	1.1/008	98.15	22.1	67	Scattered	Haze
1000	2.5/066	98.15	24.7	57	Clear	moderate haze
1100	2.1/095	98.13	25.3	51	Scattered	Haze
1200	3.7/034	98.07	26.2	50	Scattered	Haze
1300	4.7/342	98.02	26.9	44	Scattered	Haze
1400	5.5/048	97.99	27.3	41	Scattered	
1500	2.7/060	97.96	27.6	41	Scattered	
1600	5.5/048	97.91	27.9	40	Scattered	
1700	4.8/065	97.89	37.3	39	Scattered	

Table D.9. Hourly cloud coverage by sky quadrant at the Central Facility 28 July, 1994

Cloud Observations, Whole Sky Cloud Types:

Time (LST)	Quadrant	Low			Mid			High		
		Amt	Height (km/10)	Type	Amt	Height (km/10)	Type	Amt	Height (km/10)	Type
0600	NE	0.1	12	4						
0700	NE							0.3	100	9
	SE							0.3	100	9
0800	NE				0.2	60	4	0.1	100	9
	SE				0.1	60	4	0.2	100	9
0900	NE				0.2	60	4	0.1	100	9
	SE				0.3	60	4			
1100	NW	0.1	15	1						
1200	NE	0.2	15	1						
	SE	0.2	15	1						
	SW	0.2	15	1						
	NW	0.3	15	1						
1300	NE	0.3	15	1						
	SE	0.4	15	1						
	SW	0.3	15	1						
	NW	0.4	15	1						
1400	NE	0.1	15	1						
	SE	0.3	15	1						
	SW	0.3	15	1				0.3	100	9
	NW	0.3	15	1				0.3	100	9
1500	NE	0.1	15	1						
	SE	0.2	15	1						
	SW	0.3	15	1						
	NW	0.3	15	1						
1600	NE	0.1	15	1						
	SE	0.1	15	1						
	SW	0.1	15	1				0.3	90	1
	NW	0.1	15	1				0.1	90	1
1700	NE							0.1	90	1
	SW							0.3	90	1
	NW							0.3	90	1

Table D.10. Hourly overhead cloud amounts from 28 July, 1994.

Overhead Cloud Amount (30° Arc)			
Time (LST)	Cloud Cover (%)	Height (km/10)	Type
1200	0.1	015	1
1300	0.1	015	1
1400	0.1	015	1
1500	0.1	015	1
1700	0.1	090	1

D.2.4 Date: 31 July 1994

Table D.11. Hourly observations from 31 July, 1994 at the Central Facility

Time (LST)	Winds		Temp (°C)	RH (%)	Total Cloud Coverage	Weather Type
	Spd/Dir (m s ⁻¹ /deg)	Press (kPa)				
0000	6.5/162	97.64	21.3	84	Scattered	
0100	4.5/172	97.81	20.3	88	Scattered	possible light fog/haze forming on N horizon
0200	5.5/160	97.8.1	20.2	89	Scattered	very light dew
0300	5.4/154	97.63	19.3	91	Scattered	
0400	6.1/154	97.83	18.7	93	Clear	Dew
0500	6.3/163	97.87	18.7	90	Scattered	Dew
0600	6.6/174	97.71	19.1	85	Broken	light fog
0700	7.2/184	97.93	21.1	80	Scattered	
0800	9.1/182	97.90	23.1	76	Scattered	
0900	6.0/192	97.91	25.1	67	Clear	
1000	7.1/196	97.89	27.3	56	Clear	
1100	5.9/180	97.87	29.0	54	Clear	
1200	4.5/188	97.82	30.3	51	Clear	Haze
1300	7.1/158	97.78	31.4	46	Scattered	
1400	5.3/143	97.74	32.1	41	Scattered	
1500	5.7/191	97.72	32.9	42	Scattered	
1600	7.2/162	97.68	31.9	41	Scattered	
1700	5.2/170	97.67	29.4	54	Scattered	

Table D.12. Hourly cloud coverage by sky quadrant at the Central Facility 31 July, 1994

Cloud Observations, Whole Sky Cloud Types:

Time (LST)	Quadrant	Low			Mid			High		
		Amt	Height (km/10)	Type	Amt	Height (km/10)	Type	Amt	Height (km/10)	Type
0000	SW							0.4	100	9
	NW							0.4	100	9
0100	NE							0.4	100	9
	SE							0.2	100	9
	SW							0.2	100	9
	NW							0.5	100	9
0200	NW							0.2	100	9
0300	NW							0.7	100	9
0500	NE	0.1	10	5	0.1	60	4	0.1	100	9
	SE				0.3	60	4	0.1	100	9
	SW				0.3	60	4	0.2	100	9
	NW							0.4	100	9
0600	NE				0.1	60	4	0.3	100	9
	SE				0.1	60	4	0.6	100	9
	SW				0.3	60	4	0.3	100	9
	NW	0.2	12	8	0.1	60	4	0.2	90	2
0700	NE							0.4	90	1
	SE							0.2	90	1
	SW	0.1	12	2				0.2	90	1
	NW	0.3	12	2				0.3	90	1
0800	NE							0.1	90	1
	SE							0.3	90	1
	SW							0.2	90	1
	NW							0.3	90	1
1300	NE	0.2	15	1						
	SE	0.2	15	1						
	SW	0.3	15	1						
	NW	0.4	15	1						
1400	NE	0.2	15	1						
	SE	0.3	15	1						
	SW	0.4	15	1						
	NW	0.4	15	1						

Table D.12 continued. Hourly cloud coverage by sky quadrant at the Central Facility 31 July, 1994

Cloud Observations, Whole Sky Cloud Types:

Time (LST)	Quadrant	Low			Mid			High		
		Amt	Height (km/10)	Type	Amt	Height (km/10)	Type	Amt	Height (km/10)	Type
1500	NE	0.2	15	1						
	SE	0.1	15	1						
	SW	0.1	15	1						
	NW	0.3	15	1				0.1	90	1
1600	NE	0.1	12	8						
	SE	0.1	12	8						
	SW	0.2	12	2	0.1	55	7	0.1	90	8
	NW	0.3	12	2	0.1	55	7	0.1	90	8
1700	NE	0.1	15	1				0.1	90	1
	SE	0.1	15	1				0.1	90	1
	SW	0.1	15	1						
	NW	0.1	15	1						

Table D.13. Hourly overhead cloud amounts from 31 July, 1994.

Overhead Cloud Amount (30° Arc)

Time (LST)	Cloud Cover (%)	Height (km/10)	Type
0500	0.2	100	9
0600	0.1	090	2
	0.4	100	9
1300	0.3	015	1
1400	0.3	015	1
1500	0.1	015	1
1600	0.1	012	8

D.2.5 Date: 27 June 1995

Table D.14. Hourly observations from 27 June, 1995 at the Central Facility

Time (LST)	Winds Spd/Dir (m s ⁻¹ /deg)	Press (kPa)	Temp (°C)	RH (%)	Total Cloud Coverage	Weather Type
0000	0.0/000	98.94	20	64	Clear	
0100	0.0/250	98.92	19	72	Scattered	
0200	0.0/232	98.93	18	76	Scattered	
0500	0.0/285	98.91	17	80	Scattered	
0600	0.0/307	98.95	19	76	Scattered	
0700	0.0/334	98.95	23	65	Scattered	very light haze
0800	4.0/002	98.92	28	52	Broken	
0900	0.0/170	99.03	35	31	Broken	Haze
1000	1.3/231	99.06	36	31	Scattered	Haze
1100	0.4/150	99.05	35	29	Scattered	
1200	1.3/210	98.97	35	29	Scattered	light haze/smoke
1300	2.7/204	98.92	34	30	Scattered	smoke
1400	0.4/178	98.90	34	33	Scattered	smoke/haze
1500	2.7/153	98.85	33	36	Scattered	light haze/smoke

Table D.15. Hourly cloud coverage by sky quadrant at the Central Facility 27 June, 1995

Cloud Observations, Whole Sky Cloud Types:

Time (LST)	Quadrant	Low			Mid			High		
		Amt	Height (km/10)	Type	Amt	Height (km/10)	Type	Amt	Height (km/10)	Type
0600	NE				0.4	55	7			
	SE				0.3	55	7			
	SW				0.2	55	7			
	NW				0.3	55	7			
0700	NE	0.4	15	1				0.1	100	9
	SE	0.2	10	5	0.2	60	4	0.1	100	9
	SW	0.3	10	5	0.1	60	4			
	NW	0.3	15	1	0.2	60	4	0.1	100	9
0800	NE	0.3	15	1				0.2	100	9
	SE	0.3	10	5	0.1	60	4			
	SW	0.4	15	1						
	NW	0.2	15	1	0.3	60	4			
0900	NE	0.1	10	5	0.1	60	4	0.2	100	9
	SE	0.2	10	5	0.2	60	4	0.2	100	9
	SW	0.3	12	4				0.2	100	9
	NW	0.1	15	1	0.1	60	4	0.2	100	9
1000	NE							0.1	100	9
	SE				0.4	60	4	0.2	100	9
	SW				0.3	60	4	0.1	100	9
	NW				0.2	60	4	0.1	100	9
1100	NE				0.1	60	4			
	SE	0.1	15	1	0.3	60	4	0.1	100	9
	SW	0.1	15	1	0.1	60	4	0.1	100	9
	NW	0.1	15	1	0.3	60	4	0.1	100	9
1200	NE	0.1	15	1	0.2	60	4			
	SE	0.1	15	1	0.2	60	4	0.2	100	9
	SW				0.1	60	4			
	NW	0.1	15	1						
1300	NE	0.1	15	1	0.2	60	4			
	SE				0.2	60	4	0.3	100	9
	SW	0.2	15	1				0.1	100	9
	NW	0.1	15	1						

Table D.15 continued. Hourly cloud coverage by sky quadrant at the Central Facility 27 June, 1995

Cloud Observations, Whole Sky Cloud Types:

Time (LST)	Quadrant	Low			Mid			High		
		Amt	Height (km/10)	Type	Amt	Height (km/10)	Type	Amt	Height (km/10)	Type
1400	NE	0.2	15	1	0.2	60	4			
	SE	0.1	15	1	0.1	60	4			
	SW	0.2	15	1	0.2	60	4			
	NW	0.3	15	1						
1500	NE	0.3	15	1	0.1	60	4			
	SE	0.1	15	1						
	SW	0.2	15	1	0.2	60	4			
	NW	0.3	15	1						

Table D.16. Hourly overhead cloud amounts from 27 July, 1995.

Overhead Cloud Amount (30° Arc)

Time (LST)	Cloud Cover (%)	Height (km/10)	Type
0700	0.6	015	1
0800	0.5	015	1
0900	0.1	015	1
	0.5	100	9
1000	0.1	100	9
1300	0.1	015	1
	0.1	100	9
1400	0.1	015	1
1500	0.1	015	1

D.2.6 Date: 6 July 1995

Table D.17. Hourly observations from 6 July, 1995 at the Central Facility

Time (LST)	Winds Spd/Dir (m s ⁻¹ /deg)	Press (kPa)	Temp (°C)	RH (%)	Total Cloud Coverage	Weather Type
0000	0.0/320	99.37	21	73	Scattered	
0100	0.0/320	99.37	21	69	Clear	
0200	0.0/320	99.41	20	78	Clear	
0500	2.7/230	99.43	18	82	Clear	
0600	0.0/240	99.52	20	77	Clear	
0700	0.0/240	99.65	27	58	Scattered	
0800	2.2/200	99.68	32	45	Scattered	light haze
0900	2.7/190	99.72	34	39	Scattered	light haze
1000	3.6/190	99.72	36	28	Scattered	
1100	3.1/260	99.71	37	34	Scattered	
1200	4.5/250	99.60	40	28	Scattered	
1400	4.9/270	99.54	40	27	Scattered	
1500	4.5/280	99.49	39	28	Scattered	

Table D.18. Hourly cloud coverage by sky quadrant at the Central Facility 6 July, 1995

Cloud Observations, Whole Sky Cloud Types:

Time (LST)	Quadrant	Low			Mid			High		
		Amt	Height (km/10)	Type	Amt	Height (km/10)	Type	Amt	Height (km/10)	Type
0000	NE				0.2	60	3			
	SE				0.2	60	3			
	SW				0.6	60	3			
	NW				0.4	60	3			
0700	SW				0.1	60	4			
	NW				0.1	60	4			
0800	NE	0.1	15	1						
0900	NE	0.1	15	1						
	SE	0.1	15	1						
	SW	0.1	15	1						
	NW	0.1	15	1						
1000	SE	0.1	15	1						
	SW	0.1	15	1						
1100	NE				0.1	60	4			
	SE	0.1	15	1						
	SW	0.1	15	1						
	NW	0.1	15	1						
1200	NE	0.1	15	1						
	SE	0.3	15	1						
	SW	0.2	15	1						
	NW	0.1	15	1						
1400	NE	0.3	15	1						
	SE	0.4	15	1						
	SW	0.3	15	1						
	NW	0.3	15	1						
1500	NE	0.4	15	1						
	SE	0.3	15	1						
	SW	0.4	15	1						
	NW	0.2	15	1						

Table D.19. Hourly overhead cloud amounts from 6 July 1995.

Overhead Cloud Amount (30° Arc)			
Time (LST)	Cloud Cover (%)	Height (km/10)	Type
0900	0.1	015	1
1100	0.1	060	4
1200	0.1	015	1
1300			
1400	0.1	015	1
1500	0.3	015	1

D.2.7 Date: 9 July 1995

Table D.20. Hourly observations from 9 July, 1995 at the Central Facility

Time (LST)	Winds	Press (kPa)	Temp (°C)	RH (%)	Total	Weather Type
	Spd/Dir (m s ⁻¹ /deg)				Cloud Coverage	
0500	0.0/280	99.08	22	79	Scattered	
0600	0.0/240	99.10	23	75	Scattered	
0700	0.0/060	99.19	27	65	Scattered	
0800	0.0/070	99.25	30	53	Scattered	
0900	0.0/070	99.25	33	45	Clear	
1000	0.0/040	99.26	34	43	Clear	
1100	0.0/070	99.28	36	41	Clear	
1200	0.0/090	99.28	38	33	Clear	
1300	0.0/080	99.24	38	33	Clear	
1400	0.0/080	99.21	38	33	Clear	
1500	0.0/060	99.20	38	37	Clear	

Table D.21. Hourly cloud coverage by sky quadrant at the Central Facility 9 July, 1995

Cloud Observations, Whole Sky Cloud Types:

Time (LST)	Quadrant	Low			Mid			High		
		Amt	Height (km/10)	Type	Amt	Height (km/10)	Type	Amt	Height (km/10)	Type
0500	NE				0.1	60	3			
	SE				0.4	60	3			
	SW				0.3	60	3			
	NW				0.1	60	3			
0600	NE				0.2	60	3			
	SE				0.4	55	7			
	SW				0.3	55	7			
	NW				0.1	60	3			
0700	SE				0.4	60	3			
	SW				0.2	60	3			
	NW				0.1	60	3			
0800	SE				0.3	60	3			

Table D.22. Hourly overhead cloud amounts from 9 July, 1995.

Overhead Cloud Amount (30° Arc)

Time (LST)	Cloud Cover (%)	Height (km/10)	Type
0500	0.2	060	3
0600	0.1	060	3
0700	0.1	060	3

D.2.8 Date: 11 July 1995

Table D.23. Hourly observations from 11 July, 1995 at the Central Facility

Time (LST)	Winds Spd/Dir (m s ⁻¹ /deg)	Press (kPa)	Temp (°C)	RH (%)	Total Cloud Coverage	Weather Type
0000	2.7/180	99.02	26	72	Clear	
0100	3.1/180	98.98	25	73	Clear	
0200	1.8/120	98.97	24	78	Clear	
0500	0.9/130	99.01	22	87	Clear	
0600	1.8/140	99.02	23	86	Clear	
0700	1.3/150	99.09	27	71	Scattered	very light dew/haze
0800	4.4/175	97.74	28.7	56	Scattered	light haze
0900	3.1/205	97.74	31.7	46	Scattered	smoke
1000	2.2/260	99.12	42	29	Clear	moderate-heavy smoke
1100	3.1/260	99.11	44	47	Clear	smoke/haze
1200	3.1/260	99.07	45	26	Clear	light haze/smoke
1300	1.8/220	99.03	45	24	Clear	light haze/smoke
1400	4.0/180	98.95	43	24	Clear	moderate smoke
1500	5.4/190	98.93	43	23	Clear	moderate smoke

Table D.24. Hourly cloud coverage by sky quadrant at the Central Facility 11 July, 1995

Cloud Observations, Whole Sky Cloud Types:

Time (LST)	Quadrant	Low			Mid			High		
		Amt	Height (km/10)	Type	Amt	Height (km/10)	Type	Amt	Height (km/10)	Type
0700	NE				0.1	60	4			
0800	NE				0.1	50	8			
0900	NE				0.1	50	8			

Table D.25. Hourly overhead cloud amounts from 11 July, 1995.

Overhead Cloud Amount (30° Arc)			
Time (LST)	Cloud Cover (%)	Height (km/10)	Type
0700	0.1	060	4
0800	0.1	050	8
0900	0.1	050	8

D.2.9 Date: 13 July 1995

Table D.26. Hourly observations from 13 July, 1995 at the Central Facility

Time (LST)	Winds	Press (kPa)	Temp (°C)	RH (%)	Total	Weather Type
	Spd/Dir (m s ⁻¹ /deg)				Cloud Coverage	
0600	1.3/170	990.1	27	73	Clear	
0700	2.7/170	989.9	26	76	Clear	
0800	2.2/190	989.9	27	75	Clear	
1100	0.4/150	990.9	24	85	Clear	
1200	0.4/140	991.3	24	85	Clear	
1300	2.7/170	991.6	28	72	Scattered	light haze
1400	4.0/190	991.6	33	56	Scattered	Haze
1500	4.5/200	991.4	36	47	Clear	light haze
1600	3.1/200	991.1	40	36	Scattered	
1700	3.6/190	991.3	41	34	Scattered	moderate smoke
1800	4.9/180	991.0	39	34	Scattered	Haze/smoke
1900	4.9/180	990.7	39	34	Scattered	Haze/smoke
2000	2.7/140	990.6	39	37	Scattered	Haze
2100	5.4/120	990.5	38	35	Scattered	light haze

Table D.27. Hourly cloud coverage by sky quadrant at the Central Facility 13 July, 1995

Cloud Observations, Whole Sky Cloud Types:

Time (LST)	Quadrant	Low			Mid			High		
		Amt	Height (km/10)	Type	Amt	Height (km/10)	Type	Amt	Height (km/10)	Type
0700	NE	0.1	15	1						
	SE				0.1	60	4			
	SW	0.1	15	1						
0800	SW							0.1	100	9
1000	SW				0.1	60	4			
1100	SE	0.1	15	1						
1200	NE	0.2	15	1						
	SE	0.2	15	1						
	SW	0.2	15	1						
	NW	0.1	15	1						
1300	NE	0.2	15	1						
	SE	0.2	15	1						
	SW	0.2	15	1						
	NW	0.2	15	1						
1400	NE	0.2	15	1						
	SE	0.2	15	1						
	SW	0.2	15	1						
	NW	0.2	15	1						
1500	NE	0.2	15	1						
	SE	0.2	15	1						
	SW	0.2	15	1						
	NW	0.2	15	1						

Table D.28. Hourly overhead cloud amounts from 13 July, 1995.

Overhead Cloud Amount (30° Arc)			
Time (LST)	Cloud Cover (%)	Height (km/10)	Type
1100	0.1	015	1
1200	0.2	015	1
1300	0.1	015	1
1400	0.1	015	1
1500	0.1	015	1

Appendix E. JFD Parameters

Table E.1. JFD parameters used as input to the CuP model. B corresponds to Bowen ratio parameters. S corresponds to Solar Forcing parameters. Cut offs represent where the JFDs were truncated.

Time (LST)	Axes Slopes		Standard Deviations		Cut Offs	
	B (K/m)	S (K/m)	B (m)	S (K)	B (m)	S (K)
1 May 1994						
0830	-5.12×10^{-2}	2.83×10^{-3}	2.934	0.286	5.868	0.572
1130	-3.15×10^{-2}	3.09×10^{-3}	4.541	0.317	9.081	0.635
1452	-2.60×10^{-2}	3.33×10^{-3}	0.475	0.304	0.949	0.607
1730	-4.14×10^{-3}	-3.19×10^{-3}	17.50	0.103	34.99	0.205
27 July 1994						
0830	-1.41×10^{-2}	4.40×10^{-3}	84.505	2.055	169.01	4.110
1130	-6.53×10^{-3}	3.97×10^{-3}	14.618	0.445	29.236	0.890
1430	-9.30×10^{-3}	3.94×10^{-3}	18.862	0.460	37.723	0.920
1730	-3.06×10^{-4}	3.88×10^{-3}	21.734	0.276	43.468	0.552
28 July 1994						
0830	-2.18×10^{-2}	4.52×10^{-3}	2.059	0.477	4.104	0.954
1135	-1.06×10^{-2}	4.41×10^{-3}	12.36	0.437	24.73	0.874
1430	-5.47×10^{-3}	4.15×10^{-3}	22.86	0.404	45.72	0.807
1730	4.62×10^{-5}	4.06×10^{-3}	109.1	0.115	218.2	0.231
31 July 1994						
0830	-5.43×10^{-2}	4.75×10^{-3}	2.111	0.617	4.222	1.235
1130	-6.38×10^{-3}	4.79×10^{-3}	8.414	0.461	16.83	0.923
1430	-3.61×10^{-3}	4.50×10^{-3}	24.17	0.453	48.34	0.906
1730	1.68×10^{-3}	4.49×10^{-3}	22.29	0.315	44.58	0.630
27 June 1995						
0830	-2.16×10^{-2}	4.69×10^{-3}	2.142	0.972	4.284	1.944
0910	-1.55×10^{-2}	4.59×10^{-3}	8.556	0.470	17.11	0.939
1128	-8.25×10^{-3}	4.45×10^{-3}	17.15	0.610	34.30	1.219
1429	-1.11×10^{-2}	4.64×10^{-3}	15.70	0.421	31.39	0.841

Table E.1 continued. JFD parameters used as input to the CuP model. B corresponds to Bowen ratio parameters. S corresponds to Solar Forcing parameters. Cut offs represent where the JFDs were truncated.

Time (LST)	Axes Slopes		Standard Deviations		Cut Offs	
	B (K/m)	S (K/m)	B (m)	S (K)	B (m)	S (K)
6 July 1995						
0829	-1.05×10^{-2}	4.79×10^{-3}	7.980	0.888	15.94	1.777
1128	-4.85×10^{-3}	4.74×10^{-3}	56.68	0.774	113.36	1.548
1431	-2.25×10^{-3}	4.52×10^{-3}	53.27	0.492	106.54	0.984
9 July 1995						
0830	-2.24×10^{-2}	4.98×10^{-3}	1.826	0.551	3.651	1.102
1130	-7.28×10^{-3}	4.84×10^{-3}	14.37	0.423	28.73	0.846
1431	-1.25×10^{-2}	4.88×10^{-3}	29.91	0.577	59.81	1.154
11 July 1995						
0830	-2.17×10^{-2}	4.99×10^{-3}	5.229	0.925	10.46	1.851
1130	-9.36×10^{-3}	4.73×10^{-3}	15.36	0.798	30.73	1.597
1430	-3.80×10^{-3}	4.56×10^{-3}	60.53	0.472	121.1	0.943
13 July 1995						
0830	6.53×10^{-2}	5.24×10^{-3}	0.140	0.557	0.279	1.114
1131	-1.02×10^{-1}	5.09×10^{-3}	1.744	0.611	3.491	1.221
1430	2.10×10^{-1}	5.08×10^{-3}	1.145	0.429	2.289	0.849